



# Self-sustained shock oscillations on airfoils at transonic speeds

B.H.K. Lee\*

*Aerodynamics Laboratory, Institute for Aerospace Research, National Research Council, Ottawa, Ont., Canada K1A 0R6*

## Abstract

Self-sustained shock wave oscillations on airfoils at transonic flow conditions are associated with the phenomenon of buffeting. The physical mechanisms of the periodic shock motion are not yet fully understood even though experiments performed over fifty years ago have demonstrated the presence of oscillatory shock waves on the airfoil surfaces at high subsonic speeds. The unsteady pressure fluctuations generated by the low-frequency large-amplitude shock motions are highly undesirable from the structural integrity and aircraft maneuverability point of view. For modern supercritical wing design with thick profiles, the shock-induced fluctuations are particularly severe and methods to reduce the shock wave amplitudes to lower values or even to delay the oscillations to higher Mach numbers or incidence angles will result in expanding the buffet boundary of the airfoil. This review begins with a recapitulation of the classical work on shock-induced bubble separation and trailing edge separation of a turbulent boundary layer. The characteristics of the unsteady pressure fluctuations are used to classify the types of shock-boundary layer interaction. The various modes of shock wave motion for different flow conditions and airfoil configurations are described. The buffet boundaries obtained using the standard trailing edge pressure divergence technique and an alternative approach of measuring the divergence of normal fluctuating forces are compared to show the equivalence. The mechanisms of self-sustained shock oscillations are discussed for symmetrical circular-arc airfoils at zero incidence and for supercritical airfoils at high incidence angles with fully separated flows. The properties of disturbances in the wake are examined from linear stability analysis of two-dimensional compressible flows. The advances in high-speed computing make predictions of buffeting flows possible. Navier–Stokes solvers and approximate boundary layer-inviscid flow interaction methods are shown to give good correlation of frequencies and other unsteady flow characteristics with experiments. Finally, passive and active methods of shock oscillation control show promising results in delaying buffet onset to higher Mach numbers or incidence angles, thus enhancing the transonic performance of airfoils. © 2001 Elsevier Science Ltd. All rights reserved.

## Contents

1. Introduction . . . . .	149
2. Shock-induced separation on airfoils . . . . .	150
2.1. Steady flow separation . . . . .	150
2.2. Surface pressure fluctuations in separated flows . . . . .	153
3. Transonic buffeting of airfoils. . . . .	156
3.1. Buffet boundaries . . . . .	156
3.2. Beyond the buffet boundary . . . . .	158

\*Corresponding author. Tel.: +001-613-998-3401; fax: +001-613-998-1281.  
E-mail address: ben.lee@nrc.ca (B.H.K. Lee).

Nomenclature		St	Strouhal number
$a$	speed of sound	$s$	span
$b$	semi-chord; also half-width of wake	$T$	nondimensional time; also temperature
$c$	chord; also phase velocity	$T_p$	period of shock oscillation
$C_f$	skin friction coefficient	$t$	time
$C_L$	lift coefficient	$U$	freestream velocity
$C_{L\alpha}$	lift curve slope	$U_c$	mean velocity at center of wake; also broad-band convection velocity
$C_N$	normal force coefficient	$U_w$	mean velocity at edge of wake
$C_p$	pressure coefficient	$u$	streamwise velocity
$e$	energy	$u_s$	shock velocity
$f$	frequency	$V_s$	shock velocity
$H$	surface of discontinuity	$v$	velocity in $y$ -direction
$h_{ss}$	shock strength	$w$	downwash
$k$	reduced frequency based on semi-chord ( $= \omega b/U$ )	$(x_0, y_0)$	position of impulse source
$M$	freestream Mach number	$x_s$	shock position
$N$	normal force	$\alpha$	incidence angle; also ray angle; also complex wave number in $x$ -direction,
$P$	steady-state pressure	$\beta$	complex wave number in $z$ -direction
Pr	Prandtl number	$\delta$	flap deflection angle; also boundary layer thickness
$p$	instantaneous pressure	$\Phi$	total potential
$(p, q)$	vector parallel to normal of wavefront	$\phi$	phase angle; also velocity potential
$p_{rms}$	rms value of pressure	$\gamma$	ratio of specific heats,
$Q$	variables vector	$\gamma_{ab}^2$	coherence function of functions $a$ and $b$
$q$	dynamic pressure	$\kappa$	reduced frequency based on chord ( $= \omega c/U$ )
$R$	constant	$\mu$	viscosity
$R_{ec}$	Reynolds number based on chord	$\rho$	density
$r$	radius of wavefront	$\omega$	circular frequency
$S_a$	power spectral density of function $a$	$\bar{\omega}$	nondimensional frequency
$S_{ab}$	cross-power spectral density of functions $a$ and $b$	$\psi$	disturbance potential

4. Experimental studies on periodic shock oscillations. . . . .	160
4.1. Types of shock motion . . . . .	160
4.2. Biconvex circular-arc airfoils. . . . .	162
4.3. Supercritical airfoils. . . . .	167
5. Wave propagation in the airfoil flowfield . . . . .	171
5.1. Behavior of disturbances in two-dimensional nonuniform flows . . . . .	171
5.2. One-dimensional unsteady shock motion . . . . .	175
6. Propagation of disturbances in the wake . . . . .	176
6.1. Linearized equations of motion for compressible flows . . . . .	179
6.2. Stability analysis of a two-dimension compressible wake . . . . .	179
7. Numerical studies of periodic shock oscillations. . . . .	181
7.1. Navier–Stokes solutions . . . . .	181
7.2. Interactive boundary layer coupling method . . . . .	186
8. Control of shock oscillations . . . . .	188
8.1. Control of shock-boundary layer interaction . . . . .	188
8.2. Boundary layer control at the trailing edge . . . . .	191
9. Conclusions . . . . .	192
Acknowledgements. . . . .	193
References . . . . .	193

## 1. Introduction

At transonic flow conditions, many unsteady phenomena are associated with shock wave interaction with a separated boundary layer. The resulting pressure fluctuations cause control surface oscillations known as aileron buzz, periodic flows in supersonic intakes and cascades, and many other undesirable unsteady effects. In flight, aircraft wings can encounter flow-induced vibrations known as buffeting when separation of the boundary layer occurs. For modern supercritical wing design with thick profiles, the shock-induced fluctuations are particularly severe and often periodic shock motions with large amplitudes are observed at high subsonic Mach numbers or incidence angles. Such periodic shock motions have been detected over fifty years ago [1], but the cause of self-sustained shock oscillations on wings or airfoils is still not fully understood.

Shock-induced bubble separation and trailing edge separation have been reviewed in the classical work of Pearcey et al. [2], and the relation between trailing edge pressure divergence and the onset of buffeting has been widely used to determine the buffet boundary. The analysis is based on a steady-state behavior of the separated boundary layer. The use of unsteady pressure fluctuations to classify the type of shock boundary interaction was first proposed by Mundell and Mabey [3]. This is a useful extension of Pearcey et al. [2] flow separation models in analysing the flow characteristics.

The shock wave on the airfoil surface can oscillate in a variety of modes. Tijdeman [4] summarized three possible types of shock motion for an airfoil with an oscillating flap, and generalized them to other airfoil motions, such as pitch and plunge oscillations. These types of periodic motion are also observed during airfoil buffeting, and they are self-sustaining in that the motion is maintained without any external input of energy. Although unsteady flow behavior on airfoils at transonic speeds has been investigated as early as 1951 by Humphreys [5], systematic studies were not carried out until nearly twenty-five years later by McDevitt et al. [6] on an 18% circular-arc airfoil at zero incidence with an objective to provide data for computer code validations. The periodic flow behavior was later investigated in some details by Mabey et al. [7] on a 14% thick biconvex airfoil. Supercritical airfoils at high incidence angles were studied by Roos [8], Hirose and Miwa [9], Lee [10,11] and Stanewksy and Basler [12]. There is some difference in the mechanisms of periodic shock motion between a lifting airfoil at incidence and a symmetrical one at zero incidence.

Numerical simulation codes are quite successful in predicting the frequencies of shock oscillation, the buffet boundaries as well as the unsteady pressure fluctuations. Further refinement of these codes with better turbulence modelling can eventually predict the periodic shock

motion and buffeting flowfields with sufficient accuracy for the aircraft designer.

This review gives a brief account of the various topics related to self-sustained periodic shock motion and transonic buffeting on airfoils. Section 2 describes shock-induced separation based on the steady-state models proposed by Pearcey et al. [2]. The effects of Mach number, angle of incidence and trailing-edge flap deflection on the shock position are brought out. The classification of the types of flow separation using unsteady pressure measurements is described and an example from a supercritical airfoil is given. In Section 3, the definition of buffet boundary is given and methods to determine buffet onset are outlined. The behavior of the flow during an excursion into the buffet regime is illustrated by an example from a supercritical airfoil showing the changes in normal force fluctuations at constant incidence angle but with increasing Mach number. Experimental studies on periodic shock oscillations are discussed in Section 4. The types of shock oscillations according to Tijdeman [4] are described. The oscillatory flow for circular-arc airfoils at zero incidence and the mechanisms of self-sustained shock motion are discussed. The section concludes by showing typical results for supercritical airfoils at high incidence, and demonstrate the good correlation between measured and computed shock oscillation frequencies using a closed-loop model based on propagation of disturbances in the separated and inviscid flow regions behind the shock wave. Section 5 gives the theory of two-dimensional wave propagation in nonuniform flows, and the accuracy of Tijdeman's [4] empirical formula of the propagation time for disturbances to travel from the trailing edge to the shock wave is assessed. Examples are given for a NACA 64A006 airfoil. One-dimensional unsteady shock motion in a nonuniform steady flowfield is discussed and expressions are derived to compute the pressure behind a moving normal shock close to the airfoil surface with upstream disturbances. Section 6 uses the linearized equations of motion for compressible two-dimensional flows to analyse the stability of the wake. Using an approximate velocity profile for the near wake, the amplification factors of disturbances are calculated and the frequencies are also computed. It is shown that the shock-induced disturbances on the airfoil surface have frequencies lower than other disturbances with much larger amplification rates that may be excited in the wake. This suggests that at a distance sufficiently far downstream from the trailing edge, the shock-induced disturbances will have little influence on the wake development. Numerical simulation schemes using the Navier–Stokes equations are discussed in Section 7 and the effects of turbulence modelling are pointed out from examples. A less time consuming method using an interactive boundary layer coupled with a transonic small disturbance inviscid code is described and results compared with the Navier–Stokes codes. The

use of passive and active control strategies to either reduce the amplitude of shock oscillation or to move the onset of periodic shock motion to a higher Mach number or incidence angle is discussed in Section 8. This has the potential of expanding the buffet boundaries of transonic airfoils. Finally, some concluding remarks are given in Section 9.

## 2. Shock-induced separation on airfoils

### 2.1. Steady flow separation

#### 2.1.1. Types of separation

In subsonic attached flow past an airfoil, viscous effects are usually assumed to be confined to a thin layer adjacent to the airfoil surface and in the wake. As the Mach number increases, a critical value is reached when somewhere on the airfoil surface the local Mach number becomes unity. Above the critical Mach number, a supersonic region appears which in general is terminated by a shock wave. Further increases in Mach number result in the shock moving rearwards and its strength becomes stronger while the region of supersonic flow grows. When the pressure rise across the shock reaches a sufficiently large value, shock-induced separation of the boundary layer occurs. For a turbulent boundary layer, this starts when the local Mach number just upstream of the shock lies between 1.25 to 1.3 according to Tijdeman [4]. In terms of pressure rise across the normal shock, Pearcey [13] gave a value of 1.4 to 1.5 (equivalent to a Mach number of approximately 1.158 to 1.195) for the RAE 102 and RAE 104 airfoils.

In considering shock-induced boundary layer separation on airfoils, we always encounter a region of mixed supersonic/subsonic flow separated by a shock wave. This is followed by the presence of continuous adverse pressure gradient in the subsonic flow downstream of the shock. Development of upper- and lower-surface boundary layers near the trailing edge and their merging into the wake have significant influence on the circulation, and through it the pressure distribution and shock location. In the case of a lifting airfoil, the boundary layer along the upper surface near the trailing edge tends to be thicker than that on the lower surface. The flow leaves the trailing edge in the direction of the lower surface since the boundary layer carries the highest momentum. The streamlines in the boundary layers and the wake near the trailing edge are curved which result in a traverse pressure gradient.

To determine the circulation, Preston [14] and Spence [15] showed that the flow at the trailing edge must satisfy certain conditions. The Kutta–Joukowski condition, valid for vanishing small viscosity, has to be modified such that the static pressure at the trailing edge is able to recover to the freestream value along the wake in a manner consistent with the changes in displacement thickness

of the wake. Furthermore, the static pressures in the external flow at the two edges of the wake must be related in a manner consistent with the gradient across the wake which is very small in most cases. In other words, the static pressure on the two sides of the wake has to be equal, or nearly equal, since the wake cannot support a pressure difference across it. These are known as the conditions for compatibility and equality of the trailing edge pressure.

At low incidences when shock waves occur on both surfaces, the introduction of a small disturbance at the foot of the upper shock will cause a change in the pressure recovery downstream of the shock. The flow at the lower surface is affected which in turn causes the shock to move rearwards. The static pressure along the wake is also disturbed and in order that the pressure may fall to the freestream value so as to satisfy the compatibility condition, the shock and separation point on the upper surface must move forward. Since it takes a finite time for disturbances to travel from the shock to the trailing edge, oscillations of both shocks are likely before the new steady-state equilibrium is established. Normally, the trailing edge pressure falls rapidly after its initial divergence in response to the changes in the static pressure variations along the wake caused by the development of the separated flow.

Pearcey [13,16] and Pearcey and Holder [17] studied mostly bubble separation. A sketch of this type of separation found commonly in airfoils of conventional design is shown in Fig. 1a where a supersonic region extends along the edge of the bubble downstream of the foot of the shock. This region lies in an area where the pressure increases in the downstream direction causing the streamlines to converge. This offsets the tendency for the shear layer to reattach and delays the closure of the bubble. On the other hand, a local subsonic flow with diverging streamlines would help to promote reattachment. As long as the rise near the forward part of the bubble re-establishes subsonic flow, the bubble size would tend to be self-limited.

In addition to the presence of a bubble separation, rear separation tends to occur and spread forward from the trailing edge for thick or supercritical airfoils. The onset and rate of forward movement depend mainly on the thickness and velocity profile of the boundary layer approaching the trailing edge as well as local pressure gradients. Influence of rear separation will pass directly to the wake and the trailing edge pressure and circulation get immediately affected. Complicated interactions between rear and bubble separations can occur. If the boundary layer is already on the verge of separating near the trailing edge when a bubble separation occurs further forward, this bubble will likely disturb the boundary layer profile sufficiently to trigger rear separation. Pearcey et al. [2] named this type of flow separation as model B to distinguish from the bubble separation which

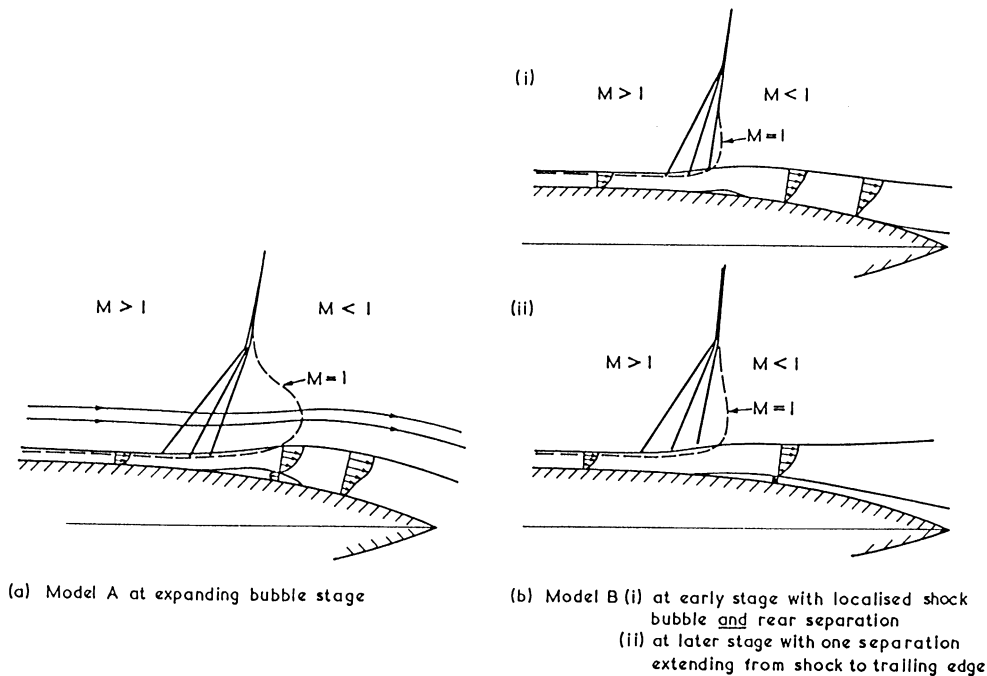


Fig. 1. Sketch illustrating shock boundary layer interaction: (a) bubble separation, (b) bubble and rear separation (from Ref. [2]).

they termed as model A. Fig. 1b illustrates the regions of separated flow and their eventual merging. Fig. 2 shows the various sequences covering practically every possible case of the flow models for shock-induced separation. A common feature of the three variants in model B is that the interaction between the local disturbance at the foot of the shock and the rear separation accelerates the development of the whole shock-induced phenomena at a more rapid rate than that when only bubble separation occurs. The rear separation can be present or incipient when the shock and the separation at the foot of the shock appears. It modulates the rate and magnitude of the flow development, and often dominates it.

### 2.1.2. Position of shock waves

Shock wave positions are measured optically by some investigators whilst others determine the positions from pressure measurements on the airfoil surface. For the later method, a reliable method to locate the shock is given by Blackerby and Cahill [18] where the pressure rise is fitted by a straight line and is extrapolated to a value of pressure corresponding to the local Mach number of unity. The location on the chord where this occurs gives the shock position. The factors that affect the shock wave location are the incidence, freestream Mach number, and airfoil configuration.

**2.1.2.1. Increasing incidence.** With the freestream Mach number held constant, an increase in incidence increases

the local Mach number at fixed points upstream of the shock wave. For small bubble at the shock, the disturbance dies out before reaching the trailing edge where the pressure is practically unaffected by the change in incidence. As the bubble grows in size, it will affect the trailing edge pressure causing divergence when the separation bubble reaches the trailing edge. Further increase in incidence results in a greater decrease in trailing edge pressure and a stronger disturbance at the wake. Pearcey [16] showed that for a 6% thick RAE 104 airfoil at Mach numbers between 0.7 and 0.95, the shock initially moves downstream with incidence until a value is reached where any further increase will cause the shock to move forward. This will allow pressure recovery to begin with a higher initial pressure and a less severely separated flow in order to satisfy the compatibility condition.

**2.1.2.2. Increasing Mach number.** The behavior in shock wave position with increasing Mach number is quite similar to that for increasing incidence. In this case, the freestream pressure falls as the Mach number increases, and the separation becomes more severe due to the stronger local Mach number ahead of the shock wave. The airfoil shape determines the local Mach number ahead of the shock and hence controls the onset of separation as well as the rate at which the shock moves over the surface. Pearcey [16] showed that for a 6% thick RAE-104 conventional airfoil at two relatively low incidence of 2 and 3.7° and Mach numbers up to 0.95, the

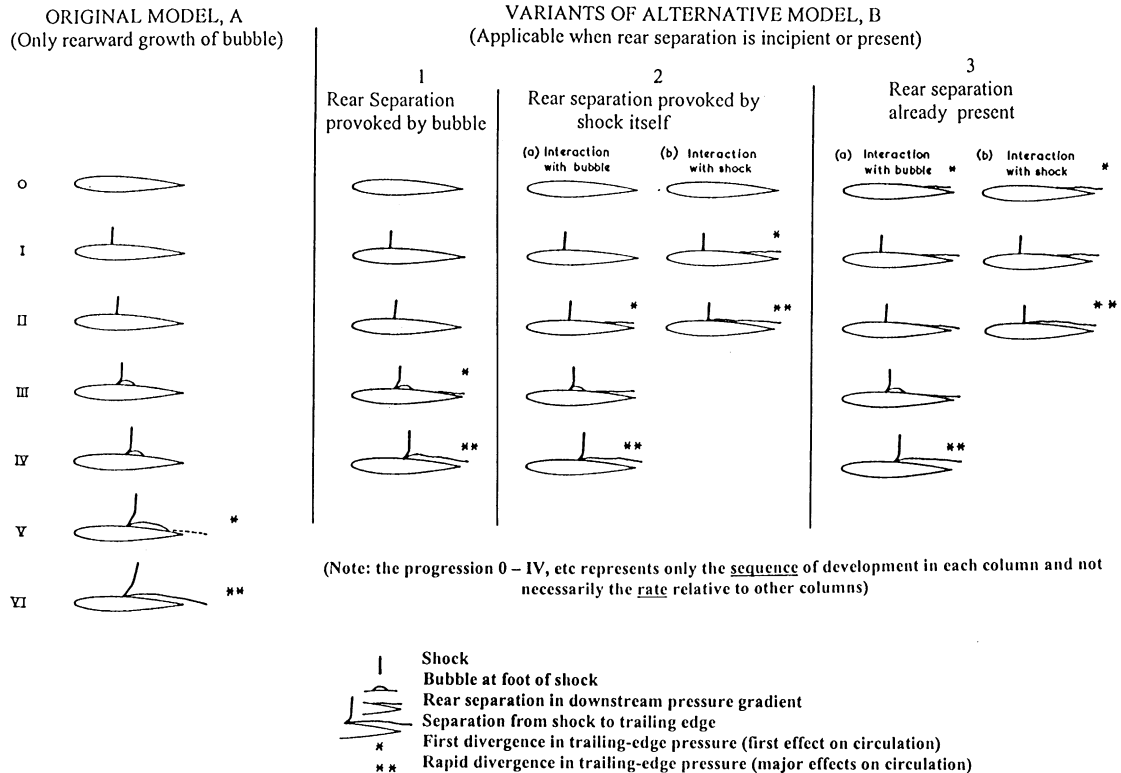


Fig. 2. Model A and Model B flow separation according to Pearcey et al. (from Ref. [2]).

rearward moving shock does not reverse in direction and moves upstream. However, for thick airfoil sections such as those found in supercritical airfoil design, a forward moving shock may occur for sufficiently high freestream Mach numbers.

**2.1.2.3. Effects of trailing-edge flap.** Forward or rearward shock movements can be controlled by changes in downstream pressure caused by the deflection of a trailing-edge flap. Upward (negative) deflection increases the pressure at the rear of the airfoil upper surface and causes the shock to move forward while the opposite is true for positive deflection. Lee [19] investigated the shock positions for a 16% thick supercritical airfoil (WTEA II) for various combinations of Mach number, incidence and flap angles. As an example, he presented some results at an incidence angle of  $3^\circ$ . Variations in shock position with Mach number at different flap angles show the rearward movement of the shock gradually slows down before starting to move upstream. The curves of shock position with changes in incidence depend on the Mach number. For a value of Mach number below 0.792 and with various flap angles, the shock moves downstream with incidence and shows a tendency to move forward once the extreme rearward position has been reached. However, at  $M = 0.792$ , only forward shock motion with

increasing incidence was detected for the cases presented by Lee [19] where only three flap angles ( $\delta = -4^\circ, 0^\circ$ , and  $14^\circ$ ) were considered.

### 2.1.3. Time-averaged airfoil surface pressure, skin friction and wake properties

Most of the pressure and velocity measurements in the separated flow regions of two-dimensional conventional airfoils were conducted to validate computer code or to provide guidance in turbulence modelling. Studies carried out on conventional airfoils include the NACA 0012 [20], NACA 64A010 [21,22], and 18% thick circular arc airfoils [6,23,24]. For supercritical airfoils, investigations have been carried out on a modified Whitcomb [25], CAST7/DOA1 [26], BGK No.1 [9,27], and WTEA II [28–30] airfoils in an attempt to obtain a better understanding of the flow past supercritical airfoils at nonoptimized conditions. Some of the results presented in the above references are at conditions where the shock waves are stationary, but at the high Mach number and incidence range, the shock waves are unsteady. Measurements given by various investigators, though not specifically stated, are in all likelihood time averaged.

Using holographic interferometry, Johnson [21] mapped the Mach number contours (Fig. 3) around a NACA 64A010 airfoil at  $M = 0.8$ ,  $Re_c = 2 \times 10^6$ , and  $\alpha = 6.2^\circ$ .

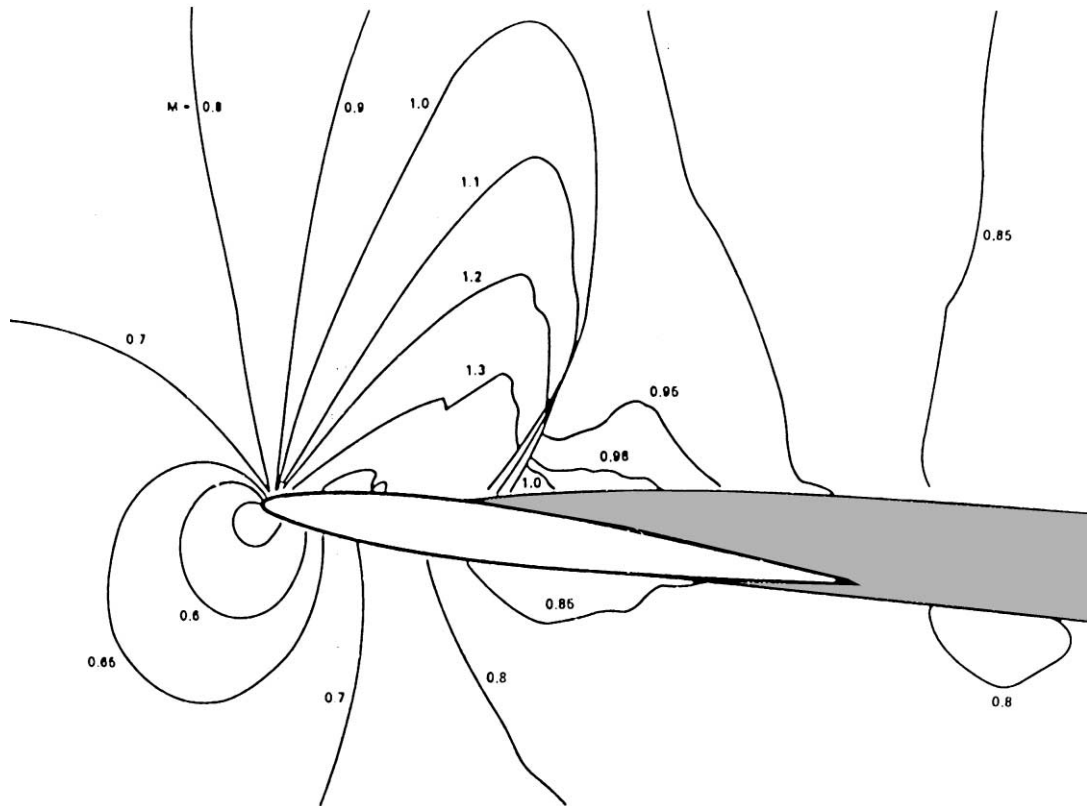


Fig. 3. Mach number contours obtained from interferograms of a NACA 64A010 airfoil at  $M = 0.8$ ,  $\alpha = 6.2^\circ$  and  $R_{cc} = 2 \times 10^6$  (from Ref. [21]).

A small local region of supersonic flow is detected which slowly decelerates downstream. The mean velocity profiles illustrated in Fig. 4 show relatively small reversed velocities observed in the separated flow region on the airfoil upper surface where the skin friction is near zero. Near the trailing edge, the wake closes rapidly and there is a sharp upward displacement of the near wake. Johnson et al. [22] also proposed a model of the near wake velocity recovery and flow angle development with streamwise distance based on the results they obtained at  $\alpha = 6.2^\circ$  and  $M = 0.8$ . In Fig. 5, they postulated that there is no net flow of fluid from the lower surface boundary layer at the trailing edge into the upper surface. Instead there is a net downward flow of the slow moving fluid above the airfoil's upper surface into the lower surface viscous layer as a result of entrainment resulting in flow angles near  $90^\circ$ . Further downstream, due to mixing with the lower stream high energy layer, the flow takes on a wake character with the minimum mean streamwise velocity occurring above the trailing edge of the airfoil. In numerical simulation of the near wake, Johnson et al. [22] found this entrainment process has to be taken into account to give reasonable prediction of the near wake flow development.

Rear separation provoked by a bubble at the shock was investigated by Lee [27] from skin friction measurements on the BGK No. 1 airfoil using a Preston tube. For this airfoil, separation at low Mach numbers can begin as a bubble behind the shock wave and spread downstream as the angle of attack increases. Trailing edge separation occurs when the incidence angle  $\alpha$  reaches a critical angle. The rear separation region moves rapidly upstream and merges with the shock-induced bubble separated flow region. Fig. 6 shows superimposed on time-averaged pressure distribution plots the locations of the separated flow regions for varying incidence. At  $\alpha = 4.95^\circ$ , the bubble is approximately 8% chord in size. When  $\alpha$  increases to  $6.43^\circ$ , trailing edge separation moves to  $x/c = 0.82$ , and the two separated flow regions are approximately 0.23 chord apart. The rear separation region moves upstream much more rapidly than the downstream motion of the separation bubble. At  $\alpha = 6.94^\circ$ , the two separation regions have completely merged and the flow is fully separated.

## 2.2. Surface pressure fluctuations in separated flows

The classification of the types of flow separation by Pearcey et al. [2] is based on a stationary shock

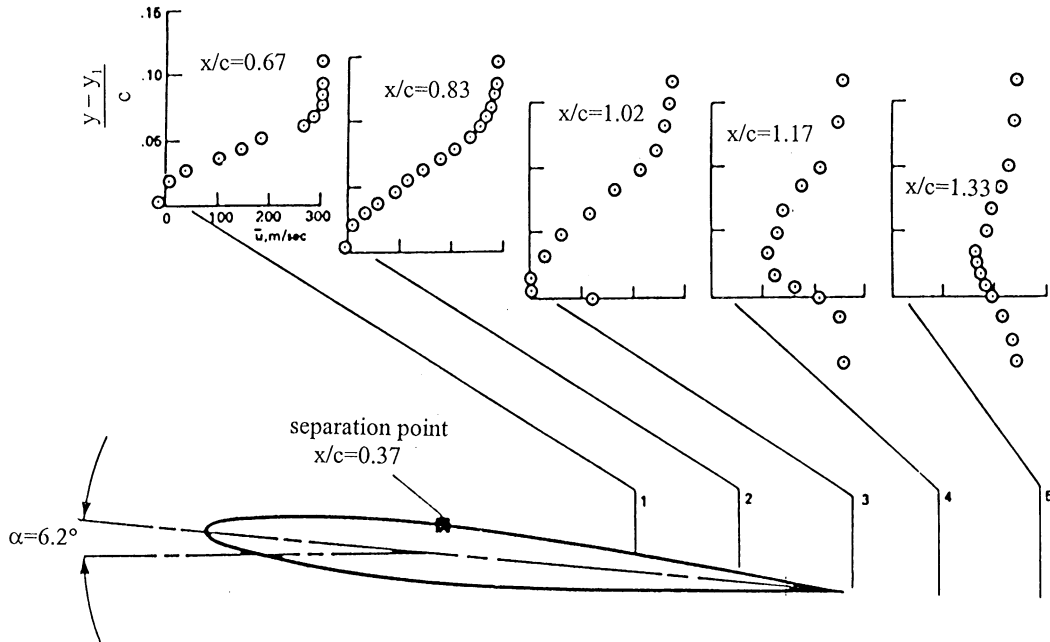


Fig. 4. Mean velocity profiles of a NACA 64A010 airfoil at  $M = 0.8$ ,  $\alpha = 6.2^\circ$  and  $R_{e_c} = 2 \times 10^6$  (from Ref. [21]).

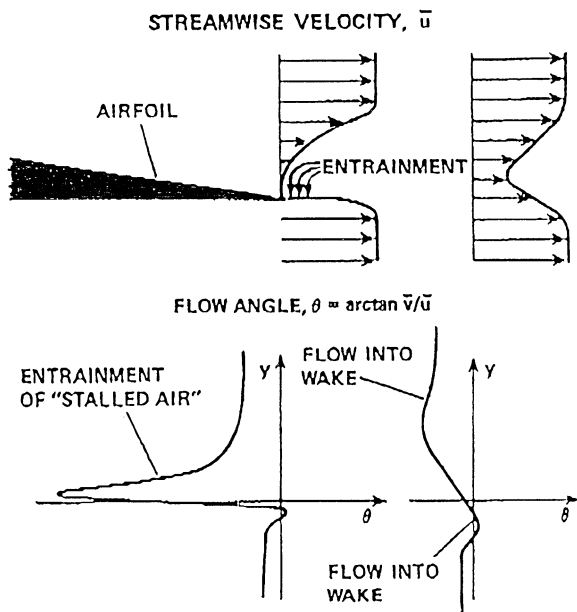


Fig. 5. Trailing edge flow model of a NACA 64A010 airfoil (from Ref. [22]).

interacting with a turbulent boundary layer. Eventhough the pressure in the separated flow is unsteady, time-averaged measurements can be made to identify regions where bubble or rear separation occurs on the airfoil. There are

ranges in the Mach number or incidence angle where the shock waves become very unsteady. Measurements [5] of the pressure fluctuations at transonic speeds have been carried out as early as the 1950s, and more detailed studies were reported in Refs. [3,6,8–11,24,25,27,31–33].

From unsteady pressure measurements on a 11.7% thick NACA 16 series airfoil, Mundell and Mabey [3] classified shock-boundary layer interactions into three types based on the level of excitation of the pressure on the airfoil surface. For a fixed freestream Mach number, the effect of varying incidence can be summarized in Fig. 7 where at low incidence type 1 flow represents a weak shock boundary layer interaction. Upstream of the shock wave, the pressure fluctuations are small for all frequency components having values typically of those beneath a turbulent boundary layer. Close to the shock, the fluctuations are also small and they occur mainly at low frequencies. At a short distance from the shock, the pressure fluctuations decay and revert to the tunnel level.

By increasing the angle of incidence, type 2 flow occurs when the shock is sufficiently strong to induce separation which is followed by reattachment. This is similar to the model A bubble separation described by Pearcey et al. [2]. The time-averaged boundary layer thickness increases and further increases in incidence will cause divergence of the mean pressure at the trailing edge. The five regions on the airfoil surfaces where there are noticeable differences in the characteristics of the pressure fluctuations are denoted in Fig. 7.

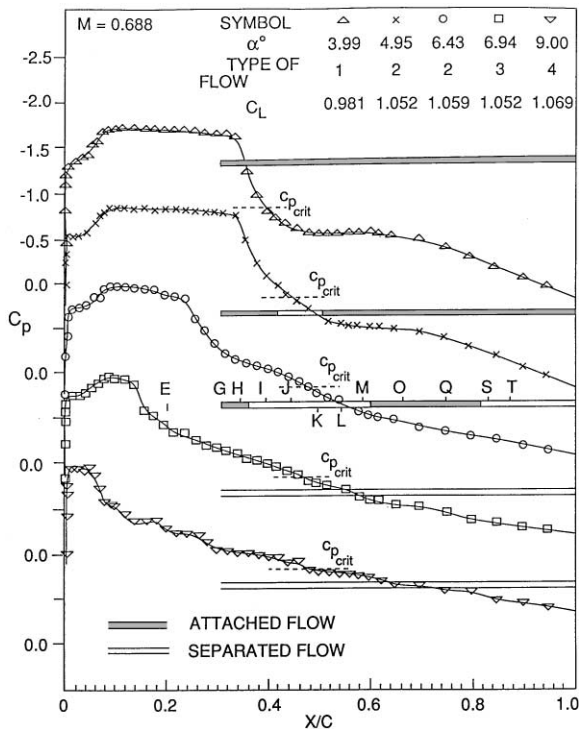


Fig. 6. Steady-state pressure distributions and separation regions of BGK No. 1 airfoil (from Ref. [27]).

Type 3 flow occurs when the strong shock separates the turbulent boundary layer which does not reattach to the airfoil. In the time-averaged flow, the main change is the thick separated shear layer at the trailing edge which closes a short distance downstream to form the wake. There are now three identifiable regions with pressure fluctuation characteristics given in Fig. 7. Mundell and Mabey [3] demonstrated the existence of these three types of flow from pressure measurements on the NACA 16 series airfoil at a fixed  $\alpha = 3.6^\circ$ , and varying  $M$  from 0.70 to 0.82.

An investigation of the pressure fluctuations on the BGK No. 1 supercritical airfoil was carried out by Lee [10,27]. By keeping Mach number fixed at  $M = 0.688$  and varying incidence angle from  $\alpha = 3.99^\circ$  to  $9^\circ$ , he detected the types of shock-boundary layer interaction proposed by Mundell and Mabey [3]. In his experiments, Lee [10,27] installed fast response pressure transducers on the airfoil upper surface at  $x/c$  between 0.2 to 0.87 and measured the rms pressure coefficient  $C'_p = p_{rms}/q$  which is shown in Fig. 8. The letters *E, G, ..., T* in the figure denote the location of the pressure transducers. The corresponding time-averaged pressure measurements from 70 pressure orifices on the airfoil upper and lower surfaces are shown in Fig. 6.

Type 1 interaction is shown in Fig. 6 in the form of time-averaged pressure coefficient  $C_p$  on the airfoil upper

surface at  $M = 0.688$  and  $\alpha = 3.99^\circ$ . The curves for different  $\alpha$  are displaced downwards by one unit of the vertical scale to avoid overlapping. Skin friction coefficients between 30 and 95% chord show the flow to be attached. The corresponding pressure fluctuations are shown in Fig. 8 where the peak intensity occurs behind the shock wave at  $x/c = 0.35$ . The pressure intensity decreases very rapidly behind the shock to a value close to the tunnel level.

Increasing the incidence to  $4.95^\circ$  results in the formation of a small bubble at the shock-boundary layer interaction region. This occurs at  $x/c$  from approximately 0.42 to 0.50 determined from skin friction measurements where  $C_f = 0$ . At this value of  $\alpha$ , Fig. 8 shows that in addition to the large peak behind the shock, there is a second peak of smaller magnitude located at  $x/c$  about 0.45. The second peak is slightly in front of the center of the separated bubble and this type of flow corresponds to the type 2 flow. The pressure fluctuation levels are practically constant in the reattached flow region which extended to the trailing edge of the airfoil. They are slightly higher than the tunnel level averaged for the values of  $\alpha$  considered. At  $\alpha = 6.43^\circ$ ,  $C_p$  plots show a shock-induced separation bubble between  $x/c = 0.36$  and 0.60 in addition to a rear separation region starting at a position  $x/c = 0.82$ . The corresponding pressure fluctuation plots in Fig. 8 show the bubble given by the curve HIJKLM. The peak pressure intensity inside the bubble occurs at transducer J ( $x/c = 0.45$ ) which is slightly in front of the center of the separated flow region. The intensity reaches a minimum at transducer M ( $x/c = 0.591$ ) which is very close to the reattachment point determined from skin friction measurements. The difference in the location of the reattachment point is due to the spatial inaccuracies of the two sets of measurements. This type of flow corresponds to model B described by Pearcey et al. [2]. It was not observed by Mundell and Mabey [3] and is probably sensitive to scale effects. The pressure fluctuations still possess the general characteristics of the type 2 flow.

Increasing  $\alpha$  to  $6.94^\circ$  causes the flow to be fully separated. It is seen that the intensity distribution behind the shock wave still shows a bulge which is typical for flows with a separation bubble. Skin friction measurements show that the two separated flow regions have just merged and the flow is fully separated. At this stage of flow separation, some of the unsteady characteristics of the separation bubble and rear separation region are still preserved. The flow resembles the type 3 shock-boundary layer interaction described by Mundell and Mabey [3]. At  $\alpha = 9^\circ$ , the flow becomes very unsteady and large shock wave motion is detected. A typical intensity distribution curve for this class of flow is shown in Fig. 8 where a very gradual decrease in the pressure fluctuation intensity towards the trailing edge is seen. This type of flow was not included in Mundell and Mabey [3] classification of shock-boundary layer interaction and Lee [27]

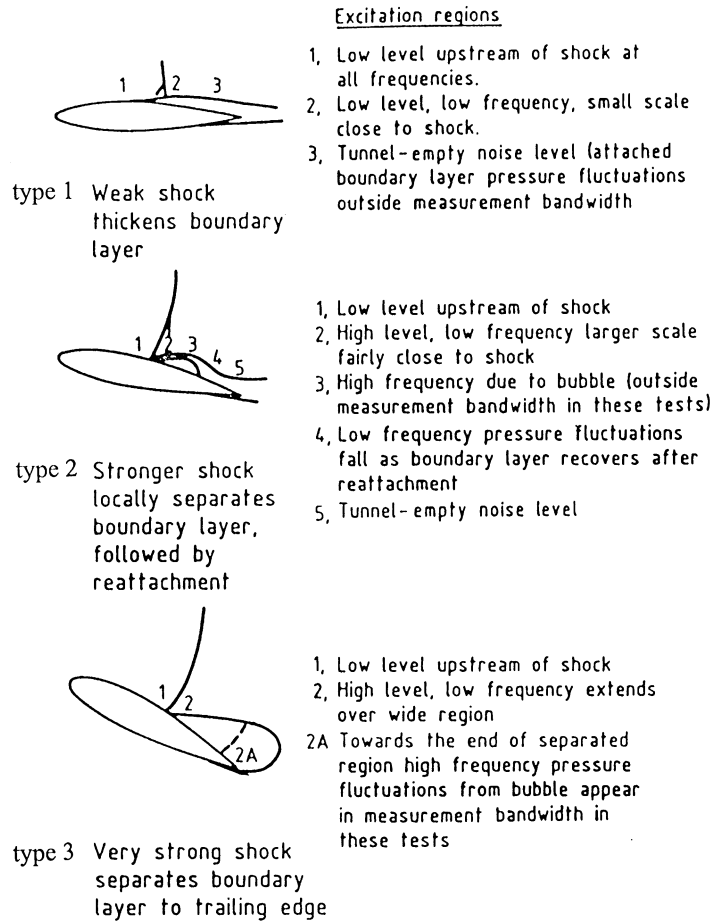


Fig. 7. Classification of shock boundary layer interactions and excitations on airfoils (from Ref. [3]).

designated it as type 4 flow. It should be noted that the classification of the flow by Pearcy et al. [2] and Mundell and Mabey [3] is essentially similar except that the latter approach makes use of the unsteady pressures to identify the type of flow arising from shock-boundary layer interaction.

### 3. Transonic buffeting of airfoils

#### 3.1. Buffet boundaries

Buffeting is the dynamic response of an aircraft structure, such as a wing, to unsteady forces acting on it. After the tragic accident [34] at Meopham, England, on July 21, 1930 when a Junkers F 13 monoplane encountered tail buffeting and crashed killing all the passengers and pilots, a number of investigations was conducted on this subject. Earlier studies were primarily concerned with the response of the horizontal tail submerged in the wake of the wing, or to the effect of gusts and turbulence on the

vibration of the wing. The introduction of supercritical wing design in the early seventies renewed interest in this subject although some buffeting research at transonic flow conditions have been conducted at NACA in the early fifties [35–37].

In this review, we concentrate only in transonic buffeting since the buffet loads are far more severe than those at low subsonic or supersonic speeds, and hence is of greater concern from aircraft maneuverability and structural integrity considerations. The process is essentially driven by the interaction of the shock wave with the boundary layer which influences the development of the shock-induced separation bubble or rear separation as discussed in Section 2. As a result of the change in flow conditions at the airfoil trailing edge, Pearcy [13] showed that the circulation or lift variations produced by the separation process is mainly responsible for the buffet loads. In principle, the magnitude of the buffet loads can be estimated from the magnitude of the divergence of the trailing edge pressure.

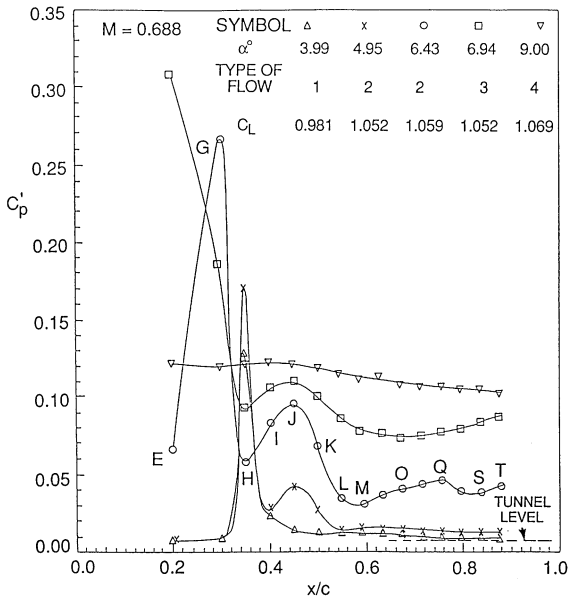


Fig. 8. Pressure fluctuations on upper surface of BGK No. 1 airfoil (from Ref. [27]).

An example of one of the early definitions of the buffet boundary illustrated in a lift versus Mach number plot is shown in Fig. 9. Thomas [38] defined the onset boundary to be a curve separating the regions where the flow is essentially attached or partially separated and those where the flow is totally separated. In the subsonic region the boundary coincides with the maximum lift versus Mach number curve. As the flight speed is increased, a shock wave is formed and it moves rearwards and

finally reaches the trailing edge of the airfoil. Separation will disappear and we have a buffet-free supersonic flow. For thin wings at small incidence  $\alpha$ , this condition can be reached even before the shock wave has attained an intensity great enough to initiate buffeting. There is a buffet-free corridor whereby it is possible for a suitably designed supersonic aircraft to pass through the transonic region without encountering buffeting. For cruising flight, the design point is situated at sufficiently safe values of  $\Delta C_L$  and  $\Delta M$  from the buffet boundary such that normal flight maneuvers and acceptable gust intensity will not bring the aircraft beyond the buffet onset boundary.

The onset of buffet is defined similarly for fighter and transport aircraft, but the permissible operation of the aircraft after excursion into the buffet regime is different. For a combat aircraft, light buffeting is defined as the first appearance of sizable vibrations noticed by the pilot and the aircraft can safely operate in that regime. The margin set for moderate buffeting represents the highest values of instantaneous pull-up or turn rates at which the weapon platform may still be effective in releasing stores or carrying out a tracking mission. Heavy buffet is determined by the structural limits of the aircraft and should be avoided at all costs.

For transport aircraft during normal cruise, the aircraft may encounter a strong gust which carries it over the buffet boundary. However, excursion inside this boundary for any prolonged period of time is not permissible. The performance of the aircraft is related to the conditions at buffet onset which is very close to the drag rise Mach number.

One of the earliest methods to determine buffet onset is described by Pearcey [16] and Pearcey and Holder [17]

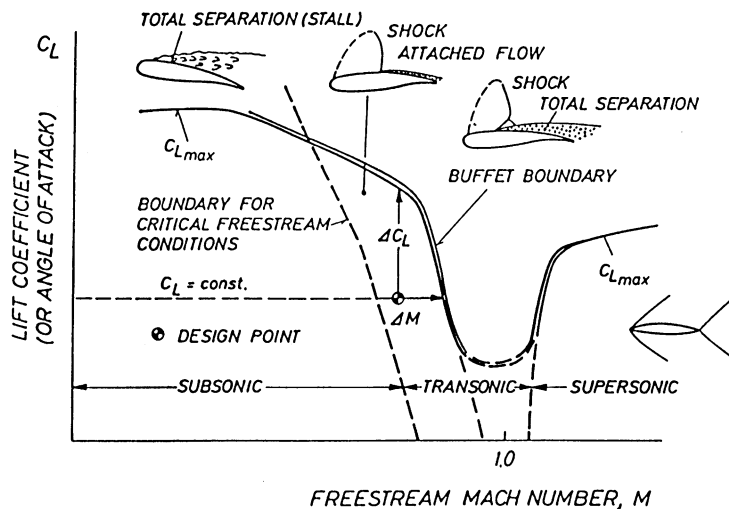


Fig. 9. Buffet boundary (from Ref. [12]).

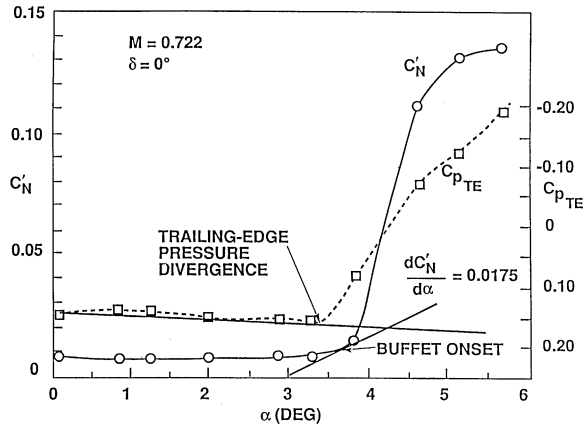


Fig. 10. Comparison of buffet onset determined from divergence of normal force fluctuations and trailing edge pressure (from Ref. [29]).

who considered only airfoils encountering bubble separation. Buffet onset is determined by the Mach number or incidence when the bubble reaches the trailing edge and bursts. This can be obtained quite readily from the divergence of the trailing edge pressure. Other methods using unsteady forces or pressure measurements are described by Polentz et al. [36] and Mabey [39]. In two-dimensional airfoil testing, a convenient quantity to use is the unsteady normal force obtained either from integration of unsteady pressures on the airfoil surfaces or from direct measurement with a force balance. Lee and Tang [29] used the divergence of this quantity to define the buffet boundary and found consistent results in their investigation of supercritical airfoils. In a plot of the rms value of the normal force coefficient  $C'_N (= N_{rms}/qsc)$  against  $C_L$ , the buffet onset is determined by the slope  $dC'_N/dC_L = 0.1$ . This value is arbitrary chosen but it gives consistent results and compares well with other methods. The method is illustrated in Fig. 10 where  $C'_N$  is plotted against  $\alpha$  for the 16% thick WTEA II supercritical airfoil [29]. The buffet onset is determined from the slope  $dC'_N/d\alpha = C_{Lx} dC'_N/dC_L = 0.1 C_{Lx}$ . Using the divergence of the trailing edge pressure, a slightly lower value is obtained for the incidence angle when buffet onset sets in. For this particular airfoil, it is known that rear separation is provoked by the shock itself and the flow belongs to model B shown in Fig. 2. In carrying out buffet investigations on a Whitcomb-type airfoil, Roos [32] found that unlike a conventional airfoil, buffet onset for a supercritical airfoil does not develop simultaneously with divergence of the trailing edge pressure. Roos [32] gave an example from flight test results [40] of the NASA F-8 supercritical wing aircraft, and commented that the trailing edge pressure divergence criterion did not give the correct buffet boundary. There are advantages in

using the fluctuating normal force from a force balance to determine buffet onset. Installation of a pressure transducer close to the trailing edge is cumbersome and is not feasible for airfoils with thin trailing edge. Also, it is often necessary to obtain trailing edge pressure data over a wide range of incidence below buffet onset to define a baseline to locate  $\alpha$  when trailing-edge pressure divergence occurs.

Buffet boundaries for two-dimensional airfoils can also be computed using methods based on boundary layer theory. Thomas [38] was perhaps the first to determine the separation point and drew conclusions concerning the buffeting phenomenon. The method assumes separation to reach the shock from the trailing edge since it cannot satisfactorily compute the more complex bubble separation case. For a given  $\alpha$ , the buffet onset Mach number is given by  $dx_{sep}/dM = 0$ , where  $x_{sep}$  is the separation point measured from the trailing edge. There are flow conditions when the variation of the separation point with  $M$  does not follow a smooth curve and discontinuities are present. Also, there are cases that by the time the separation point reaches the shock, the buffet intensity is already very large. An arbitrary criterion at buffet onset is chosen by Thomas [38] when the separation point reaches  $x/c = 0.9$ . For model A flow, he found that at a certain Mach number the separation can suddenly jump from the trailing edge to the shock, and he assumed this Mach number to coincide with that for a bubble separation which burst at the trailing edge. In a later paper, Thomas and Redeker [41] used the  $x/c = 0.9$  criterion on the NACA 65-213, NPL 4111 and RAE 103 airfoils and showed good agreement with wind tunnel measurements. Redeker and Proksch [42] used Bauer et al. [43] supercritical airfoil computer code and Thomas [38] boundary layer method to determine the onset boundary for the BGK No.1 airfoil. The results shown in Fig. 11 compare quite favorably with the experimental data from Kacprzynski [44].

### 3.2. Beyond the buffet boundary

For conventional airfoils, it is often useful to designate in a  $C_L$ - or  $\alpha$ -versus  $M$  plot the regions of mild, moderate or heavy buffeting. For supercritical airfoils such as those investigated by Lee et al. [45], buffet occurs so close to  $C_{Lmax}$  for Mach numbers near the design value that it is not too meaningful to assign a degree of severity in the  $C_L$ - or  $\alpha$ - $M$  plots. Lee and Ohman [46,47] have shown that for the BGK No. 1 airfoil, large fluctuations in normal forces are detected near the “elbow” of the buffet boundary at  $M$  approximately 0.733. It is shown in Fig. 11 that the airfoil can experience a large  $C'_N$  from a small excursion into the buffet regime at transonic flow conditions. The source of this behavior is associated with the presence of periodic shock motions. Fig. 12 shows the region where shock oscillations [48] occur for the BGK

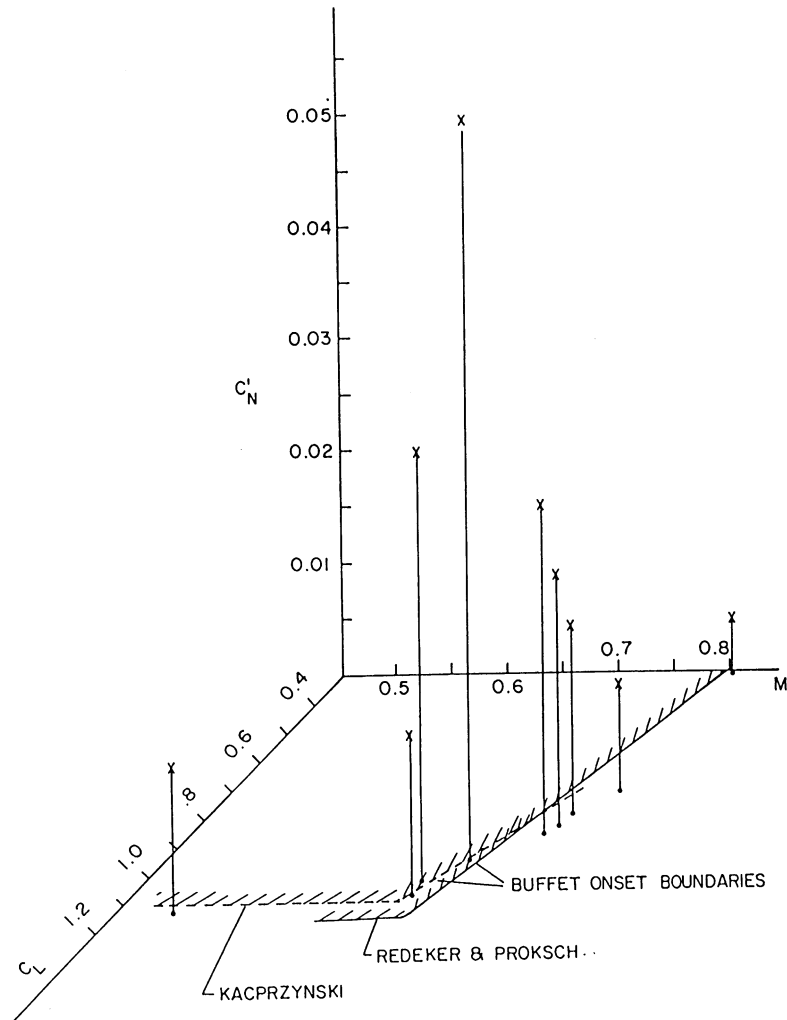


Fig. 11. Variation of  $C'_N$  with  $M$  and  $C_L$  (from Ref. [48]).

No. 1 airfoil. Comparison with Fig. 11 shows the region where large values of  $C'_N$  is detected lies inside the shock oscillation region. This region where discrete frequency shock oscillations occur increases in dimension for thicker supercritical airfoils, such as the 16% thick WTEA II airfoil [19].

The excursion into the buffet regime is shown in Fig. 13 where  $\alpha$  is fixed at approximately  $6^\circ$  and Mach number varied from 0.6 to 0.81. The results obtained by Lee [10,48] for the BGK No. 1 airfoil show the fluctuating normal force  $C'_N$  to increase almost linearly from  $M = 0.6$  to  $0.69$ . The onset boundary is crossed at  $M = 0.615$  and the shock oscillation region begins at  $M = 0.67$ . Between  $M = 0.67$  and  $0.69$ , the shock is very weak and  $C'_N$  continues to increase approximately in a linear manner. A maximum  $C'_N$  is located at  $M = 0.733$  close to the design value of  $0.75$ . The slope  $dC'_N/dM$  for

$0.616 < M < 0.69$  is much smaller than that for  $0.69 < M < 0.733$  where fairly strong shock oscillations occur in the latter range of  $M$ . At the higher values of Mach numbers ( $M > 0.733$ ), the shock weakens and the pressure field due to shock oscillations decreases with increasing  $M$ , resulting in a decrease in  $C'_N$ .

Lee [10,19,48] gave results of the fluctuating normal force variation with  $\alpha$  for a given  $M$  as the airfoil penetrates into the buffet regime. Close to the design Mach number, curves of  $C'_N$  versus  $\alpha$  for constant  $M$  show the increase in buffet intensity to be very rapid as soon as the boundary is crossed. Classification of light, moderate and heavy buffet usually involves only a small change in  $\alpha$  and is difficult to determine accurately.

Oscillatory shock motions during transonic buffeting on supercritical airfoils have also been observed by Roos and Riddle [25] and Stanewsky and Basler [12]. These

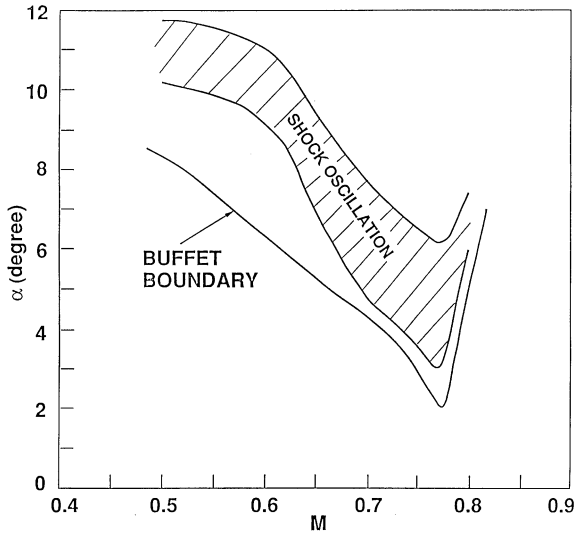


Fig. 12. Region of shock oscillation for BGK No. 1 airfoil (from Ref. [48]).

studies deal with the pressure flow field characteristics [25] and mechanisms [12] of periodic shock motion, and will be discussed in the next section.

In studies of shock-induced separation on circular-arc airfoils, McDevitt et al. [6] and Mabey et al. [7] also detected periodic shock oscillation in experiments carried out at zero incidence for different thickness to chord ratios. This situation is somewhat different from an aircraft wing experiencing buffeting where normally the wing is at an angle of incidence and flow separation occurs mainly on the upper surface. McDevitt et al. [6] and Mabey et al. [7] found this type of oscillatory shock motion to occur in a very narrow range of transonic Mach numbers and is usually sensitive to scale effects. An example of the periodic shock boundary in a  $R_{ec}$  versus

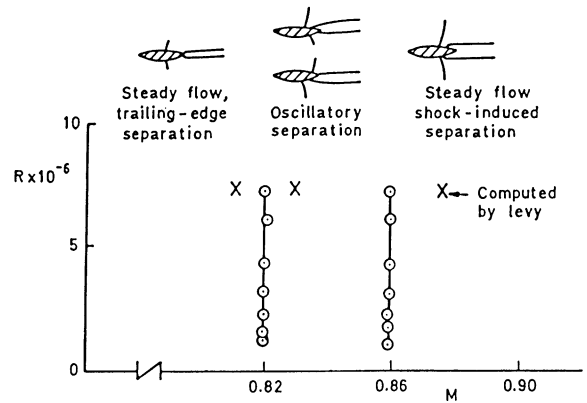


Fig. 14. Flow domains for a 14% thick biconnex airfoil  $\alpha = 0^\circ$  fixed transition (from Ref. [7]).

$M$  plot is shown in Fig. 14 for a 14% thick circular arc airfoil. The range of Mach numbers where shock oscillation occurs is very small varying from 0.82 to 0.86, compared with the range  $0.5 < M < 0.8$  for the BGK No. 1 airfoil when buffeting is experienced. Thick symmetrical airfoils at zero incidence or lift are often used as model supports in wind tunnel testing.

#### 4. Experimental studies on periodic shock oscillations

##### 4.1. Types of shock motion

In discussions on periodic shock motions over airfoils, many authors refer to the type of shock oscillations proposed by Tijdeman [4]. It is useful to briefly review his investigations for later discussions. The experiments were carried out on a NACA 64A006 airfoil with a trailing-edge flap located at the three-quarter chord point

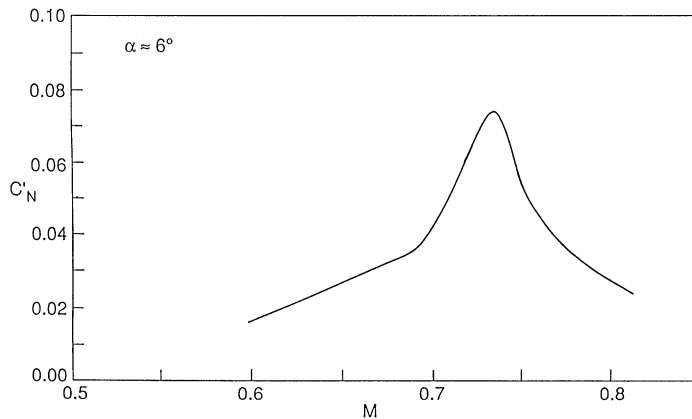


Fig. 13. Variation of  $C_N$  with  $M$  at  $\alpha$  approximately  $6^\circ$  (from Ref. [48]).

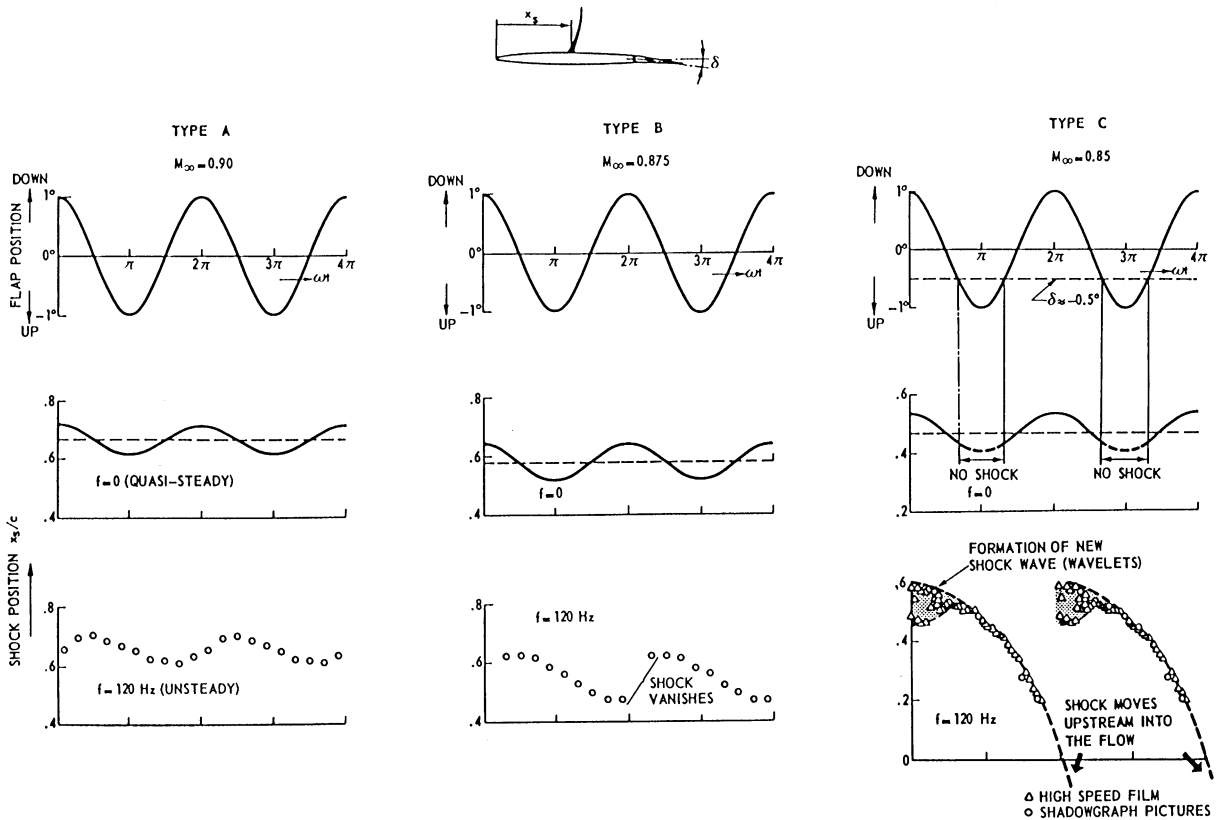


Fig. 15. Types of periodic shock wave motion (from Ref. [4]).

and  $R_{ec}$  was approximately  $2 \times 10^6$ . The flap was forced to oscillate sinusoidally and the mean angle, frequency and amplitude were set independently. The unsteady pressure distributions exhibit a large pressure peak at the leading edge of the flap, and for qualitative analysis of the disturbance flowfield, the flap can be represented by a point source.

Tijdeman [4] carried out his investigations at  $\alpha = 0^\circ$ , zero mean flap deflection ( $\delta = 0^\circ$ ), amplitude and frequency of oscillations at  $1^\circ$  and 120 Hz, respectively. Time histories of the shock wave motion recorded from shadowgraph pictures and high-speed photography show the existence of three types of shock wave motion.

The type A shock oscillation is detected at  $M = 0.9$ . The shock position given in Fig. 15 shows an almost sinusoidal motion having a phase shift relative to the flap deflection. The quasi-steady shock location is also shown for reference and as expected, there is no phase shift with respect to the position of the flap. The instantaneous shock positions on the upper and lower surfaces of the airfoil are shown in Fig. 16 at various phases during the period of an oscillation cycle. It can be seen that due to the symmetry of the airfoil, the two shocks move in anti-phase.

When the Mach number is decreased to  $M = 0.875$ , type B shock motion is observed. The quasi-steady shock position is still approximately sinusoidal following the flap displacement without any lag. However, dynamic effects cause the unsteady flowfield to behave differently than the type A motion. The shock motion is still periodic, but during a portion of the cycle, the shock becomes very weak and photographic studies show it degenerates into weak pressure waves. The shock wave time history and instantaneous shock positions at different times in an oscillation cycle are shown in Figs. 15 and 16.

At  $M = 0.85$ , type C flow emerges. The periodic shock motion is quite different from the two types previously described. In Figs. 15 and 16 we see that at about  $x/c = 0.6$ , weak compression waves coalesce to form a shock which moves upstream into the flow. After exiting from the leading edge of the airfoil, weak compression waves are again formed at  $x/c$  approximately 0.6 and the process repeats itself. There is no downstream motion of the shock wave and this process repeats periodically and alternates between the upper and lower surfaces. For the quasi-steady flow, the shock wave is replaced by weak compression waves during a part of the cycle.

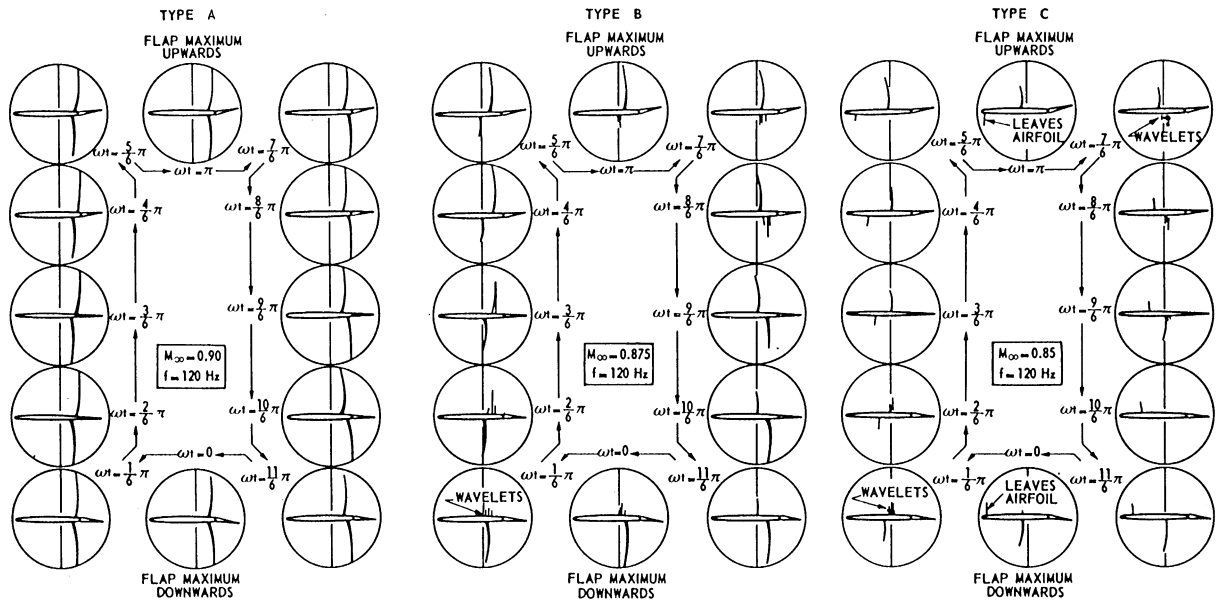


Fig. 16. Time histories of the periodic shock wave motions (from Ref. [4]).

Using the inviscid transonic small disturbance equation [49], type A and B periodic shock motions can also be predicted for an airfoil performing pitch and plunge motions. Tijdeman [4] conducted tests on the NLR 7301 airfoil and showed that these two types of shock motion are possible for forced pitching motion, but very little data are available on supercritical airfoils with oscillating flaps. For an airfoil at incidence experiencing transonic buffeting, shock waves are usually present only on the upper surface. Lee and Tang [29,30] carried out some studies on the 16% thick WTEA II supercritical airfoil with a 14% chord length trailing-edge flap. They obtained pressure distributions and shock locations for quasi-steady flow using various  $M$ - $\alpha$ - $\delta$  combinations. Since their studies were conducted close to the buffet boundary, the behavior of the shock wave with flap angles similar to those at zero incidence described by Tijdeman [4] was not observed.

#### 4.2. Biconvex circular-arc airfoils

McDevitt et al. [6] conducted tests on an 18% thick biconvex circular-arc airfoil at  $Re_c$  between  $1 \times 10^6$  and  $17 \times 10^6$  covering laminar to fully developed turbulent flows. By varying the peak Mach number  $M_1$  just in front of the shock from about 1 to 1.4, weak and strong shock boundary layer interactions were observed. Unsteady pressure measurements were taken at  $x/c = 0.5$  and 0.775, and these measurements show periodic motion of the flow to be asymmetric and the shock movement on the upper and lower surfaces is exactly  $180^\circ$  out of phase. High speed shadowgraph movies were

taken of the flow over the aft portion of the airfoil as  $M$  was varied from 0.74 to 0.785 at a rate  $dM/dt = 0.001/s$ , and the results show that on the airfoil surfaces, alternate shock-induced and trailing-edge separation occur. McDevitt et al. [6] suggested that during a particular phase of the oscillation cycle when the peak Mach number  $M_1$  ahead of the shock on the upper surface is above the critical value, shock-induced separation will occur. The shock on the lower surface, being closer to the trailing edge, will induce rear separation. The effective airfoil profile is no longer symmetrical and the effect of negative camber is to slow down the flow over the upper surface. This tends to suppress the shock-induced separation phenomenon but at the same time induces higher velocities over the lower surface, thus promoting shock-induced separation, and the flowfields reverse. When the freestream  $M$  is increased to a value sufficiently above the critical, the oscillatory behavior ceases and both surfaces experience steady, shock induced separation.

McDevitt [50] carried out more detailed studies on the biconvex circular-arc 18% thick airfoil, and extended the original study to include effects of angle of attack, and leading and trailing edge splitter plates. The frequency of oscillation was found to vary very slightly from  $Re_c = 1 \times 10^6$  to  $17 \times 10^6$  at  $188 \pm 3$  Hz throughout the  $Re_c$  range tested. The reduced frequency  $\kappa$  is approximately 0.99, which is smaller than Finke's [51] value of 1.13 for a 20% thick airfoil at  $\alpha = 0^\circ$ . Fig. 17 shows the regions where periodic shock oscillations occur for increasing and decreasing  $M$  at a rate of  $dM/dt = \pm 0.001$ . The right-hand boundaries are essentially the same but

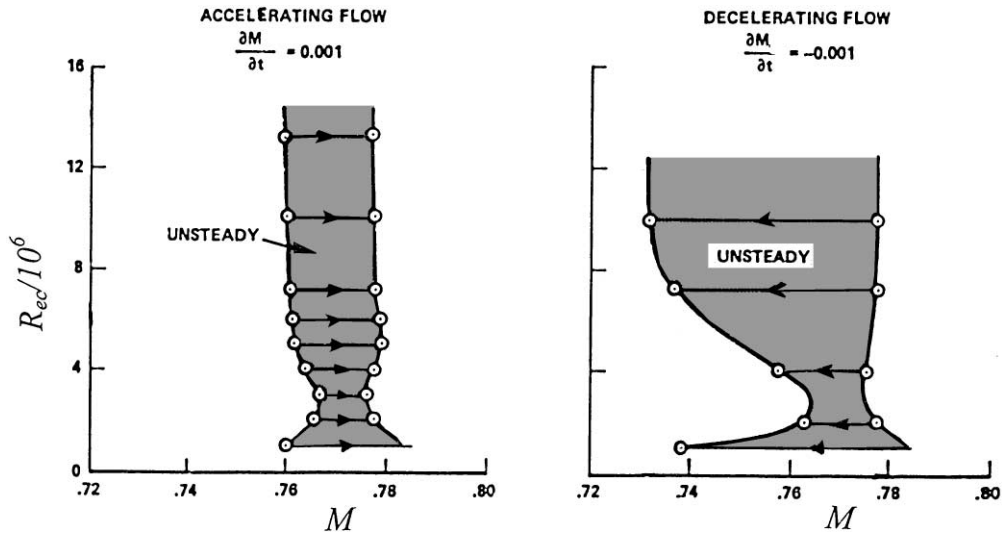


Fig. 17. Unsteady flow domains (from Ref. [50]).

the left-hand boundaries are consistently different, indicating a strong hysteresis effect. The first appearance of shock-induced separation and the onset of periodic flow occurs at peak  $M_1 \approx 1.25$ .

Close examination of the instantaneous pressure measurements and high-speed shadowgraph movies of the flowfield indicates two types of periodic flow to occur at  $\alpha = 0^\circ$ . The type C prevails during most of the domain shown in Fig. 17 with the exception being near the right-hand (high speed) boundaries where the buffeting is weak and is approaching the steady state with shock-induced separation of the boundary layer. Some limited but exploratory study of the effect of incidence was carried out up to  $\alpha = 4^\circ$  at  $Re_c = 11 \times 10^6$ . The measured reduced frequency  $k$  (based on semichord  $b$ ) is shown in Fig. 18 where the boundary for the high  $M$  is practically the same for accelerating and decelerating flows. Only the left-hand boundary changes noticeably. Except for a small region at the lower corner on the left-hand boundary at the higher incidence, and a small Mach number range at the high-speed boundary, the flow is of the type C.

Flow communication between upper and lower surfaces is necessary in order that the cyclic unsteady flow alternating between trailing edge and shock-induced separation of the boundary layer on the airfoil surfaces can occur. By putting a thin splitter plate 0.02 chord thick and length  $c/2$  downstream of the trailing edge in the plane of the airfoil, McDevitt [50] virtually eliminated the unsteady phenomenon. The only noticeable periodic pressure fluctuations were detected by the most rearward sensor ( $x/c = 0.78$ ) and the motion is of type A occurring only in a very narrow  $M$  range from 0.771 to 0.773 at  $Re_c = 8 \times 10^6$ . In studying the effect of the length of the plates on the wake flow, McDevitt [50] found that

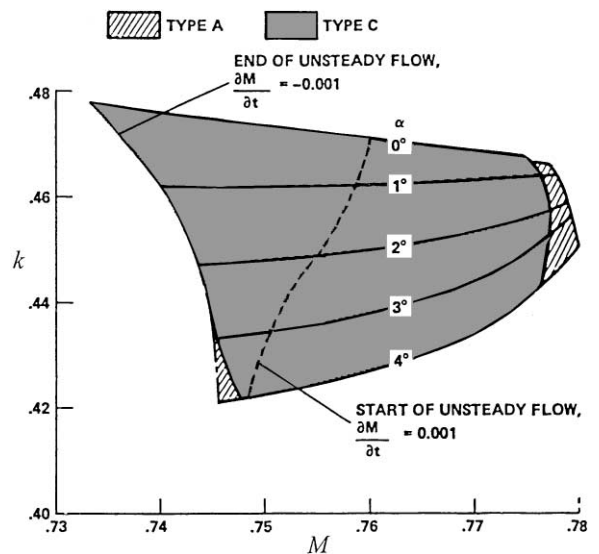


Fig. 18. Frequency of pressure fluctuations at angles of attack;  $Re_c = 11 \times 10^6$  (from Ref. [50]).

type C occurred only for very short plates. The wake closes about 1/4 chord behind the trailing edge and a splitter plate of this length or longer is very effective in suppressing communication across the wake, although a high-frequency type A shock oscillation persists at low amplitude.

Mabey [52] carried out studies on the periodic flow boundaries at zero incidence for two sets of biconvex airfoils ranging from 10% to 20% thick with chord lengths of 32 and 50 mm, respectively. The region of periodic motion with laminar boundary layer is a little

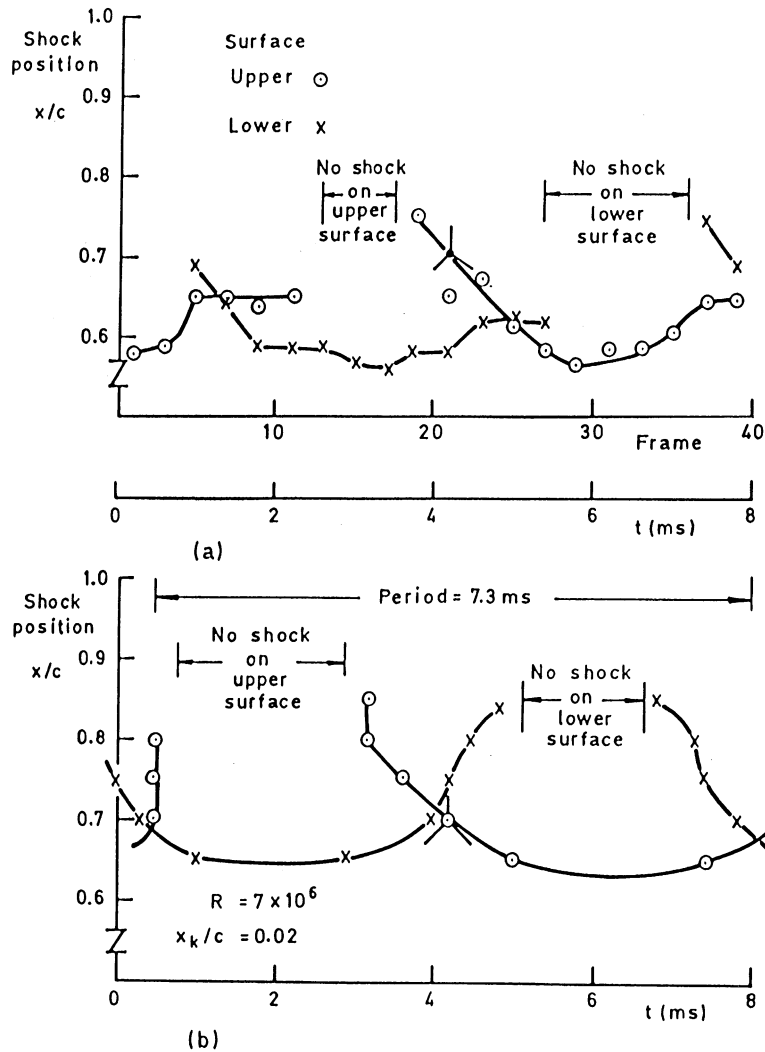


Fig. 19. Shock position with time at  $M = 0.85$ ,  $\alpha = 0^\circ$ : (a) from shadowgraph, (b) from pressure (from Ref. [7]).

wider than for turbulent shock-boundary layer interaction. Turbulent boundary layer was ensured by fixing transition at 2.5 mm downstream of the leading edge with a narrow band of small glass spheres of 0.25 mm diameter.

With free transition, the measured reduced frequency  $\kappa$  is between 0.72 and 1.04 for the short chord airfoils, while for the longer chord airfoils, it lies between 0.85 and 1.15, which is significantly higher than the short chord airfoil frequencies. Mabey [52] concluded that the origin of flow oscillation is essentially a viscous phenomenon, and a necessary but not sufficient condition for the onset of periodic flow requires the peak  $M_1$  just upstream of the shock to be in the range from about 1.14 to 1.24.

Mabey et al. [7] carried out further studies on a 14% thick biconvex half-wing model with an aspect ratio of two which is sufficiently large to give two-dimensional flow at the mid-section at  $\alpha = 0^\circ$  for shadowgraph and

pressure measurements. The tests were conducted at free stream  $M$  from 0.74 to 0.9, and  $R_{ec}$  from  $1 \times 10^6$  to  $7 \times 10^6$ . Most of the studies were carried out at  $\alpha = 0^\circ$ , but limited results were available for  $\alpha$  between  $-3^\circ$  and  $3^\circ$ . Periodic flow over a narrow  $M$  range from 0.82 to 0.86 was observed and the shock moves in antiphase. Strong shock oscillations at  $f \approx 130$  Hz giving a reduced frequency  $\kappa$  close to 1 were detected. Also, oscillation of the separated wake was clearly visible from shadowgraph movies. Scale effects are small over the range of  $R_{ec}$  from  $1 \times 10^6$  to  $7 \times 10^6$  provided that the boundary layer is turbulent just upstream of the shock. It is possible to suppress the periodic flow from  $R_{ec}$  about  $3 \times 10^6$  to  $5 \times 10^6$  if the boundary layer is laminar and scale effects are large in this case.

Fig. 19a shows from shadowgraphs taken at  $M = 0.85$  that the shock moves from  $x/c = 0.78$  to 0.55 and

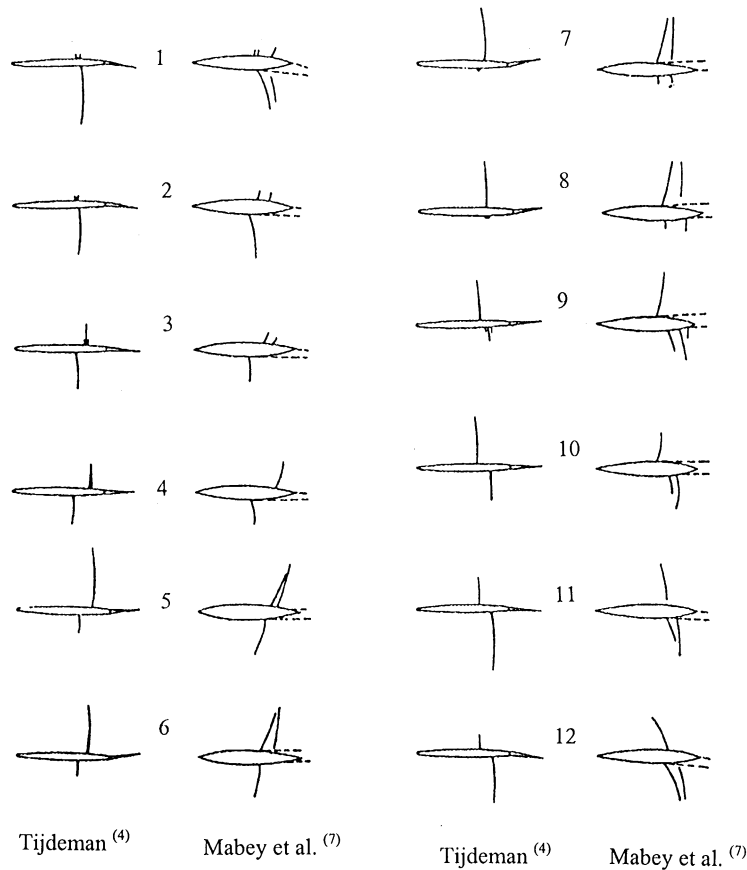


Fig. 20. Comparison of flows on airfoil with oscillating flap and a 14% biconex airfoil (from Ref. [53]).

remains practically stationary at that position for about half a period. It then gradually becomes weaker until the flow suddenly reattaches and the shock disappears. Pressure measurements shown in Fig. 19b suggest a similar picture with forward shock movement from  $x/c = 0.85$  to  $0.65$ . These results are consistent with Fig. 19a and Mabey et al. [7] suggested the motion to be of the type B. This is different from McDevitt's [50] classification based on the 18% thick circular-arc airfoil results where he deduced the motion to be type C. Finke [33] showed from spark interferograms the alternating upstream motion of the shock waves on the upper and lower surfaces of a 20% thick biconvex circular-arc airfoil. Near the leading edge the shock waves degenerate into weak pressure waves and leave the airfoil as upstream propagating sound waves. This behavior of the periodic flow phenomenon belongs to the type C motion. It is possible that Mabey et al. [7] tested a thinner airfoil and detected type B motion, and it is conceivable that the shock motion depends on the airfoil thickness. Further evidence that the 14% thick circular-arc airfoil generates type B motion was demonstrated by Mohan [53] who

compared Mabey et al. [7] shadowgraph sketches taken at  $M = 0.85$ ,  $R_{ec} = 7 \times 10^6$  and  $\alpha = 0^\circ$  with transition fixed at  $x/c = 0.02$  with Tijdeman's [4] oscillating flap results at  $M = 0.875$  for the NACA 64A006 airfoil. The flap oscillates at an amplitude of  $\delta = 1^\circ$  and a frequency of 120 Hz. The reduced frequency  $\kappa$  for the oscillating flap results is about 0.43 while that for the periodic shock motion on the 14% thick airfoil is approximately one. However, at the same phase in the periodic cycle, the shock positions bear remarkable resemblance as shown in Fig. 20. This close correlation between the two sets of results suggests that Mabey et al. [7] observations are indeed the type B motion. Also, shadowgraphs did not reveal the presence of weak compression waves on the airfoil near the leading edge and their subsequent propagation into the flow upstream of the airfoil.

Unlike McDevitt's [50] results, Mabey et al. [7] did not detect a hysteresis effect in the boundaries for periodic shock motion. The methods of increasing  $M$  were somewhat different. Mabey et al. [7] used a pressure transducer mounted at  $x/c = 0.8$  on the lower surface to monitor the flow in real time. Near the periodic

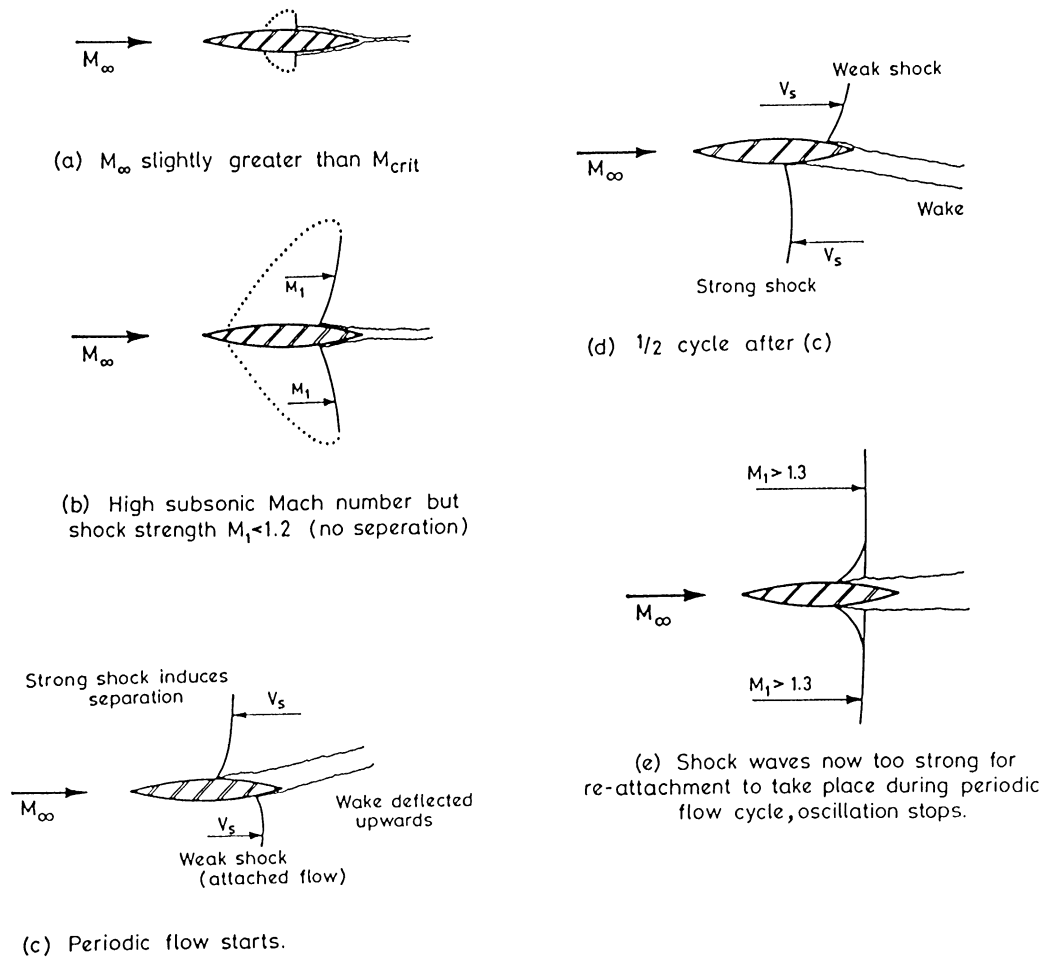


Fig. 21. Shock wave development as Mach number increases (from Ref. [54]).

boundary at  $M = 0.8$ , the Mach number was increased in steps of 0.01 above  $M = 0.8$  at constant total pressure. Using these small increments a speed would be reached at which periodic flow would occur intermittently but for which no frequency could be determined. A further increase of 0.01 would then establish a remarkably steady periodic flow with a single predominant frequency. The freestream Mach number was then increased until intermittent flow occurred and then suppressed by a further increase of 0.01. When  $M$  was reduced, no hysteresis was observed, while in McDevitt [50] tests, hysteresis was observed when the Mach number was changed continuously at a small rate  $dM/dt = \pm 0.001$ .

Previous tests [52] show that for periodic flow to exist, shock-induced separation must occur with a peak  $M_1$  just upstream of the shock within a narrow  $M_1$  range of  $1.14 < M_1 < 1.24$ . The tests were conducted on small models and restricted to small  $Re_c$  ( $\leq 0.6 \times 10^6$ ), and both laminar and turbulent boundary layer gave periodic flow at a reduced frequency  $\kappa$  of approximately one.

From later tests with free transition but with a thin turbulent boundary layer at the shock ( $Re_c > 5 \times 10^6$ ), Mabey et al. [7] found that the peak Mach number lies in the range  $1.24 < M_1 < 1.34$ . With transition fixed at  $x/c = 0.02$  giving a thicker boundary layer at the shock, this criterion becomes ( $Re_c > 4 \times 10^6$ )  $1.22 < M_1 < 1.34$ . The results show that the range of  $M_1$  is apparently largely independent of  $Re_c$ , implying that scale effects are small. With a laminar boundary layer, scale effects are large and the region of periodic motion is completely eliminated over the  $Re_c$  range from about  $3 \times 10^6$  to  $5 \times 10^6$ .

Upon interpreting available results for the 14% thick circular-arc airfoil at zero incidence, Gibb [54] presented a mechanism of the shock oscillation phenomenon. Fig. 21 shows the sequence of events for this airfoil as the freestream Mach number is increased. It is assumed that the range of peak Mach number  $M_1$  where shock-induced separation occurs is known and is given by  $M_L < M_1 < M_U$ . Gibb [54] used a value of 1.21 for the lower limit  $M_L$  and 1.3 for the upper limit  $M_U$ .

In Fig. 21a, when the freestream Mach number is slightly above the critical value for transonic flow over the airfoil, a weak shock wave appears with a small pocket of supersonic flow in front of the shock. The flow is attached, steady and symmetrical. As  $M$  is increased, the shock wave becomes stronger and moves aft towards the trailing edge. The pocket of supersonic flow increases and the flow is attached as long as  $M_1$  is below the value required to promote separation. An upstream pressure disturbance on the upper surface will move the shock forward at a speed  $V_s$ . The instantaneous shock Mach number is given by

$$M_s = M_1 + \frac{1}{a} dx_s/dt, \quad (1)$$

where the subscript  $s$  denotes the shock wave. If  $M_1$  is close to  $M_L$ , and if  $V_s$  is sufficiently large so that  $M_s > M_L$ , the flow will separate as the shock travels forward. Separation on the upper surface will cause a deflection of the wake upward, similar to the movement of a flap as illustrated in Fig. 20. The asymmetric wake will accelerate the flow on the lower surface and the shock wave will move towards the trailing edge.  $V_s$  will contribute to a decrease in  $M_s$  but as long as  $M_s < M_L$ , the boundary layer will remain attached (see Fig. 21c). Since the upper surface shock is moving into a slower supersonic region, its strength will weaken as it propagates upstream. The flow becomes attached when a position is reached where  $M_s < M_L$ . On the other hand, the lower surface shock will eventually strengthen to cause boundary layer separation when  $M_s > M_L$ . The wake will gradually deflect downward reversing the direction of shock motion. There will be a time lag between the wake deflection and the shock movement, but the flow can maintain a self-sustained periodic motion. As  $M$  is further increased, a value will be reached such that re-attachment can no longer take place when  $M_s > M_U$ . The shock will be strong enough at all times to cause shock-induced separation and periodic motion then ceases.

There is sufficient evidence [33] from optical studies that the wake oscillates in a synchronous manner with the shock oscillations and behaves like a flap. Furthermore, Mohan [53] showed that by shortening the rear portion of a 14% thick circular-arc airfoil, the frequency of shock oscillation increases, thus demonstrating the dependence of the distance between the shock and the trailing edge on the periodic motion. Tijdeman [4] has pointed out that the flap can be treated as an acoustic source placed at the hinge line, and the time required for a disturbance to travel from the trailing edge to the shock is given by the following expression:

$$\Delta t = - \int_{x=c}^{x_s} \frac{dx}{(1 - M_{loc})a_{loc}}, \quad (2)$$

where  $M_{loc}$  and  $a_{loc}$  are the local Mach number and speed of sound, respectively.  $M_{loc}$  is approximated by the following empirical formula:

$$M_{loc} = R[M_{loc}(\text{at the surface}) - M] + M. \quad (3)$$

The relaxation factor  $R$  varies between 0 and 1, and for the NLR 7301 airfoil the experimentally determined value is 0.7.

Mabey et al. [7] related the frequency with  $\Delta t$  from Eq. (2) and found that at  $M = 0.81$  and  $0.88$  the reduced frequency  $\kappa$  was 3.6 and 2.3, respectively. This is considerably higher than the experimental value of about 1.

Another empirical formula to determine the time for disturbances at the trailing edge to reach the shock is given by Erickson and Stephenson [55] as follows:

$$f = \frac{a(1 - M)}{4(c - x_s)}. \quad (4)$$

Expressing Eq. (4) as a reduced frequency using  $(c - x_s)$  as the characteristic length, Mabey [52] computed the quantity  $\omega(c - x_s)/U$ . The experimental values were found to be about 70% of those from prediction. The reduced frequency  $2\pi f c/U$  using Eq. (4) is approximately 1.43 as compared to about 1 from experiments. This value is lower than that obtained from Tijdeman's [4] equation, but it is still too large. It is obvious that the self-sustained oscillation mechanism is incomplete when only wave propagation from the trailing edge to the shock wave is considered.

#### 4.3. Supercritical airfoils

In experiments carried out on the NLR 0.1025-0.6750-1.300 airfoil at  $M = 0.71$  and  $\alpha = 5^\circ$ , Finke [33] detected the presence of pressure oscillations on the lower airfoil surface. Multi-spark shadowgraphs also showed disturbances to travel upstream on the lower surface. A possible cause for the occurrence of shock oscillations at high incidence is the unsteady flowfield generated by these upstream propagating disturbances which are triggered by the divergence of the trailing edge pressure. The resulting periodic oscillations of the circulation of the airfoil cause oscillations of the circulation in the wake. Stanewsky and Basler [12] extended this idea in their study of buffeting on the CAST7/D0A1 supercritical airfoil and suggested that since the flow on the lower surface is accelerated due to the pressure drop at the trailing edge, the stagnation point will change. A change in the flow on the upper surface will develop and hence alters the circulation. However, they did not present results from the high-speed interferograms which were capable of giving the various paths of the propagation of the disturbances.

Stanewsky and Basler [12] reported some results that are typical of those for supercritical airfoils. They found

the reduced frequencies  $\kappa$  to depend on the Mach number, incidence angle and Reynolds number, and these values vary from about 0.3 to 0.6. Similar magnitudes of the shock oscillation frequencies are reported by Roos [8], Lee [10] and Hirose and Miwa [9], but they are lower than those obtained by Mabey et al. [7] for the circular-arc airfoil. With transition fixed at 9% chord from the leading edge, Stanewsky and Basler [12] detected a decrease in reduced frequency  $\kappa$  with  $Re_{cc}$  between  $6 \times 10^6$  and  $10 \times 10^6$ , while a much smaller variation was observed by Hirose and Miwa [9] for the Garabedian-Korn GK 75-06-12 (similar to the BGK No. 1 airfoil) at  $15 \times 10^6 < Re_{cc} < 30 \times 10^6$ . The increase in reduced frequency with Mach number was also observed by Lee [10] for the BGK No. 1 airfoil. However, for the modified Whitcomb airfoil, a decrease with Mach number was reported by Roos [8]. This could be a scale effect since Roos [8] results were obtained at a lower  $Re_{cc} = 2 \times 10^6$  with transition fixed at 35% chord. It may be of interest to note that in the studies [8–10,12,32] on supercritical airfoils, the shock motions reported are mainly of the type A and there was no specific mention on the existence of the other two types.

The mechanism of shock oscillation described by Gibb [54] agrees with observations by Stanewsky and Basler [12] on the fluctuations of the boundary layer thickness at the trailing edge. In the case of the CAST7/D0A1 at incidence, a shock wave is present only on the upper surface. Results given at  $M = 0.77$ ,  $\alpha = 3^\circ$ ,  $Re_{cc} = 6 \times 10^6$  with transition fixed at 9% chord show that the shock motion belongs to type A. The boundary layer thickness at the trailing edge reaches a maximum when the shock is furthest upstream, and the opposite is true when the shock is at the furthest distance downstream. There is a small phase lag between the shock motion and the growth of the boundary layer. Stanewsky and Basler [12] interpreted the results to suggest the thickening of the boundary layer at the trailing edge and the corresponding drop in trailing edge pressure as the driving mechanism for the periodic shock motion. Fig. 22 shows the variation in shock strength represented by the height of the shock wave  $h_{ss}$  in a cycle of shock oscillation. During the downstream shock movement, the strength decreases due to a smaller value of  $M_s$  for a rearward moving shock (see Eq. (1)). At  $x/c \approx 0.48$  the shock strength starts to increase, and this is probably related to a strengthening of the shock as suggested by Gibb [54] with separation occurring when  $M_s > M_L$ . The shock strength continues to increase until the downstream motion reaches its maximum distance from the leading edge and then begins its forward motion. The shock strength increases as a result of a higher  $M_s$  due to propagation against the flow, and begins to decrease for the remainder of the upstream movement when  $x/c$  reaches about 0.44. The reason for the decrease is the change over from shock-induced separation to attached flow at the shock when  $M_s < M_L$ .

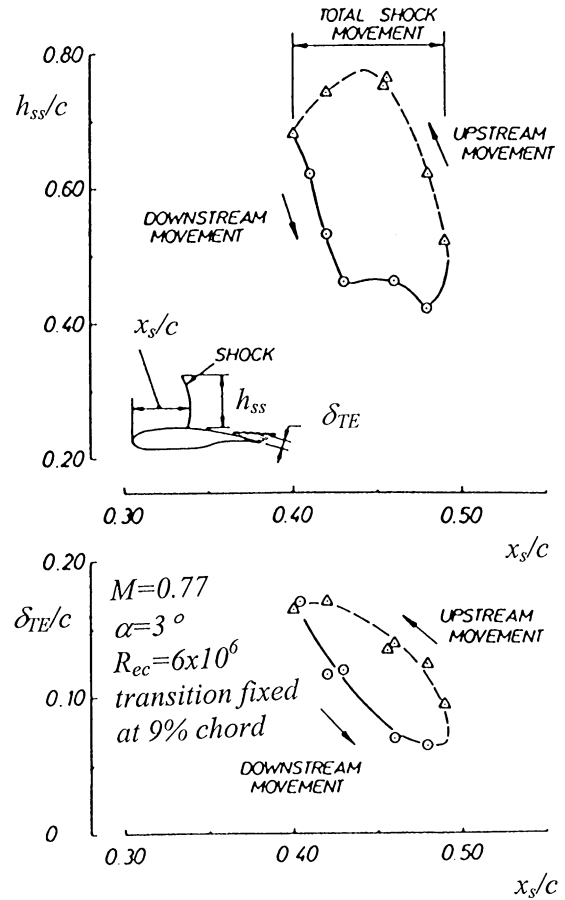


Fig. 22. Relation between shock movement, shock strength and trailing edge boundary layer thickness (from Ref. [12]).

The bottom figure shows during upstream and downstream shock motion, the boundary layer thickness at the trailing edge increases and decreases without showing the effects of a change in the type of shock-boundary layer interaction at  $x/c = 0.44$  and  $x/c = 0.48$ . Stanewsky and Basler [12] attributed this to the delay required for disturbances to propagate from the shock to the trailing edge. During the upstream shock movement, the termination of shock-induced separation at  $x/c = 0.44$  will not be felt at the trailing edge instantaneously and the boundary layer continues to grow. By the time the effect of the reduced shock strength is felt at the trailing edge, the shock has already started to move downstream. Similarly, the increase in shock strength during the downstream motion when the shock reaches  $x/c = 0.48$  will not be felt at the trailing edge until the shock begins its upstream motion at  $x/c = 0.49$ .

The coupling between the shock and the wake forms a crucial link responsible for the self-sustained oscillation observed on airfoils during transonic buffeting. In

analyzing the broadband surface pressure correlation, Roos [32] and Lee [10] found that upstream propagation of disturbances is possible in the boundary layer on the airfoil upper surface for attached flow. For fully separated flow, they detected only pressure waves traveling downstream from the shock to the trailing edge. Hence, during transonic buffeting, changes in the wake do not communicate to the upstream shock via the upper surface boundary layer, and the most likely path is in the region outside the separated flow.

Experiments carried out by Lee [10] on the BGK No. 1 airfoil at  $Re_c = 20 \times 10^6$  with free transition showed the disturbance propagation speed along the upper surface boundary layer is a function of the Mach number and angle of incidence. Scale effects were not investigated. The studies by Roos [32] on a Whitcomb-type airfoil was also carried out at a single Reynolds number  $Re_c = 2 \times 10^6$ . Lee's [10] results showed that for  $0.6 < M < 0.8$  and  $5 < \alpha < 12^\circ$ , the non-dimensional broadband convection velocity  $U_c/U$  lies between 0.5 to 0.8. For large values of  $\alpha$ , the curves for all  $M$  reach a constant value approximately 0.5–0.55. Roos [32] carried out narrowband correlation of the pressure field at heavy buffeting and demonstrated the dependence of convection velocity on frequency. Small-scale disturbances associated with high frequencies travel close to the edge of the shear layer at a velocity higher than the large-scale disturbances close to the surface. The convection velocity  $U_c/U$  varies from a value slightly above 0.8 at reduced frequency  $\kappa = 60$  to about 0.2 at  $\kappa = 1$ . Using the experimental value [8] of the shock oscillation frequency  $\kappa = 0.39$  at  $M = 0.82$ ,  $U_c/U$  is found to be approximately 0.18, thus indicating that disturbances from the shock to the trailing edge propagate close to the airfoil surface.

The unsteady pressure fluctuations behind the periodic shock wave have contributions from two sources; namely, a random component associated with the turbulent motion in the separated flow region and a deterministic part  $\tilde{C}_p$  as a result of shock wave oscillation. The magnitude of  $\tilde{C}_p$  is usually small compared to that from turbulent fluctuations. In determining the oscillatory pressure wave component, Lee et al. [45] first obtained the periodic shock frequency from the balance normal force spectrum. The balance output was then passed through a band pass filter and used as a reference signal in carrying out an ensemble averaging of the transducer outputs. Fig. 23 shows a typical example of the variation of the total pressure fluctuation  $C'_p$  on the airfoil surface at  $M = 0.746$  and  $\alpha = 6.066^\circ$ . Large fluctuations are seen near the shock-boundary layer interaction region, but they decay rapidly and show a slight increase towards the trailing edge after reaching a minimum at  $x/c \approx 0.5$ . The ensemble-averaged component  $\tilde{C}_p$  usually has a smaller magnitude compared to the total fluctuations and the rms values of the fundamental frequency component are

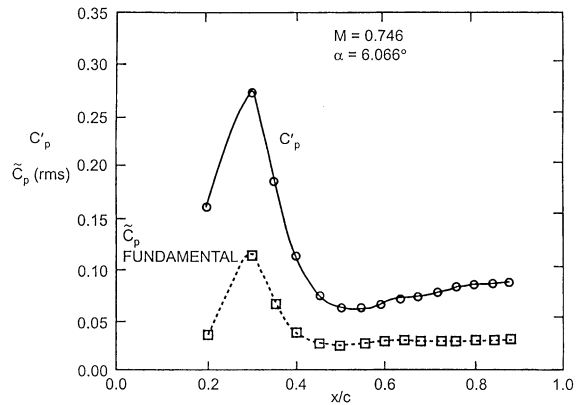


Fig. 23. rms values of pressure fluctuations (from Ref. [56]).

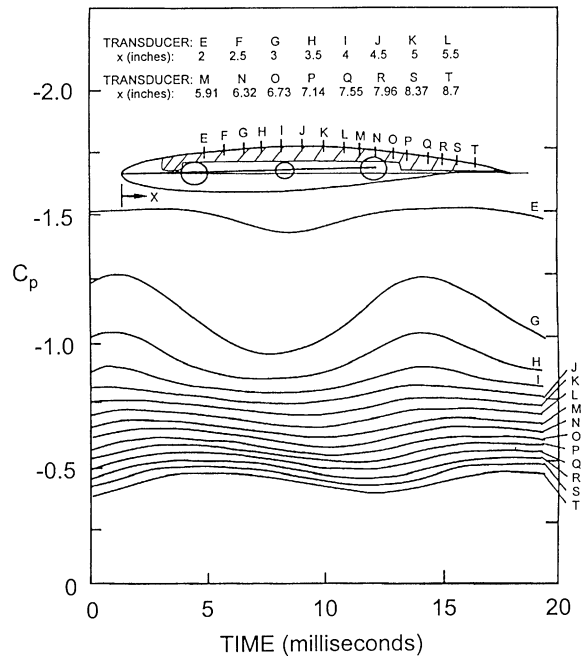


Fig. 24. Instantaneous  $C_p$  variations (from Ref. [56]).

shown in Fig. 23. The largest differences between these two quantities occur in the region traversed by the shock wave. Between  $x/c = 0.5$  to  $0.87$  the value of  $\tilde{C}_p$  (rms) is nearly constant. Fig. 24 shows for the same test conditions the instantaneous variations of the ensemble-averaged  $C_p$  with time. Here  $C_p$  is the sum of the steady-state pressure coefficient and the value of the fundamental component of  $\tilde{C}_p$ . Large amplitude oscillations in the neighborhood of the mean shock position are found for the transducer located at  $x/c = 0.3$ .

The ensemble-averaged  $\tilde{C}_p$  distributions with  $x/c$  at different phase angles during a shock oscillation cycle are

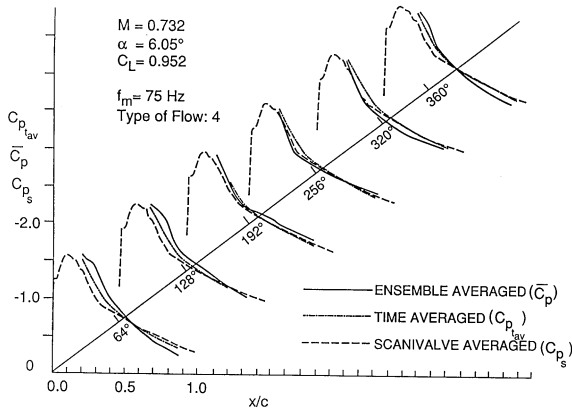


Fig. 25. Ensemble-, time- averaged and scanivalve  $C_p$  plots (from Ref. [27]).

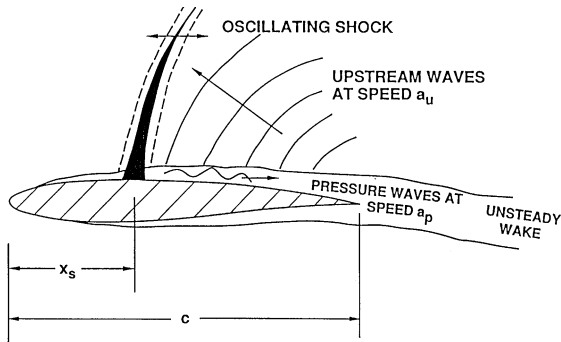


Fig. 26. Model of self-sustained shock oscillation (from Ref. [56]).

shown in Fig. 25 at  $M = 0.732$  and  $\alpha = 6.05^\circ$ . Superimposed on these results are the time-averaged  $C_{p_{tav}}$  values obtained from the fast response transducers using a signal duration of 2 s. Also shown in the figure are the pressure distributions  $C_{ps}$  obtained from scanivalve measurements which are not as accurate as the  $C_{p_{tav}}$  results because of the short averaging time. The amplitude of the shock oscillations from the ensemble-averaged  $\bar{C}_p$  data is quite large having a value of nearly  $0.05c$ , and the shock motion belongs to the type A.

Lee [56] proposed a possible mechanism of self-sustained shock oscillation during transonic buffeting with fully separated flow. In Fig. 26 the shock wave is shown to oscillate on the upper surface of the airfoil about a mean position (corresponding to type A motion). Due to the movement of the shock, pressure waves are formed which propagate downstream in the separated flow region at a velocity  $a_p$ . On reaching the trailing edge, the disturbances generate upstream moving waves at velocity  $a_u$ , either from the wake fluctuation or from the

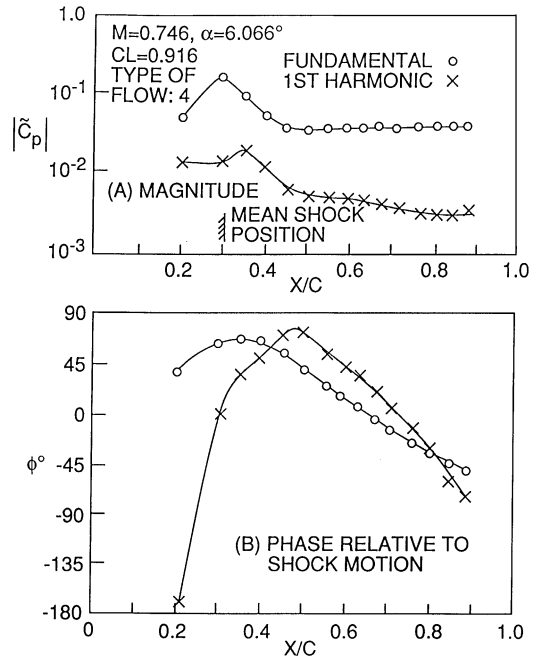


Fig. 27. Magnitude and phase of pressure waves propagating downstream in separated flow region (from Ref. [27]).

trailing edge boundary layer. These waves will interact with the shock wave and impart energy to maintain its oscillation. The loop is then complete and the measured period of the shock wave oscillation should agree with the time it takes for a disturbance to propagate from the shock to the trailing edge plus the duration for an upstream moving wave to reach the shock from the trailing edge via the region outside the separated flow.

The magnitude and phase (relative to the shock oscillation) of the fundamental and first harmonic of  $\bar{C}_p$  for  $M = 0.746$  and  $\alpha = 6.066^\circ$  are shown in Fig. 27. The magnitude  $|\bar{C}_p|$  peaks close to the mean shock position and is much smaller for the first harmonic. The phase angle  $\phi$  varied almost linearly behind the shock. For other test conditions, the slope  $d\phi/dx$  may not be approximately constant on the airfoil as in this case. From the phase relation the velocity  $a_p$  of the pressure wave in the separated flow region can be calculated. The total time it takes for a disturbance originating from the shock to complete a loop is given by the following relation:

$$T_p = \int_{x_s}^c 1/a_p dx - \int_c^{x_s} 1/a_u dx. \tag{5}$$

The value of  $a_u$  is equal to  $(1 - M_{loc})a_{loc}$ , and  $M_{loc}$  is given by Eq. (3). Knowing  $a_p$  and  $a_u$  as functions of  $x$ , and upon determining  $x_s$  from steady pressure measurements on the airfoil, Eq. (5) can be integrated and the frequency of the feed back loop  $f_c = 1/T_p$  is then determined. Small

Table 1  
Comparison of measured and calculated shock oscillation frequencies (from Ref. [56])

$M$	$\alpha$ (deg)	$M_1$	$\kappa = 2\pi f_m c/U$	$f_m$ (Hz) from balance	$f_c$ (Hz) calculated
0.688	6.97	1.52	0.507	70	91.3
0.722	6.00	1.47	0.519	75	82.6
0.722	7.02	1.5	0.554	80	75.2
0.732	6.03	1.46	0.513	75	87.8
0.747	4.52	1.42	0.504	75	87.7
0.747	6.04	1.46	0.537	80	85.4
0.747	8.02	1.5	0.505	75	74.1

variations in Tijdeman's empirical value [4] of  $R = 0.7$  do not introduce significant changes in the second integral of Eq. (5). Results for different  $M$  and  $\alpha$  are given in Table 1. The correlation between measured shock frequency  $f_m$  from the balance force spectra and the calculated frequency  $f_c$  is fair considering the inaccuracies in locating the shock positions and the uncertainty of the upstream propagating velocity. It is interesting to note that the narrowband convection velocity obtained by Roos [8] for the modified Whitcomb airfoil is of the same order of magnitude as the velocity  $a_p$  for the BGK No. 1 airfoil. Shown also in the table are the Mach numbers  $M_1$  in front of the shock. These values are above the upper limit of 1.34 given by Mabey et al. [7] for the biconvex circular-arc airfoil. The reduced frequency  $\kappa$  is based on the measured frequency and the value is about half that obtained by Mabey et al. [7].

## 5. Wave propagation in the airfoil flowfield

### 5.1. Behavior of disturbances in two-dimensional nonuniform flows

Experimental studies have shown quite conclusively that during buffeting the wake oscillates and the periodic shock motion is coupled with disturbances generated at the trailing edge. Tijdeman [4] called these "Kutta" waves since they are associated with the Kutta condition at the trailing edge. Some early investigations of wave propagation in transonic flows have been carried out by Spee [57] in connection with the stability of smooth transonic flow past airfoils. Using a graphical method based on procedures commonly used in geometrical acoustics, Spee [57] demonstrated in transonic flows the waves generated downstream in the boundary layer or in the wake can penetrate into the supersonic region in front of the shock if the mean flow velocity gradients are sufficiently large. In the self-sustained shock oscillation model proposed by Lee [56], the upstream moving waves

in the flowfield outside the separated flow region are assumed to carry the bulk of the energy to the shock in order to maintain its oscillatory motion, and an inviscid flow model in the formulation of wave propagation in a nonuniform medium is assumed. The use of Tijdeman's empirical equation [4] has raised some questions as to the universality of the constant  $R$  (see Eq. (3)) for different airfoils and Mach numbers. To assess the accuracy on the use of Tijdeman's formula for the Kutta waves, Lee et al. [58,59] studied wave propagation in transonic flows for different airfoil thicknesses and Mach numbers, and computed the time for disturbances to travel from the trailing edge to the shock.

#### 5.1.1. Characteristic surfaces

Lee et al. [58,59] used the method of characteristics to investigate the propagation of pressure disturbances in transonic flows. The nonconservative form of the nonlinear transonic small disturbance equation written in terms of a potential  $\phi$  is given by

$$A\phi_{tt} + 2B\phi_{xt} = C\phi_{xx} + \phi_{yy}, \quad (6)$$

where  $A = M^2\kappa^2$ ,  $B = M^2\kappa$ ,  $C = (1 - M^2) - (\gamma + 1)M^2\phi_x$ , and the subscripts  $x$ ,  $y$ ,  $t$  denote differentiation with respect to those variables, respectively. To find a characteristic surface for Eq. (6), the potential  $\phi$  and its gradient  $\nabla\phi$  are assumed to be continuous, but the second derivatives of  $\phi$  have jump discontinuities across a surface  $H(x, y, t) = \text{const}$ . Thus, on the surface of a discontinuity, the function satisfies the equation

$$H_t^2 + 2A^{-1}BH_xH_t - A^{-1}CH_x^2 - A^{-1}H_y^2 = 0. \quad (7)$$

This equation is referred to as the characteristic equation of Eq. (6), and its solution defines a surface  $H = \text{const}$  which can also be described by the following equation:

$$H(t, x, y) \equiv t - S(x, y) = 0 \quad \text{or} \quad t = S(x, y). \quad (8)$$

Substituting Eq. (8) into Eq. (7) gives an expression for  $S(x, y)$  as follows:

$$1 - 2A^{-1}BS_x - A^{-1}CS_x^2 - A^{-1}S_y^2 = 0. \quad (9)$$

Introducing the variables  $p = S_x$  and  $q = S_y$ , and adding and subtracting a term  $(A^{-1}B)^2p^2$ , Eq. (9) becomes

$$\begin{aligned} F(x, y, S, p, q) \\ \equiv -1 + A^{-1}Bp + A^{-1}\sqrt{(B^2 + AC)p^2 + Aq^2} = 0. \end{aligned} \quad (10)$$

On the characteristic surface,  $t = S$ ,  $\phi = \phi(S, x, y)$ , and therefore  $C$  is a function of  $x, y$  and  $S$ . Eq. (10) is often called the Eikonal equation [60], and a solution for  $S$  can be obtained parametrically by a system of ordinary

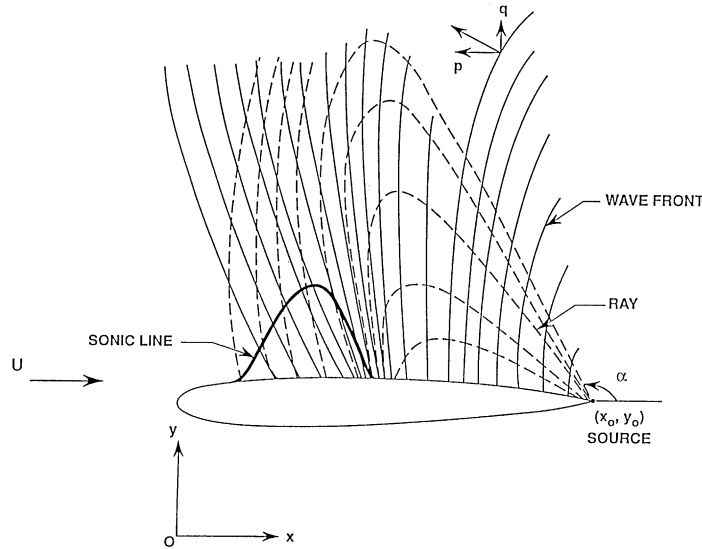


Fig. 28. Schematic of wavefronts and rays emanating from source disturbance at trailing edge of airfoil (from Ref. [59]).

differential equations [61] as follows:

$$\begin{aligned} \frac{dx}{dt} &= A^{-1}B + \frac{(B^2 + AC)p}{A\sqrt{(B^2 + AC)p^2 + Aq^2}}, \\ \frac{dy}{dt} &= \frac{q}{\sqrt{(B^2 + AC)p^2 + Aq^2}}, \\ \frac{dp}{dt} &= \frac{-C_x p^2 - C_t p^3}{2\sqrt{(B^2 + AC)p^2 + Aq^2}}, \\ \frac{dq}{dt} &= \frac{-C_y p^2 - C_t p^2 q}{2\sqrt{(B^2 + AC)p^2 + Aq^2}}, \end{aligned} \quad (11)$$

where

$$\begin{aligned} C_x &= -(\gamma + 1)M^2\phi_{xx}, C_y = -(\gamma + 1)M^2\phi_{xy} \quad \text{and} \\ C_t &= -(\gamma + 1)M^2\phi_{xt}. \end{aligned} \quad (12)$$

This system of equations describes how disturbances in the form of discontinuities propagate in the transonic flowfield. Fig. 28 shows a schematic of the wave fronts generated above the upper surface of an airfoil from a source placed at the trailing edge. The expression  $S(x, y) = t$  describes a wave front at a given time  $t$ . Thus  $(p, q) = (S_x, S_y)$  is parallel to the normal to the wave fronts, and the vector  $(dx/dt, dy/dt)$  is the direction of the rays which are integral curves  $[x(t), y(t)]$  of Eq. (11) that define the paths followed by disturbances. Lee et al. [59] considered the disturbance to be an impulse at a point  $(x_0, y_0)$  at time  $t = t_0$  and the initial wave front is represented by a circle of infinitesimal radius. Each point on

the initial wave front has the same position  $(x_0, y_0)$ , but the normal direction is given by

$$(p_0, q_0) = [r \cos \alpha, r \sin \alpha], \quad 0 \leq \alpha \leq 2\pi. \quad (13)$$

The radius  $r$  is determined by requiring the initial wave front to be on a characteristic surface. Substituting Eq. (13) into Eq. (10),  $r$  can be obtained in terms of  $\alpha$ , as well as  $x_0, y_0$ . For a given  $\alpha \in (0, 2\pi)$ , Eq. (11) can be integrated in time to yield the solution

$$x = x(t, \alpha), y = y(t, \alpha), p = p(t, \alpha), q = q(t, \alpha). \quad (14)$$

For a fixed angle  $\alpha$ ,  $[x(t, \alpha), y(t, \alpha)]$  for  $t > t_0$  is the ray of propagation of the energy. For a fixed time  $t > t_0$ ,  $[x(t, \alpha), y(t, \alpha)]$  for  $0 < \alpha < 2\pi$  describes the wave front of the pulse disturbance at time  $t$ .

### 5.1.2. Asymptotic expansion

There is no restriction on the transonic flowfield in which the disturbances from an arbitrary source will propagate. In the original analysis given by Lee et al. [58,59], an unsteady flowfield generated by an oscillating flap or from the motion of the airfoil itself was considered. In this review on periodic shock motion in airfoil buffeting, we consider the transonic flowfield to be steady which can be computed from a number of available computer codes. The total flow potential  $\Phi$  is represented by the sum of two terms, that is,

$$\Phi = \phi + \psi, \quad (15)$$

where  $\phi$  is the steady potential and  $\psi$  is due to the disturbance source. An equation for  $\psi$  can be obtained by

substituting Eq. (15) into Eq. (6) to give the following:

$$A\psi_{tt} + 2B\psi_{xt} = C\psi_{xx} + \psi_{yy} + D(\psi_x\psi_{xx} + \phi_{xx}\psi_x), \quad (16)$$

where  $D = -(\gamma + 1)M^2$ . Assuming the amplitude of the disturbance to be small,  $\psi$  can be written as

$$\psi = e^{i\theta} \sum_{n=1} \varepsilon^n a_n(t, x, y), \quad (17)$$

where  $\theta = \theta(t, x, y)$ , and  $a_n(t, x, y)$  are slowly varying functions, and  $\varepsilon$  is a small parameter. Furthermore, the term  $\phi_x$  is also assumed to be slowly varying. More precisely,  $\theta_t, \theta_x, \theta_y, \phi_x = 0(1)$ , and  $a_{nt}, a_{nx}, a_{ny}, \phi_{xx} = 0(\varepsilon)$ . Each additional derivative increases the order by  $\varepsilon$ . Following Whitham [60], the following substitutions are made:

$$\begin{aligned} \theta(t, x, y) &= \varepsilon^{-1} \tilde{\theta}(\varepsilon t, \varepsilon x, \varepsilon y), \\ a_n(t, x, y) &= \tilde{a}_n(\varepsilon t, \varepsilon x, \varepsilon y), \\ \phi_x(t, x, y) &= \tilde{\phi}_x(\varepsilon t, \varepsilon x, \varepsilon y), \end{aligned} \quad (18)$$

where  $\tilde{\theta}, \tilde{a}_n, \tilde{\phi}_x$ , and their derivatives are  $0(1)$ . Defining the frequency and wave numbers by

$$\omega = \theta_t, \quad \xi = -\theta_x, \quad \eta = -\theta_y, \quad (19)$$

and substituting Eqs. (17) and (18) into Eq. (16), we obtain the following equation from the  $\varepsilon$  order equation:

$$A\omega^2 - 2B\omega\xi - C\xi^2 - \eta^2 = 0. \quad (20)$$

After dropping the tilde notation, the  $\varepsilon^2$  order equation yields a relation for  $a_1$ , which leads to the following equation after averaging over one period of  $\theta$ :

$$\frac{\partial}{\partial t} [(A\omega - B\xi)a_1^2] + \frac{\partial}{\partial x} [(B\omega + C\xi)a_1^2] + \frac{\partial}{\partial y} (\eta a_1^2) = 0. \quad (21)$$

Since  $\omega = \theta_t$ ,  $\xi = -\theta_x$ , and  $\eta = -\theta_y$ , the following equations of consistency are obtained:

$$\frac{\partial \omega}{\partial x} + \frac{\partial \xi}{\partial t} = 0, \quad \frac{\partial \omega}{\partial y} + \frac{\partial \eta}{\partial t} = 0, \quad \frac{\partial \xi}{\partial y} - \frac{\partial \eta}{\partial x} = 0. \quad (22)$$

Eqs. (20)–(22) describe the refraction of frequency and wave numbers and the propagation of wave energy. Solving for  $\omega$  in Eq. (20), we obtain

$$\begin{aligned} \omega &= \Omega(x, y, t, \xi, \eta) \\ &\equiv A^{-1}B\xi + A^{-1}\sqrt{(B^2 + AC)\xi^2 + A\eta^2}. \end{aligned} \quad (23)$$

Eqs. (22) and (23) lead to a system of equations for  $(x, y, \xi, \eta)$  which is equivalent to Eq. (11) if the following substitutions are made:

$$p = \xi/\omega, \quad q = \eta/\omega. \quad (24)$$

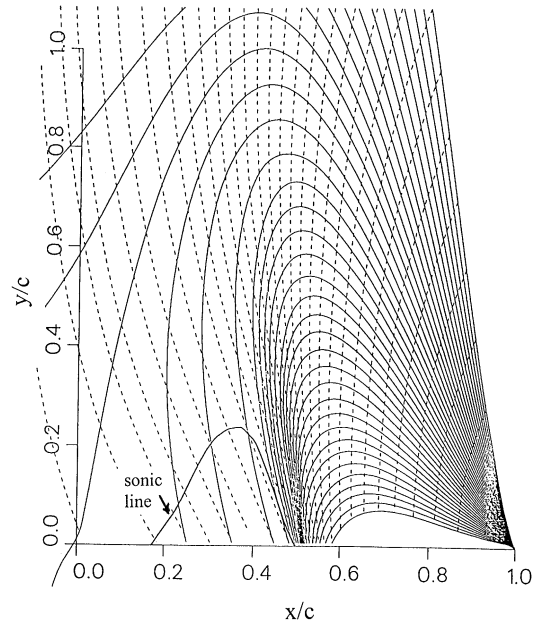


Fig. 29. Wavefronts and rays on the upper surface of a NACA 64A006 airfoil at  $M = 0.85$  generated by an impulse source at the trailing edge: ..... wavefront; — ray (from Ref. [59]).

Therefore, Eqs. (11) not only describe the propagation of the characteristic surfaces, but also the propagation of the wave solution of Eq. (17).

The first two equations in Eqs. (11) define rays or bicharacteristic curves. Along the rays, the wave numbers propagate according to the third and fourth equations of Eqs. (11). For a homogeneous medium, the right-hand sides in the third and fourth equations of Eqs. (11) are zero, so that the wave numbers are constant along a ray. Waves of the same wavelengths can be found along a ray. In the general case, however, the wave numbers are not constant, and there are refractions of wave numbers along the rays.

### 5.1.3. Propagation of wave fronts

Lee et al. [59] integrated Eqs. (11) using a first-order Euler time-stepping scheme. At each time step, the solution  $(x, y)$  from the first two equations of Eqs. (11) trace out the rays. Using a range of initial angles  $\alpha$  from  $\pi/2$  to  $\pi$ , we can compute wave fronts  $(x, y)$  on the airfoil upper surface.

Fig. 29 shows the wave fronts and rays generated by an impulse disturbance at the trailing edge of a NACA 64A006 airfoil at  $M = 0.85$  and at zero incidence angle. The range of initial ray angles  $\alpha \in (107^\circ, 170^\circ)$ , and the time interval  $\Delta t$  is approximately  $0.4^\circ$ , where time is scaled by  $\omega^{-1}$ . The nonuniformity of the flowfield causes the curvature of the rays to bend towards the surface

where the velocity gradient is the largest. At this Mach number, the steady shock wave is formed at approximately midchord, and the Mach number upstream of the shock is 1.07. Close to the surface, we can see that the wave fronts build up behind the shock wave and cannot propagate upstream. Further away from the airfoil surface, the rays penetrate into the supersonic region and move upstream past the leading edge into the freestream flowfield.

By increasing the freestream Mach number, Lee et al. [58] showed the presence of larger and stronger supersonic regions can significantly increase the curvature of the rays. It is evident from Fig. 29 that some of the rays do not reach the shock wave. For different airfoil geometry and Mach numbers, the maximum initial ray angle of a disturbance generated at the trailing edge that will reach the shock was determined by Lee et al. [58] for the NACA 64A006, NACA 64A10 and NACA 0012 airfoils. This critical angle  $\alpha_{cr}$  is smaller for the thicker airfoils, and also decreases with increasing Mach number up to a value  $M = 0.85$ , above which it remains practically unchanged.

Once the critical angle is computed, the minimum propagation time  $T_p$  from the disturbance source to the shock wave along the critical ray can be computed. For the three airfoils investigated, increasing  $M$  will result in a decrease in  $T_p$  since the shock waves are stronger and are located further downstream towards the trailing edge. Increasing airfoil thickness at constant  $M$  also has the similar effect of moving the shock closer to the disturbance source, and hence results in a smaller value of  $T_p$ .

Tijdeman's expression [4] for the propagation time given by Eq. (3) was evaluated by Lee et al. [58]. The integration was carried out along a line starting at the trailing edge at a fixed angle of  $\alpha_1 = 160^\circ$  which is determined from the best agreement with Tijdeman's empirical formula [4] given by Eq. (3). The variation of  $\alpha_1$  for the three different NACA airfoils at various incidence angles was investigated. The sensitivity of the constant  $R$  in Tijdeman's formula was evaluated for a NACA 64A006 airfoil at  $M = 0.85$ . Three values of  $R = 0.5, 0.7$  and  $0.9$  were used and the results are shown in Fig. 30 where the time  $T$  is normalized with respect to  $a/U$ . Between the shock and the disturbance source, the propagation time is not very sensitive to  $R$ , and the value of  $0.7$  gives a good approximation for the airfoils investigated.

#### 5.1.4. Wave amplitude

The wave amplitude can be computed by solving Eq. (21) where the quantity  $a_1$  is the amplitude of the leading term in the series expansion of  $\psi$ . Using Eqs. (20) and (22), Eq. (21) becomes

$$\frac{\partial a_1^2}{\partial t} + \frac{\partial}{\partial x}(\Omega_\xi a_1^2) + \frac{\partial}{\partial y}(\Omega_\eta a_1^2) = 0, \quad (25)$$

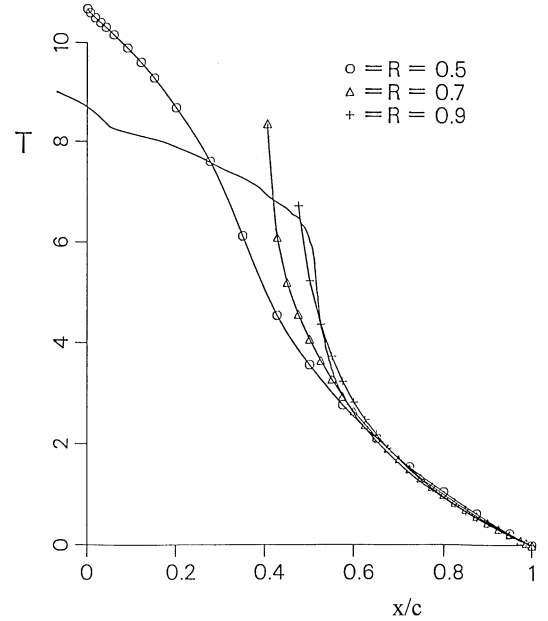


Fig. 30. Propagation time of wavefronts along  $\alpha_1 = 160^\circ$  at various values of  $R$  for a NACA 64A006 airfoil at  $M = 0.85$ : —, numerical (from Ref. [59]).

where  $(\Omega_\xi, \Omega_\eta)$  is the group velocity whose components are given by the following:

$$\Omega_\xi = A^{-1}B + \frac{(B^2 + AC)\xi}{A\sqrt{(B^2 + AC)\xi^2 + A\eta^2}},$$

$$\Omega_\eta = \frac{\eta}{\sqrt{(B^2 + AC)\xi^2 + A\eta^2}}. \quad (26)$$

A discussion on group and phase velocities is given in Ref. [58]. Eq. (25) is in the form of a conservation law. To calculate  $a_1$ , a wave volume  $V$  bounded by rays is considered. The wave volume propagates at the group velocity along the space–time rays. Integrating both sides of Eq. (25) over the volume  $V$  results in the following equations:

$$\iiint_V \left[ \frac{\partial a_1^2}{\partial t} + \frac{\partial}{\partial x}(\Omega_\xi a_1^2) + \frac{\partial}{\partial y}(\Omega_\eta a_1^2) \right] dV = 0. \quad (27)$$

The divergence theorem gives

$$\iint_S \mathbf{n} \cdot (1, \Omega_\xi, \Omega_\eta)^t a_1^2 dS = 0, \quad (28)$$

where  $\mathbf{n}$  is the outward normal of the boundary surface  $S$ , and the surface integral is taken over the sides  $\Sigma$  and the ends  $S_1$  and  $S_2$ . Since the surface  $\Sigma$  is formed by rays,  $\mathbf{n}$  is orthogonal to the ray direction  $(1, \Omega_\xi, \Omega_\eta)^t$ . This implies that  $\mathbf{n} \cdot (1, \Omega_\xi, \Omega_\eta)^t = 0$ . On the two ends of  $V$ , the normal direction is parallel to the  $t$ -axis; therefore  $\mathbf{n} = (1, 0, 0)^t$

and  $\mathbf{n} \cdot (1, \Omega_\xi, \Omega_\eta)^t = 1$  on  $S_2$ , and  $\mathbf{n} \cdot (1, \Omega_\xi, \Omega_\eta)^t = -1$  on  $S_1$ . Finally, Eq. (28) becomes

$$\iint_{S_1} a_1^2 dS = \iint_{S_2} a_1^2 dS. \quad (29)$$

The area element  $S$  can be chosen to be the area bounded by two rays and two wave fronts. Both the rays originate from the same point source. The rays and wave fronts from a point source disturbance can be parameterized by  $t$  and an initial angle  $\alpha$ . A ray can be described by  $[x(t, \alpha), y(t, \alpha)]$  with  $\alpha$  fixed, whereas a wave front is obtained by varying  $\alpha$  with  $t$  fixed. Thus the area under consideration can be described by

$$\{[x(t, \alpha), y(t, \alpha)] | t_1 \leq t \leq t_1 + dt, \alpha_1 \leq \alpha \leq \alpha_1 + d\alpha\}. \quad (30)$$

The area element can then be calculated by using the Jacobian of the transformation  $x = x(t, \alpha)$ ,  $y = y(t, \alpha)$ , and  $S$  can be written as

$$dS = dx dy = \left| \frac{\partial(x, y)}{\partial(t, \alpha)} \right| dt d\alpha = \frac{D(x, y)}{D(t, \alpha)} dt d\alpha. \quad (31)$$

Eq. (29) can now be written as

$$\iint_{S_1} a_1^2 \frac{D(x, y)}{D(t, \alpha)} dt d\alpha = \iint_{S_2} a_1^2 \frac{D(x, y)}{D(t, \alpha)} dt d\alpha. \quad (32)$$

In the limit as the area approaches zero, Eq. (32) becomes

$$a_1^2 \frac{D(x, y)}{D(t, \alpha)} \Big|_{t=t_1} = a_1^2 \frac{D(x, y)}{D(t, \alpha)} \Big|_{t=t_2}, \quad (33)$$

or along a ray,

$$a_1^2 \frac{D(x, y)}{D(t, \alpha)} = \text{const.} \quad (34)$$

The magnitude  $a_1$  can be found by calculating the following:

$$\frac{D(x, y)}{D(t, \alpha)} = |x_t y_\alpha - y_t x_\alpha|. \quad (35)$$

Eq. (35) can be integrated together with the ray equations in Eqs. (11).

Lee et al. [59] considered impulse source placed on the airfoil upper surface at the trailing edge of initial amplitude  $a_1 = 100$ , which is an arbitrary value. The airfoil considered is a NACA 64A006 at  $M = 0.85$ . Fig. 31 shows the triplet  $(x, y, a_1)$  in the upper flowfield at different times for a segment of the wave front in  $\alpha \in [104^\circ, 173^\circ]$ . Because of the convergence of the rays, the amplitude of the disturbances in the vicinity of the shock wave reaches values much larger than the initial value of 100 units. This suggests that downstream disturbances can amplify on propagating upstream towards the shock wave.

The analysis carried out by Lee et al. [59] uses an initial steady flowfield computed from an inviscid

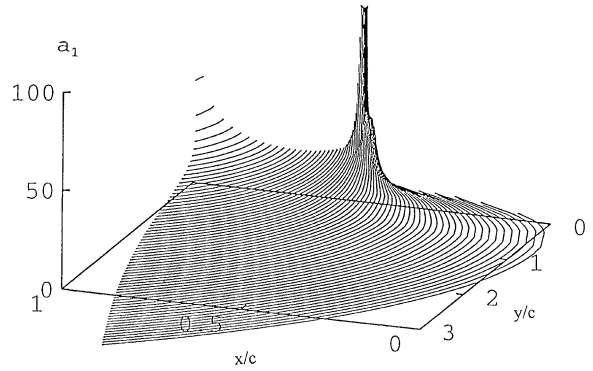


Fig. 31. Amplitude variation along wavefronts on the upper surface of a NACA 64A006 airfoil generated by an impulse source at the trailing edge at  $M = 0.85$  (from Ref. [59]).

computer code. Improvements can be made if the flowfield  $\phi$  in Eq. (15) takes into account flow separation. One of the weaknesses in the model lies in the assumption of a stationary shock wave. It is to be expected that disturbances accumulating behind the shock induce a shock motion in order to satisfy the Rankine–Hugoniot relations. The resulting shock amplitude depends on the strength of the disturbances and an approximate one-dimensional treatment of the unsteady shock motion is outlined in the next section.

### 5.2. One-dimensional unsteady shock motion

In Fig. 28 we see that upstream waves from the trailing edge can penetrate into the supersonic region ahead of the shock wave. Initially, a steady flowfield exists and close to the surface, we approximate it as one dimensional. The steady shock is assumed to be at a position  $x = x_s$ , and the upstream and downstream properties are denoted by the subscripts 1 and 2, respectively. Furthermore, we assume that in the steady flow, there is a variation of Mach number, mean velocity  $U$ , pressure and speed of sound in the  $x$ -direction along the flow. At any instant of time, if the shock displacement is  $\Delta x$ , the pressure and velocity in front and behind the shock (see Fig. 32) can be written as follows:

$$\begin{aligned} p_1 &= P_1 + \frac{dP_1}{dx} \Delta x + \tilde{p}_1, & u_1 &= U_1 - u_s + \tilde{u}_1 + \frac{dU_1}{dx} \Delta x, \\ p_2 &= P_2 + \tilde{p}_2, & u_2 &= U_2 - u_s + \tilde{u}_2 \end{aligned} \quad (36)$$

where  $P$  and  $U$  are the steady-state values of the pressure and velocity evaluated at  $x = x_s$ , respectively, and  $u_s$  is the shock velocity. The tilde quantities represent perturbations from the downstream disturbance source. The Rankine–Hugoniot relation for the instantaneous

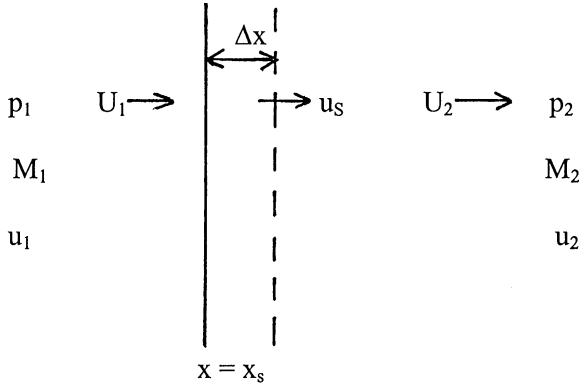


Fig. 32. Flow in front and behind a normal shock.

pressure is given as follows:

$$\frac{p_2}{p_1} = 1 + \frac{2\gamma}{\gamma + 1} \left( \frac{u_1^2}{a_1^2} - 1 \right). \quad (37)$$

Substituting Eq. (36) into Eq. (37) and retaining the linear terms only, we obtain

$$\frac{p_2}{p_1} = \frac{P_2}{P_1} + \frac{4\gamma}{\gamma + 1} M_1 \left[ \frac{dM_1}{dx} \Delta x - \frac{u_s}{a_1} + \frac{\tilde{u}_1}{a_1} \right]. \quad (38)$$

We can also express the disturbance pressure behind the shock in terms of the steady-state pressure  $P_1$  at  $x = x_s$  as follows:

$$\begin{aligned} \frac{\tilde{p}_2}{P_1} &= \frac{P_2}{P_1} \left( \frac{1}{P_1} \frac{dP_1}{dx} \Delta x + \frac{\tilde{p}_1}{P_1} \right) \\ &+ \frac{4\gamma}{\gamma + 1} M_1 \left[ \frac{dM_1}{dx} \Delta x - \frac{u_s}{a_1} + \frac{\tilde{u}_1}{a_1} \right]. \end{aligned} \quad (39)$$

For isentropic flow, the stagnation pressure  $P_0$  is related to  $P_1$  by the expression

$$P_0 = P_1 \left[ 1 + \frac{\gamma - 1}{2} M_1^2 \right]^{\gamma/(\gamma - 1)}. \quad (40)$$

Differentiating this equation with respect to  $x$  and substituting  $dP_1/dx$  into Eq. (39) we obtain

$$\begin{aligned} \frac{\tilde{p}_2}{P_1} &= \frac{P_2}{P_1} \frac{\tilde{p}_1}{P_1} + \frac{2\gamma}{\gamma + 1} M_1 \left[ \left( \frac{3 + \gamma - 2M_1^2}{2 + (\gamma - 1)M_1^2} \right) \frac{dM_1}{dx} \Delta x \right. \\ &\left. - \frac{2u_s}{a_1} + \frac{2\tilde{u}_1}{a_1} \right]. \end{aligned} \quad (41)$$

This equation can be used in conjunction with the analysis of Section 5.1. Given a source of known frequency and amplitude place at the trailing edge, the fluctuating pressure and velocity in front and behind the shock wave can be computed. Upon substituting these quantities into Eq. (41) we obtain a differential equation

for the shock displacement  $\Delta x$  as follows:

$$\begin{aligned} \frac{2}{a_1} \frac{d\Delta x}{dt} - \left( \frac{3 + \gamma - 2M_1^2}{2 + (\gamma - 1)M_1^2} \right) \frac{dM_1}{dx} \Delta x \\ + \frac{\gamma + 1}{2\gamma M_1} \left( \frac{\tilde{p}_2}{P_1} - \frac{P_2}{P_1} \frac{\tilde{p}_1}{P_1} \right) - \frac{2\tilde{u}_1}{a_1} = 0, \end{aligned} \quad (42)$$

which can be computed at each time step in the Euler time integration scheme used in Ref. [59] to solve Eq. (11). This approach gives a very rough estimation for  $\Delta x$  since the one-dimensional approach assumes a normal shock and  $\partial \tilde{p}_2 / \partial y \neq 0$ , whereas in the two-dimensional wave equation  $\tilde{p}_2$  is also a function of  $y$ .

For a sinusoidal disturbance source, we can write the shock displacement, velocity and perturbation quantities as follows:

$$\begin{aligned} \Delta x &= x_0 e^{i\omega t}, \quad u_s = i\omega x_0 e^{i\omega t}, \quad \tilde{u}_1 = \bar{u}_1 e^{i\omega t}, \\ \tilde{p}_1 &= \bar{p}_1 e^{i\omega t}, \quad \tilde{p}_2 = \bar{p}_2 e^{i\omega t}. \end{aligned} \quad (43)$$

Eqs. (38) and (41) can be written as follows:

$$\frac{p_2}{p_1} = \frac{P_2}{P_1} + \frac{4\gamma}{\gamma + 1} M_1 \left[ \frac{dM_1}{dx} - \frac{i\omega}{a_1} + \frac{\bar{u}_1}{a_1} \right] x_0 e^{i\omega t}, \quad (44)$$

$$\begin{aligned} \frac{\tilde{p}_2}{P_1} &= \left\{ \frac{2\gamma}{\gamma + 1} M_1 \left( \left[ \frac{3 + \gamma - 2M_1^2}{2 + (\gamma - 1)M_1^2} \right] \right. \right. \\ &\left. \left. \frac{dM_1}{dx} - \frac{2i\omega}{a_1} \right] x_0 + \frac{2\bar{u}_1}{a_1} \right\} + \frac{P_2}{P_1} \frac{\bar{p}_1}{P_1} \left. \right\} e^{i\omega t}. \end{aligned} \quad (45)$$

If we assume the disturbances in the supersonic region upstream of the shock to be negligible, Eqs. (44) and (45) reduce to those derived by Tidjeman [4]. Furthermore, if  $dM_1/dx = 0$ , and  $\bar{u}_1 = 0$ , Eq. (44) shows that the maximum phase difference between the shock displacement and the pressure fluctuation is  $90^\circ$ .

An example in using Eqs. (44) and (45) to relate pressure fluctuations with shock motion is given by Tidjeman [4] using experimental steady-state data measured on the NACA 64A006 airfoil at  $M = 0.90$ . The periodic shock motion is of the type A with frequency and amplitude of 120 Hz and  $x_0/c = 0.05$ , respectively. The steady-state Mach number in front of the shock wave determined from quasi-steady flow is  $M_1 = 1.18$  and  $dM_1/dx = 1.7$ . The shock strength  $p_2/p_1$  computed from Eq. (44) is nearly 3% larger than that determined from quasi-steady flow with a phase shift of  $64^\circ$ . Alternatively, the unsteady pressure can be measured and the shock amplitude is then computed from either Eq. (44) or Eq. (45).

## 6. Propagation of disturbances in the wake

One of the early studies of pressure fluctuations in the wakes of two-dimensional airfoils in large wind tunnels

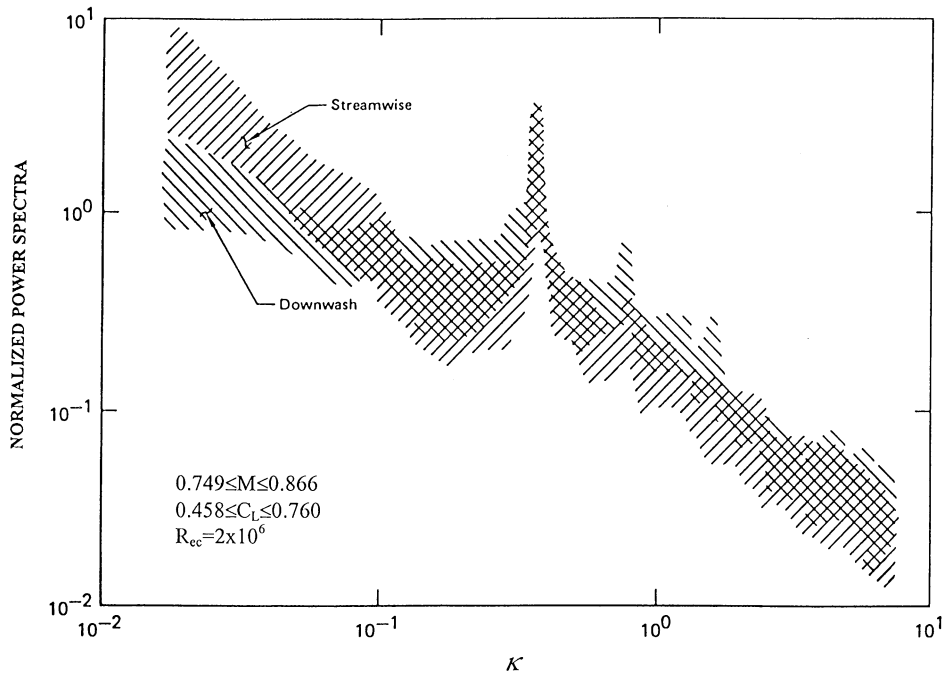


Fig. 33. Normalized power spectra of streamwise and downwash velocity fluctuations at upper edge of wake (from Ref. [25]).

was carried out by Sorenson et al. [62] on the NACA 65<sub>1</sub>-213 and NACA 23013 airfoils from  $0.6 < M < 0.8$ ,  $-2 < \alpha < 5^\circ$ , and  $9 < R_{ec} < 11 \times 10^6$ . The unsteady pressures in the wake were random until periodic shock oscillation appeared on the airfoil whereupon the wake pressure fluctuations showed a distinct frequency corresponding to the shock frequency. The stream angle fluctuations were also measured on the NACA 23013 airfoil at  $x/c = 0.7$  from the trailing edge for various Mach numbers. Results obtained at  $M = 0.75$  and  $\alpha = 5^\circ$  showed the maximum angle fluctuations can be as large as  $5^\circ$ . This indicates that significant transverse oscillations of the wake can occur when periodic shock motion appears at buffeting.

A detail investigation of the velocity fluctuations in the wake during buffeting was conducted by Roos and Riddle [25] on the Douglas Aircraft profile DSMA 523 which is a Whitcomb-type supercritical airfoil design for  $M = 0.82$  and  $C_L = 0.56$ . They mounted a pair of crossed-sensor hot film anemometer probes on a vertical traversing rig located 0.25 chord downstream of the trailing edge. The probe measured the streamwise and downwash ( $u-w$ ) components of the velocity field. The overall intensity of velocity fluctuations at the upper edge of the wake varied greatly with flow conditions. However, the shapes of the power spectra of the unsteady  $u$ - and  $w$ - velocity components remained remarkably similar. This is shown in Fig. 33 at a location  $x/c = 0.25$  from the trailing edge for a Mach number and lift coefficient

range of  $0.749 \leq M \leq 0.866$  and  $0.458 \leq C_L \leq 0.760$  at  $R_{ec} = 2 \times 10^6$ . The spectra show a pair of pronounced peaks at  $\kappa = 0.4$  and  $0.8$ , corresponding to the fundamental and first harmonic of the periodic shock motion.

Evidence of the coupling between the shock motion and the wake oscillation can be obtained from the correlation of the surface pressure fluctuations on the airfoil induced by the shock and the velocity fluctuations in the wake. Roos and Riddle [25] measured the coherence function between the downwash fluctuations at the upper wake edge and the airfoil surface pressure fluctuations at  $x/c = 0.9$ . The coherence function is defined as

$$\gamma_{pw}^2 = \frac{|S_{pw}|^2}{S_p S_w} \quad (46)$$

where  $S_{pw}$  is the cross-spectral density between the pressure  $p$  and the downwash  $w$ ,  $S_p$  and  $S_w$  are the power spectral densities of  $p$  and  $w$ , respectively. Fig. 34 shows for different  $M$  and  $C_L$  combinations, the pressure and downwash are essentially incoherent except at very low frequencies and in a few narrow frequency bands. At  $\kappa = 0.4$  and  $0.8$ , a coherence of 0.6–0.7 is obtained, and at the other lower frequency bands, the coherence function decreases with increasing  $\alpha$  and  $M$ . Roos and Riddle [25] were not able to detect the propagation direction of the  $\kappa = 0.4$  disturbance. This was later shown by Roos [32] from broadband pressure correlations on the airfoil surface that upstream propagation of disturbances is

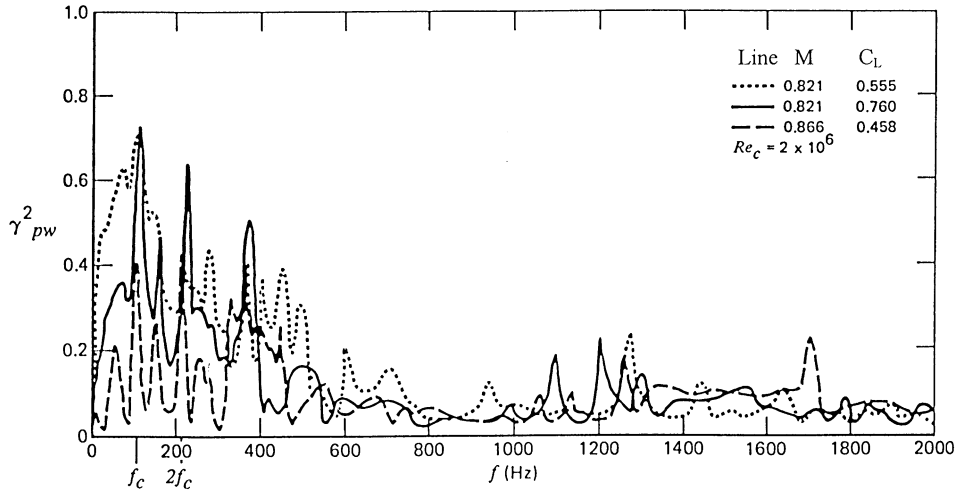


Fig. 34. Coherence of pressure and downwash fluctuations (from Ref. [25]).

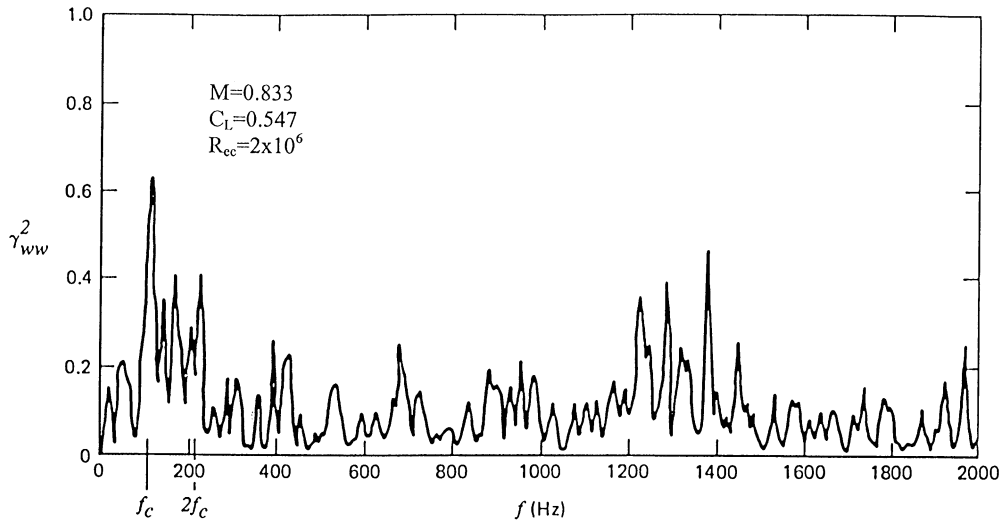


Fig. 35. Coherence of downwash fluctuations on upper and lower edges of wake (from Ref. [25]).

possible in the boundary layer on the airfoil upper surface for attached flow. For fully separated flow, only pressure waves travelling downstream from the shock to the trailing edge are detected. The  $\kappa = 0.4$  disturbance Roos and Riddle [25] measured is probably the same shock-induced disturbance which has propagated past the trailing edge in the downstream direction.

Across the wake, Fig. 35 shows the coherence function of the downwash at the upper and lower edges at  $\kappa = 0.4$  is as high as the pressure–velocity coherence  $\gamma_{pw}^2$  at that frequency shown in Fig. 34. The magnitude of the coherence function of the first harmonic is also quite high and the figure shows some high-frequency components that

correlate well in velocity but not with the pressure on the airfoil as shown in Fig. 34 for  $\gamma_{pw}^2$ . Phase measurements of the vertical velocity component  $w$  on the upper and lower surfaces are essentially in phase at  $\kappa = 0.4$ , and this indicates the fluctuations amount to a vertical undulation or flapping of the wake. High-speed cinematography by Mohan [53] shows the wake to oscillate up and down. Similarly, Finke [33] found from optical studies on the 20% circular-arc airfoil that the wake showed cross-wise oscillations with the frequency of the shock wave motion. These observations are in agreement with the quantitative measurements of Roos and Riddle [25].

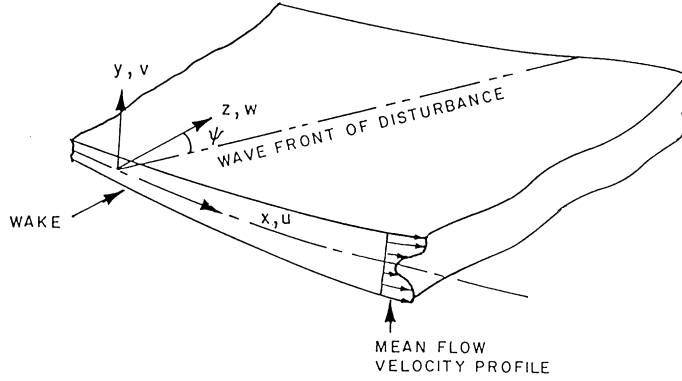


Fig. 36. Schematic of wake flow and notations.

Analysis of the propagation of disturbances in the wake flow is useful in the study of the oscillatory shock motion on an airfoil. Undoubtedly, Navier–Stokes computer codes (see Section 7) are able to predict the wake properties with good accuracy. However, qualitative features of the wake can be obtained from a study of wave propagation in free shear layers which include wake flows. Stability of shear flows is a classical topic widely studied since the early works of Lord Rayleigh [63]. This subject will not be dealt with in any details and the reader can refer to the excellent text by Betchov and Criminale [64].

6.1. Linearized equations of motion for compressible flows

Following the approach given by Lessen et al. [65] in a study of the propagation of three-dimension disturbances between two parallel streams of a compressible fluid, the linearized equations for a two-dimensional wake are derived in this section. A sketch of the wake and the co-ordinate system is shown in Fig. 36.

A Cartesian co-ordinate system normalized with respect to the wake half-width  $b$  is used and the mean flow velocity  $U$  is assumed to be a function of  $y$  only. The perturbation velocity components are  $u', v'$  and  $w'$ , and  $p', T'$ , and  $\rho'$  are the pressure, temperature and density disturbances, respectively. For reference quantities, the mean velocity outside the wake  $U_w$  is used for velocities, and the initial upstream mean quantities are used for the thermodynamic variables. For spatial instability analysis, the disturbance quantities in nondimensional form can be written as follows:

$$\{u', v', w', p', T', \rho'\} = \{f(y), \alpha\phi(y), -ih(y), \pi(y), \theta(y), r(y)\} \exp[i(\alpha x + \beta z - \bar{\omega}t)]. \quad (47)$$

where  $\alpha$  is a complex number, the real part  $\alpha_r$  is the wave number and the imaginary part  $-\alpha_i$  is the amplification

rate for a spatially growing disturbance. The wave number in the  $z$ -direction is  $\beta$ , and  $\bar{\omega}$  is the nondimensional circular frequency. The perturbed compressible flow equations can be written in nondimensional form as follows:

$$\text{Continuity } i\alpha(\bar{U} - c)r + \alpha\bar{\rho}'\phi = -\bar{\rho}[i(\alpha f + i\beta h) + \alpha\phi'], \quad (48)$$

$$\text{Momentum } \bar{\rho}[i(\bar{U} - c)f + \bar{U}'\phi] = -\frac{i\pi}{\gamma M^2}$$

$$i\alpha^2\bar{\rho}(\bar{U} - c)\phi = -\frac{\pi'}{\gamma M^2}$$

$$i\alpha\bar{\rho}(\bar{U} - c)h = \frac{\beta\pi}{\gamma M^2}, \quad (49)$$

$$\text{Energy } \bar{\rho}[i\alpha(\bar{U} - c)\theta + \alpha\bar{T}'\phi] = -(\gamma - 1)[i(\alpha f + i\beta h) + \alpha\phi'], \quad (50)$$

$$\text{State } \frac{\pi}{\bar{p}} = \frac{r}{\bar{\rho}} + \frac{\theta}{\bar{T}}. \quad (51)$$

where  $c = \bar{\omega}/\alpha$ ,  $\gamma$  is ratio of the specific heats, the bar denotes mean quantities and the superscript ' denotes differentiation with respect to  $y$ . This system can further be reduced to the following:

$$i\bar{\rho}[(\bar{U} - c)\phi' - \bar{U}'\phi] = -\frac{\pi}{\gamma M^2} \left[ \left(1 + \frac{\beta^2}{\alpha^2}\right) - (\bar{U} - c)^2 \frac{M^2}{\bar{T}} \right]. \quad (52)$$

$$\alpha^2\bar{\rho}(\bar{U} - c)\phi = \frac{i\pi'}{\gamma M^2}. \quad (53)$$

6.2. Stability analysis of a two-dimension compressible wake

These equations have been solved by Chan and Leong [66] for a wake with the following velocity and

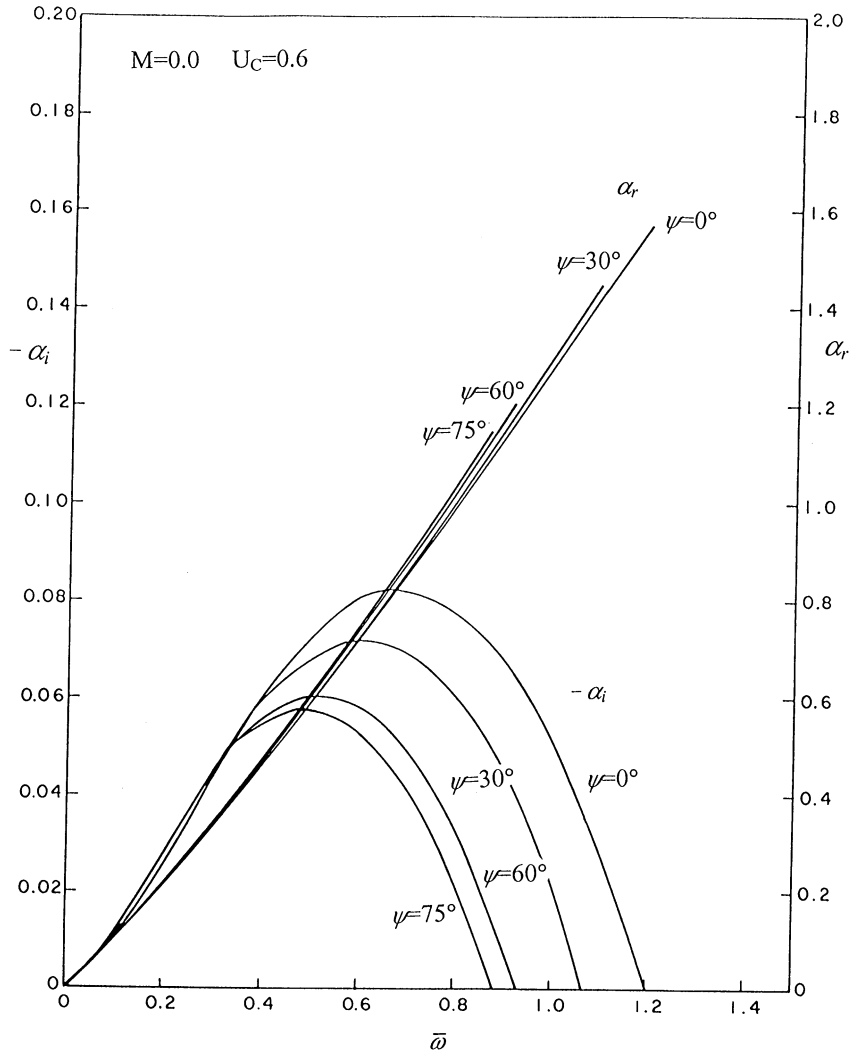


Fig. 37. Wave numbers and amplification rates versus frequency for a wake with  $U_c = 0.6$  (from Ref. [66]).

temperature distributions:

$$\frac{1 - \bar{U}}{1 - \bar{U}_c} = \exp(-0.693Y^2), \tag{54}$$

$$\frac{\bar{T} - 1}{\bar{T}_c} = \exp(-0.367Y^2), \tag{55}$$

where

$$Y = \int_0^y \frac{1}{\bar{T}} dy, \tag{56}$$

and the subscript c denotes the centerline of the wake. Chan and Leong [66] analyzed the case where the wake

is confined between two parallel walls with vanishing normal velocity boundary conditions on the walls. The angle between the normal to the wavefront and the direction of the mean flow is defined as:

$$\psi = \arctan(\beta/\alpha_r). \tag{57}$$

A typical example of the variation of wave number and amplification factor with  $\bar{\omega}$  is shown in Fig. 37 for a wake with centerline velocity  $U_c = 0.6$  and Mach number  $M = 0$ . For different values of  $U_c$  and  $M$ , the curves look similar in shape except that the amplification region is different. At low  $\bar{\omega}$ , the effect of  $M$  is small. For two-directional disturbances, we consider only the curves for  $\psi = 0^\circ$ .

To obtain an estimate of the behavior of shock-induced pressure disturbances from the airfoil, we take as an example the BGK No. 1 airfoil at  $M = 0.722$  and  $\alpha = 6^\circ$  (see Table 1). The measured frequency is  $f_m = 75$  Hz, and assuming the wake width to be the same as the thickness ratio of the airfoil, and  $U_w = U$ , the freestream value, we calculate a Strouhal number  $St = f_m b / U_w$  to be about 0.01. The amplification rate  $-\alpha_i$  is approximately 0.007. In other words, the disturbance originating from the shock wave grows slowly in the  $x$ -direction and the phase velocity is close to  $U_w$ . The most amplified mode with  $-\alpha_i \approx 0.081$  occurs at a much higher frequency than the disturbance from the airfoil upper surface. Although we cannot obtain detail information on disturbances as they travel downstream, stability analysis predicts that eventually the wake will be dominated by the most amplified mode. The disturbances from the periodic shock motion will not be significant far downstream and they will be overshadowed by the more highly amplified disturbances.

It is interesting to note from Fig. 33 that the power spectral density plot does not show any significant peaks at frequencies higher than those at  $\kappa = 0.4$  and 0.8 which represent disturbances originating from the shock-induced separation. At this location from the trailing edge ( $x/c = 0.25$ ), it appears that the dominant mode from stability analysis which has a higher frequency is too weak to be detected. It will be informative if a more detail study of the wake is carried out by carrying out space-time cross-correlation of the velocity fluctuations for sufficiently far downstream positions from the trailing edge to analyze the large-scale structure of the wake.

Refinements in the stability analysis can be obtained by including nonlinear effects [67] and interaction with background turbulence [68]. However, the overall qualitative behavior of the disturbance can adequately be predicted from an inviscid theory.

## 7. Numerical studies of periodic shock oscillations

### 7.1. Navier–Stokes solutions

The three-dimensional time-dependent compressible Navier–Stokes equations written in conservative form can be expressed as follows [69]:

$$\frac{\partial \hat{Q}}{\partial t} + \frac{\partial}{\partial \xi}(\hat{F} - \hat{F}_v) + \frac{\partial}{\partial \eta}(\hat{G} - \hat{G}_v) + \frac{\partial}{\partial \zeta}(\hat{H} - \hat{H}_v) = 0, \quad (58)$$

where

$$\hat{Q} = \frac{Q}{J}. \quad (59)$$

The conserved variables vector  $Q$  and the inviscid flux vectors  $\hat{F}$ ,  $\hat{G}$ ,  $\hat{H}$  are defined by

$$Q = \begin{pmatrix} \rho \\ \rho u \\ \rho v \\ \rho w \\ e \end{pmatrix}, \quad \hat{F} = \frac{1}{J} \begin{pmatrix} \rho U \\ \rho U u + \xi_x p \\ \rho U v + \xi_y p \\ \rho U w + \xi_z p \\ (e + p)U - \xi_t p \end{pmatrix},$$

$$\hat{G} = \frac{1}{J} \begin{pmatrix} \rho V \\ \rho V u + \eta_x p \\ \rho V v + \eta_y p \\ \rho V w + \eta_z p \\ (e + p)V - \eta_t p \end{pmatrix}, \quad \hat{H} = \frac{1}{J} \begin{pmatrix} \rho W \\ \rho W u + \zeta_x p \\ \rho W v + \zeta_y p \\ \rho W w + \zeta_z p \\ (e + p)W - \zeta_t p \end{pmatrix}, \quad (60)$$

The Jacobian of the transformation between the Cartesian variables  $(x, y, z)$  and the body fitted coordinates  $(\xi, \eta, \zeta)$  is given by

$$J = \frac{\partial(\xi, \eta, \zeta)}{\partial(x, y, z)}, \quad (61)$$

and the contravariant velocities are

$$U = \xi_x u + \xi_y v + \xi_z w + \xi_t, \\ V = \eta_x u + \eta_y v + \eta_z w + \eta_t, \\ W = \zeta_x u + \zeta_y v + \zeta_z w + \zeta_t. \quad (62)$$

The corresponding viscous flux vectors are denoted by  $\hat{F}_v$ ,  $\hat{G}_v$ ,  $\hat{H}_v$  and they are given as follows:

$$\hat{F}_v = \frac{1}{J} \begin{pmatrix} 0 \\ \xi_x \tau_{xx} + \xi_y \tau_{xy} + \xi_z \tau_{xz} \\ \xi_x \tau_{yx} + \xi_y \tau_{yy} + \xi_z \tau_{yz} \\ \xi_x \tau_{zx} + \xi_y \tau_{zy} + \xi_z \tau_{zz} \\ \xi_x b_x + \xi_y b_y + \xi_z b_z \end{pmatrix},$$

$$\hat{G}_v = \frac{1}{J} \begin{pmatrix} 0 \\ \eta_x \tau_{xx} + \eta_y \tau_{xy} + \eta_z \tau_{xz} \\ \eta_x \tau_{yx} + \eta_y \tau_{yy} + \eta_z \tau_{yz} \\ \eta_x \tau_{zx} + \eta_y \tau_{zy} + \eta_z \tau_{zz} \\ \eta_x b_x + \eta_y b_y + \eta_z b_z \end{pmatrix},$$

$$\hat{H}_v = \frac{1}{J} \begin{pmatrix} 0 \\ \zeta_x \tau_{xx} + \zeta_y \tau_{xy} + \zeta_z \tau_{xz} \\ \zeta_x \tau_{yx} + \zeta_y \tau_{yy} + \zeta_z \tau_{yz} \\ \zeta_x \tau_{zx} + \zeta_y \tau_{zy} + \zeta_z \tau_{zz} \\ \zeta_x b_x + \zeta_y b_y + \zeta_z b_z \end{pmatrix}, \quad (63)$$

where

$$b_{x_i} = u_j \tau_{x_i x_j} - \dot{q}_{x_i}. \quad (64)$$

The pressure is obtained from the equation of state for a perfect gas and is given by

$$p = (\gamma - 1) \left[ e - \rho \frac{(u^2 + v^2 + w^2)}{2} \right]. \quad (65)$$

The shear stress and heat flux terms are defined by

$$\tau_{x_i x_j} = \frac{M}{Re_c} \left[ \mu \left( \frac{\partial u_i}{\partial x_j} + \frac{\partial u_j}{\partial x_i} \right) + \lambda \frac{\partial u_k}{\partial x_k} \delta_{ij} \right], \quad (66)$$

$$\dot{q}_{x_i} = - \left[ \frac{M}{Re_c Pr(\gamma - 1)} \right] \frac{\partial a^2}{\partial x_i}, \quad b_{x_i} = u_j \tau_{x_i x_j} - \dot{q}_{x_i}, \quad (67)$$

where  $\mu$ ,  $Pr$  and  $\lambda$  are the viscosity, Prandtl number and bulk viscosity coefficient, respectively. The boundary conditions on the body are the no slip, zero normal pressure gradient and adiabatic wall conditions. For turbulent computations, the Baldwin and Lomax [70] or the Spalart and Allmaras [71] models are commonly used.

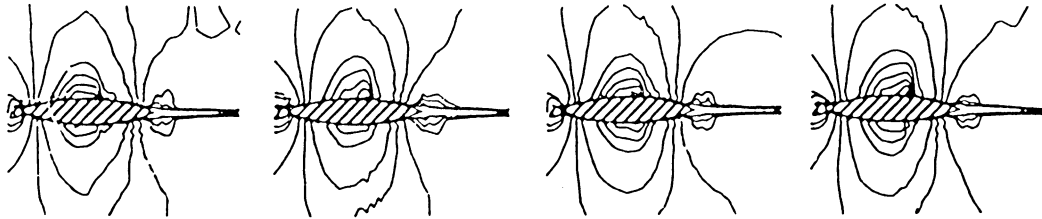
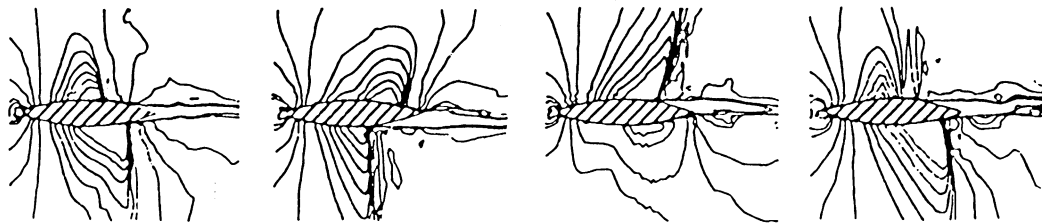
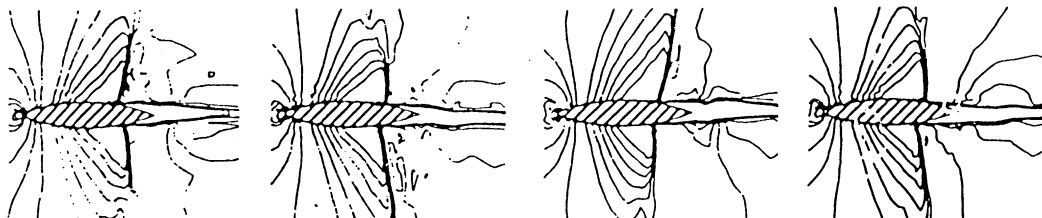
Various forms of these equations have been used by different authors in their formulation of numerical schemes to solve viscous flow problems. One of the earliest attempts to use CFD in solving the unsteady self-sustained shock oscillations on an 18% thick circular arc airfoil was carried out by Levy [72] who modified Deiwert's [73,74] code to solve the time-dependent, two-dimensional Reynolds averaged Navier–Stokes equations. Levy [72] used MacCormack's explicit solution scheme with an algebraic eddy viscosity turbulence model. The code also simulates the effects of the wind tunnel walls. The results demonstrate the capability of computer codes to predict unsteady turbulent flows involving weak and strong shock wave-boundary layer interactions. The intensity of airfoil surface pressure, skin friction fluctuations, reduced frequency of pressure fluctuations, oscillatory regions of trailing edge and shock-induced separation, and the Mach number range for periodic flows agree qualitatively with experiments. For example, Fig. 38 shows the computed Mach contours for  $M = 0.72$ , 0.754 and 0.783. The time is measured by the chord lengths travelled by the mean flow ( $Ut/c$ ) for the unsteady case, and one cycle of oscillation is shown.

The shock wave and boundary layer separation features for the types of flow discussed in Section 4 are reproduced computationally at least qualitatively. The pressures computed at two locations ( $x/c = 0.5$  and 0.775) at  $M = 0.76$  and  $Re_c = 11 \times 10^6$  are compared with experiments [24] in Fig. 39 and they show a periodic behavior having approximately 180° phase reversal on the upper and lower surfaces. In general, the computed pressures are larger and the frequency is lower with a reduced frequency  $k \approx 0.4$  compared to a measured value of 0.49. Levy [72] concluded that turbulence models using experimental data from steady flow measurements can improve the time-dependent solutions for unsteady flows. Marvin et al. [75] conducted experiments on an 18% thick biconvex airfoil and measured the ensemble-averaged mean and fluctuating velocities, turbulent kinetic energy, and turbulent shear stress for various times within a cycle of oscillation using a conditional sampling technique. These data can be used to develop better turbulence modelling for periodic flows involving shock-induced separations.

Steger [76] developed an implicit finite difference scheme with transformations that permit use of automatic grid generation to solve the thin-layer Navier–Stokes equations. For turbulence modelling, he used a two-layer algebraic eddy viscosity model following Cebecci's approach [77]. Applying the computer code to an 18% circular arc airfoil, Steger [76] found that the reduced frequency  $\kappa$  for periodic shock motion was 0.82 instead of 0.81 from Levy's [72] computations. However, periodic shock motion was not detected at  $M = 0.754$  but was delayed to  $M = 0.783$ .

Edwards and Thomas [78] used the algorithm described by Rumsey et al. [79] on an 18% thick circular arc airfoil and found the reduced frequency  $\kappa = 0.812$  agreeing with both Levy [72] and Steger [76]. Their results show that unsteady periodic flow occurs at  $M = 0.78$ . Steady trailing-edge separation occurs at  $M = 0.754$ , whereas Levy's [72] computations show large shock movements of the type C appear at this Mach number. It appears that the Navier–Stokes solutions of Levy [72], Steger [76] and Edwards and Thomas [78] predict the frequency fairly consistently, but the Mach number for the onset of periodic flows differs with the three computational schemes.

Gerteisen [80] described an Euler/Navier–Stokes solution algorithm and recommended an implicit scheme for viscous transonic flow. The Baldwin–Lomax turbulence model was used but very limited studies were carried out on periodic flows. The only example given is for a 14% thick circular-arc airfoil where type A shock oscillations were observed. There were some discrepancies with Mabey et al. [7] experiments on the domain for periodic flows because of the poor shock resolution. Gerteisen [80] suggested that more accurate results probably could be obtained using a later developed mesh

STEADY FLOW, TRAILING-EDGE SEPARATION,  $M=0.720$ UNSTEADY FLOW, OSCILLATORY SEPARATION,  $M=0.754$ STEADY FLOW, SHOCK-INDUCED SEPARATION,  $M=0.783$ 

0.0

2.6

5.2

7.8

CHORDS TRAVELED

Fig. 38. Computed Mach contours,  $M = 0.72, 0.754, \text{ and } 0.783$ ,  $R_{ec} = 10 \times 10^6$  (from Ref. [72]).

adaptation facility and time iteration algorithm, but no new results were given.

One of the more recent attempts to reproduce McDevitt et al.'s [6] experimental results using a Navier–Stokes solver is given in Ref. [69]. Rumsey et al. [69] solved Eq. (58) by using the TLNS3D [81] and CFL3D [82] codes in conjunction with subiterations to advance the equation of motion in a time accurate manner. For turbulence modelling, both the Baldwin–Lomax [70] and the Spalart–Allmaras [71] models are used. The TLNS3D code is a central-difference code. Second-order central differences are used for all spatial derivatives, and a blend of second-difference and fourth-difference artificial dissipation terms is used to maintain numerical stability. These artificial dissipation terms can be added in either scalar or matrix form. Rumsey et al. [69] used matrix dissipation and a five-stage Runge–Kutta time marching scheme. The CFL3D code uses upwind-biased spatial differencing for the inviscid terms, and flux limiting is used to obtain smooth solutions in the vicinity of

the shocks. All viscous terms are centrally differenced, and the equations are solved implicitly in time using a three-factor approximate factorization. The fluxes at the cell faces are obtained using Roe's [83] flux-difference-splitting scheme.

Rumsey et al. [69] computed the flow over an 18% thick circular-arc airfoil at Mach numbers between  $M = 0.72$  to  $0.76$  and  $R_{ec} = 11 \times 10^6$ . The effects of time step, subiteration type, grid size, grid extent, Mach number, turbulence model, computer code, and tunnel walls were investigated. Most of the results given were obtained using a  $185 \times 65$  C mesh, although some calculations were carried out on a  $369 \times 129$  grid to illustrate the effect of grid size. The computed reduced frequency, for example, depends on the computer code used. For  $M = 0.76$  and using the Spalart–Allmaras model, CFL3D gives  $k$  values ranging from 0.47 to 0.495 for the two grids and different time steps. The TLNS3D computes reduced frequency values  $k$  between 0.459 to 0.498. These two codes give frequency values close to the

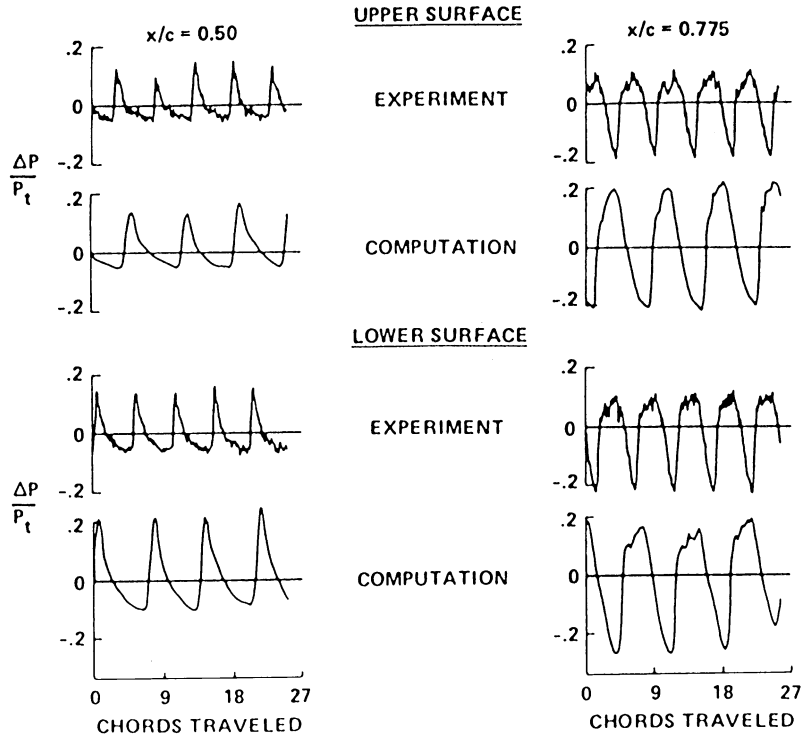


Fig. 39. Surface pressure time histories,  $M = 0.76$  and  $Re_c = 11 \times 10^6$  (from Ref. [24]).

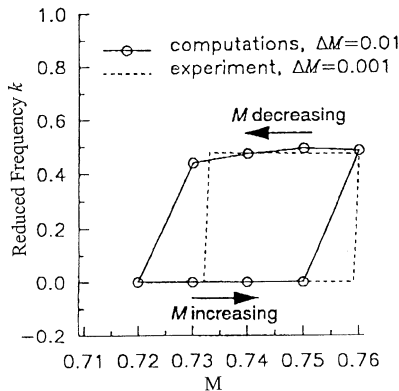


Fig. 40. Computed hysteresis for circular-arc airfoil (from Ref. [69]).

experimental value [6] of 0.49 and are more accurate than the results obtained by other Navier–Stokes codes described above. The choice of turbulence model is important, and the Baldwin–Lomax model gives a value nearly 20% less for the worst of the two cases presented by Rumsey et al. [69].

The hysteresis effect detected by McDevitt et al. [6] was reproduced from the CFL3D code and is shown in Fig. 40. Starting at  $M = 0.70$  a steady state is obtained

and  $M$  is increased in increments of 0.01. The flow is practically steady up to  $M = 0.75$  and at  $M = 0.76$  periodic flow is established. Starting from  $M = 0.76$ , the code is run time accurately at decreasing Mach numbers and unsteady flow is detected until  $M = 0.73$  where further increase in  $M$  results in a steady-state solution. The range of  $M$  where hysteresis was observed by McDevitt et al. [6] is shown in the figure by the dotted lines. The onset boundary of the unsteady flow domain for  $dM/dt > 0$  is quite well predicted, but computations predict a smaller value of the quenching boundary for  $dM/dt < 0$ .

The shock location is shown in Fig. 41 against non-dimensional time  $\bar{t}$ . Within one cycle of oscillation,  $\bar{t}$  varies between 0 and 1, and  $\bar{t} = 0$  when the shock wave is at the airfoil mid-chord or closest to it. Both the TLNS3D and CFL3D codes using the Spalart–Allmaras model give results close to McDevitt et al.’s [6] experimental values. The Baldwin–Lomax turbulence model from CFL3D predicts a significantly smaller shock movement of the type A. It appears that turbulence modelling plays an important role in the type of shock oscillation as witnessed from this particular example where a type C can change to a type A motion using two different turbulence models.

The mechanisms of the origin of shock oscillations on an 18% thick biconvex circular-arc airfoil were investigated by Raghunathan et al. [84] using a thin layer

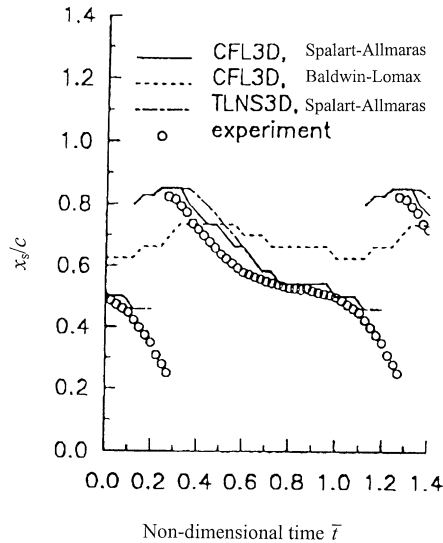


Fig. 41. Variation of shock location for circular-arc airfoil at  $M = 0.76$  (from Ref. [69]).

Navier–Stokes code. An upwind implicit predictor/corrector cell-centered finite volume scheme is adopted together with the Baldwin–Lomax turbulence model. A hyperbolic  $320 \times 64$  C-grid is used in the numerical computations. At  $M = 0.771$  and  $Re_{cc} = 11 \times 10^6$ , the reduced frequency  $k$  predicted is 0.44, lower than both the experimental value of 0.49 and predictions by Rumsey et al. [69]. Similar to McDevitt's [50] experiments, a splitter plate of length 25% chord placed at the trailing edge can eliminate periodic shock oscillations at this Mach number. A 9% chord splitter plate at the trailing edge changes the shock oscillation from type B to type A. A numerical experiment was carried out using a 25% chord long splitter plate to obtain an initially steady flow. The plate was then removed and the flow development was investigated at various times until periodic shock movement was established. Similar to the experimental evidence in Section 4, Raghunathan et al. [84] demonstrated from numerical simulations that shock-induced separation plays a leading role in the origin of periodic shock oscillations.

The comparisons between CFD and experiments given above are carried out mostly for an 18% thick circular-arc airfoil since abundant experimental data are available for code validation. In fact, the objectives of McDevitt et al.'s [6] investigations were to provide benchmark test cases to evaluate numerical simulation codes. For airfoils at incidence, Raghunathan et al. [85] applied their Navier–Stokes code to a NACA 0012 airfoil at  $M = 0.7$ ,  $Re_{cc} = 10 \times 10^6$  and  $\alpha = 6^\circ$  and showed the shock motion is of the type B. From pressure and skin friction distributions at various times in an oscillation cycle, they suggested that periodic shock motion is triggered by

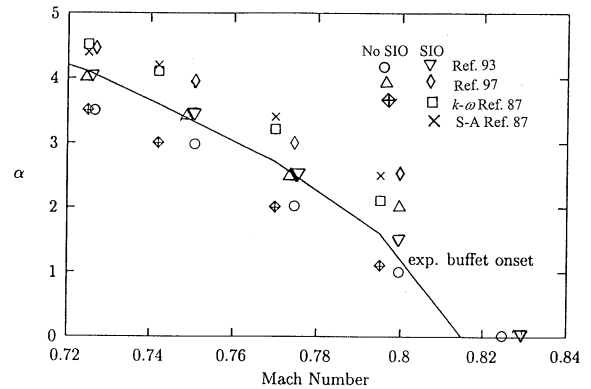


Fig. 42. Buffet onset for NACA 0012 airfoil. SIO stands for shock-induced oscillations (from Ref. [87]).

a shock-induced separation bubble, and the motion is sustained by expansion and collapse of the bubble on the suction surface. The communication between the two surfaces is through the trailing edge.

Hirose and Miwa [9] used the NSFOIL [86] code to predict unsteady flow characteristics on the NACA 0012 and GK 75-06-12 airfoils. The two-dimensional code uses an implicit approximate factorization scheme to solve the time-averaged thin layer Navier–Stokes equations. For turbulence modelling, the Baldwin–Lomax [70] algebraic model is used. The study was mainly concerned with the effects of Reynolds number, incidence angle, and transition on buffeting. The mesh is not sufficiently fine to give good shock resolutions. However, computed buffet boundaries compare reasonably well with experiments.

The accuracy of various turbulence models was evaluated by Barakos and Drikakis [87] using a second-order time accurate implicit-unfactored scheme [88] which solves in a coupled fashion the Navier–Stokes and turbulence transport equations. A Riemann solver in combination with a third-order upwind scheme is used in spatial discretisation of the equations. The algebraic Baldwin and Lomax [70] model, Spalart and Allmaras [71] one equation model, Launder and Sharma [89] and Nagano and Kim [90] linear  $k-\epsilon$  models, Sofialidis and Prinos [91]  $k-\omega$  nonlinear eddy viscosity model were assessed on the NACA 0012 airfoil at Mach numbers between 0.7 and 0.8, angle of incidence below  $5^\circ$  and  $Re_{cc}$  between  $10^6$  and  $14 \times 10^6$  following the test conditions from experiments carried out by McDevitt and Okuno [12]. The buffet boundary was defined as the onset of periodic shock motion (see Section 3 for other definitions), and for the NACA 0012 airfoil at  $Re_{cc} = 10 \times 10^6$ , the incidence versus Mach number buffet boundary is shown in Fig. 42. The computed boundary is shifted to higher  $\alpha$  values than the experiments. The Spalart–Allmaras model gives very close results to the  $k-\omega$  model and the difference

increases with Mach number. The linear  $k-\varepsilon$  models fails to predict buffet since only steady solutions are obtained. No results from the Baldwin–Lomax model are available.

### 7.2. Interactive boundary layer coupling method

An alternative to solving the Navier–Stokes equations directly is the interactive boundary layer coupling method. Essentially, the procedure involves the solution of an outer inviscid region and an inner viscous boundary layer. There are numerous inviscid codes available, but a time consuming one is not really necessary since the method is only an approximation to a very complex problem with unsteady attached and separated flows on the airfoil surfaces. We shall only present the simplest method to compute the transonic flowfield using the transonic small disturbance equation which has been widely used to compute unsteady transonic flows about isolated wings and complete aircraft configurations for aeroelastic applications.

The three-dimensional TSD equation in cartesian coordinates can be expressed in the following form [92]:

$$\frac{\partial f_0}{\partial t} + \frac{\partial f_1}{\partial x} + \frac{\partial f_2}{\partial y} + \frac{\partial f_3}{\partial z} = 0, \quad (68)$$

where  $x$ ,  $y$  and  $z$  denote the nondimensional physical co-ordinates in the streamwise, spanwise and vertical directions, respectively, and

$$\begin{aligned} f_0 &= -A\phi_t - B\phi_x, \\ f_1 &= E_1\phi_x + F_1\phi_x^2 + G_1\phi_y, \\ f_2 &= \phi_y + H_1\phi_x\phi_y, \\ f_3 &= \phi_z. \end{aligned} \quad (69)$$

Here  $\phi$  is the velocity potential and the coefficients in Eq. (69) are defined as:

$$\begin{aligned} A &= M^2, \quad B = 2M^2, \quad E_1 = 1 - M^2, \\ F_1 &= -[3 - (2 - \gamma)M^2]M^2/2, \\ G_1 &= -M^2/2, \quad H_1 = -M^2 \end{aligned} \quad (70)$$

where  $\gamma$  is the specific heats ratio. The boundary conditions to be satisfied are:

$$\phi_z^\pm = S_x^\pm + S_t^\pm; \quad x_{le} \leq x \leq x_{te}, \quad z = 0^\pm, \quad (71)$$

on the wing and

$$\Delta\phi_z = 0 \quad \text{and} \quad \Delta(\phi_z + \phi_t) = 0; \quad x > x_{te}, \quad z = 0^\pm, \quad (72)$$

in the wake. The superscript  $\pm$  refers to the airfoil upper and lower surfaces,  $S(x, t)$  denotes the airfoil shape,  $x_{le}$  and  $x_{te}$  are the airfoil leading and trailing edge locations, respectively, and  $\Delta$  represents a jump in properties across the wake.

The interactive boundary layer modeling proposed by Edwards [93] uses Eq. (68) to compute the inviscid flow. The reader should be reminded that the TSD equation is suitable only for weak shocks and hence is restricted to shock boundary-layer interaction where the resulting flow separation is not considered massive. The description of the boundary layer solution is very much involved and requires a lengthy discussion of the boundary layer equations and the various approximations used in solving those equations. We shall not go into the details of Edwards' method [93], but refer the reader to the derivations given in his paper.

The boundary layer equations are solved in a quasi-steady manner using a set of ordinary differential equations in the  $x$ -direction for the momentum thickness  $\theta$ , shape factor  $H$ , and entrainment coefficient  $C_E$ . From these quantities, the displacement thickness  $\delta^*$  is calculated. The approach used by Edwards [93] utilizes the inverse boundary layer method. The inner and outer solutions are coupled through the boundary conditions on the wing and wake. From Eqs. (71) and (72), the boundary conditions on the airfoil are modified as follows:

$$\phi_z^\pm = S_x^\pm + S_t^\pm + \delta^*; \quad x_{le} \leq x \leq x_{te}, \quad z = 0^\pm, \quad (73)$$

and on the wake we have

$$\Delta\phi_z = \Delta(\delta_x^*); \quad x > x_{te}, \quad z = 0^\pm. \quad (74)$$

The coupling method is developed based on the observation that for transonic flow, the flowfield is unsteady, displaying oscillating shocks and separating and reattaching boundaries. The interacting boundary layer method is thus regarded as a simulation of two dynamic systems, the outer inviscid flow and the inner viscous flow, whose coupling requires special treatment to ensure that the coupling error between the two systems is minimized.

Edwards [93] used his method to compute the buffet onset boundary for a NACA 0012 airfoil and his results are shown in Fig. 42. His results show a much better correlation with experiments than those obtained by Barakos and Drikakis [87].

Calculations carried out on an 18% thick circular arc airfoil at  $Re_c = 10 \times 10^6$  and at  $M = 0.76$  give a value of the periodic shock frequency  $k = 0.47$  which agrees closely with McDevitt et al.'s [6] experimental value. The hysteresis effect due to increasing or decreasing Mach number on the onset and quenching of periodic motion can be computed from the interactive boundary layer method quite accurately. Fig. 43 shows the onset and quenching boundaries from Ref. [6] together with Edwards' [93] calculations. For increasing  $M$ , periodic motion occurs at  $M = 0.755$  compared to 0.76 experimentally, while for decreasing Mach numbers, periodic motion quenches at  $M \approx 0.73$  experimentally compared

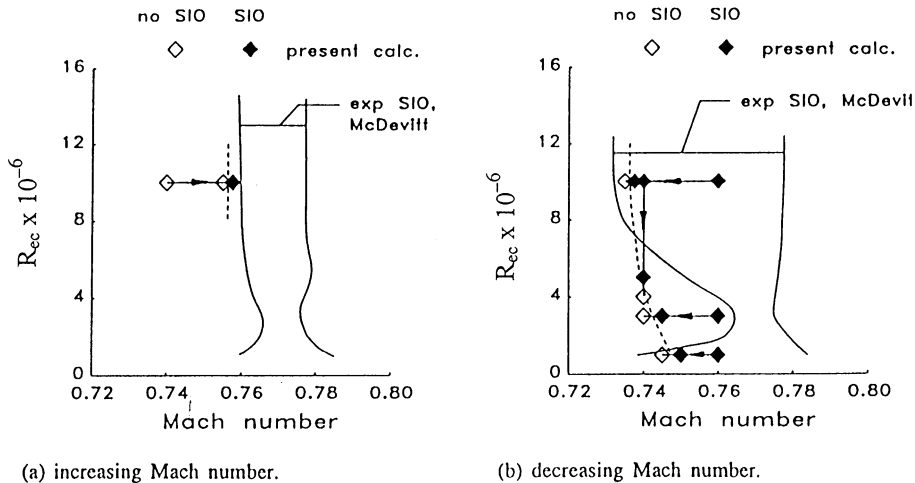


Fig. 43. Regions of SIO (shock-induced oscillations) for increasing and decreasing Mach number for the 18% thick circular-arc airfoil (from Ref. [93]).

to  $M = 0.735$  computationally. For lower  $Re_{cc}$ , a slight narrowing of the periodic shock oscillation region is predicted by Edwards [93], but the bend in the quenching boundary cannot be reproduced with sufficient accuracy. The increasing Mach number results are more accurate than those obtained by Rumsey et al. [69] using a Navier–Stokes code where they obtained a value of  $M = 0.75$  for the onset boundary, but the experimental quenching boundary at  $M = 0.73$  is more accurately predicted by the Navier–Stokes code.

Perhaps the most elegant viscous-inviscid interaction studies in unsteady transonic flow separation were carried out by Le Balleur and a few of his papers are given in Refs. [94–97]. Girodroux-Lavigne and Le Balleur [97] gives a first-order approximation to the defect formulation derived by Le Balleur [94,95]. The complex flowfield is computed by a viscous, a pseudo-inviscid, and an interaction solver. The interaction step is performed using a semi-implicit scheme and convergence is achieved at each time step. The defect between the real and pseudo-inviscid flow is obtained from the viscous solver which is approximated by integral equations and is solved by a marching scheme, either in direct or inverse modes. The pseudo-inviscid solver uses the small perturbation potential equation such as Eq. (68) and Coustin and Angelini [98] ADI scheme is adopted. The method has been used to compute the unsteady flow over an 18% thick circular-arc, a NACA 0012 airfoil, and the RA16SC1 supercritical airfoil [96,97]. The buffet boundary for the NACA 0012 airfoil at  $Re_{cc} = 10 \times 10^6$  is shown in Fig. 42 and the results are approximately  $0.5^\circ$  higher than the experimental values for the lower Mach numbers. The difference can be as large as  $1^\circ$  at  $M = 0.8$ . The boundary cannot be predicted as accurately as in

Edwards' method [93], but it is close to that obtained by Barakos and Drikakis [87]. The pressure time histories during buffeting of the NACA 0012 at  $M = 0.75$  and  $\alpha = 4^\circ$  is shown in Fig. 44. From Fig. 42, this condition occurs at about  $0.5^\circ$  inside the buffet regime and the airfoil may be experiencing moderate buffeting. The period of oscillation from computations is about 26% larger than experiments. The amplitude at  $x/c = 0.5$  is close to experiments while that at  $x/c = 0.8$  is smaller compared to the large peaks detected experimentally. The waveforms at  $x/c = 0.5$  and  $0.8$  are not well predicted and the peaks at  $x/c = 0.8$  from experiments are not reproduced. Compared to the Navier–Stokes results for an 18% thick circular-arc airfoil computed by Seegmiller et al. [24] (see Fig. 39), it can be said that the interactive boundary layer coupling method given by Girodroux-Lavigne and Le Balleur [97] does not reproduce oscillating pressure signatures as well as the Navier–Stokes codes.

An excellent prediction of the unsteady pressure fluctuations is obtained by Bartels and Rothmayer [99] using the method of matched asymptotic expansions in the leading order approximations of an unsteady compressible boundary layer interacting with an inviscid outer flow. The Levy–Lees form of the boundary layer equations is used and the inviscid flow is computed from the transonic small disturbance equation similar to Eq. (68). Results for an 18% thick circular-arc airfoil show that the computed shock oscillation frequencies are lower than those measured by McDevitt et al. [6] typically by 8–10%. The pressures in terms of  $\Delta C_p$  at  $x/c = 0.5$  and  $0.775$  match extremely well with experiments as shown in Fig. 45a at  $M = 0.773$  and  $Re_{cc} = 10 \times 10^6$ . The amplitude agrees with measured values but the difference in the period is difficult to determine accurately from the figure

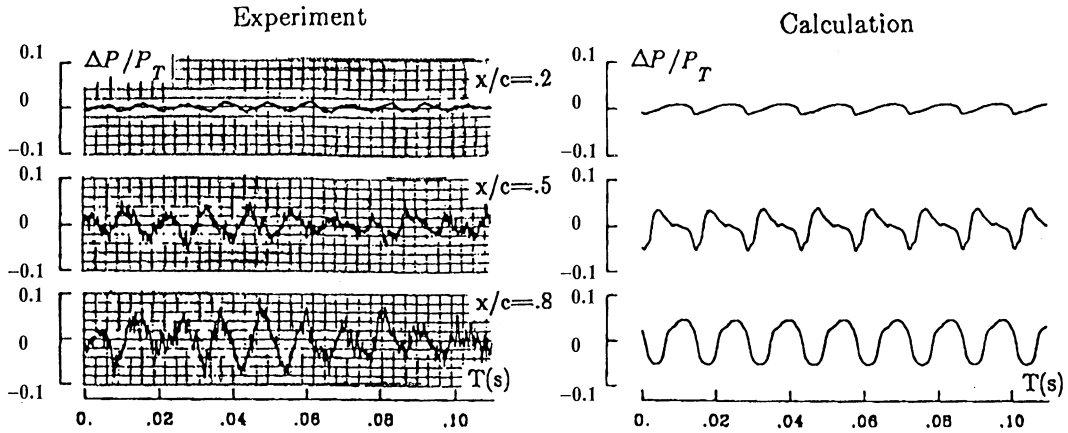


Fig. 44. Unsteady pressure time histories for NACA 0012 airfoil at  $M = 0.75$  and  $R_{ec} = 10 \times 10^6$  (from Ref. [97]).

although an 8% larger value is expected based on the difference in computed and measured shock oscillation frequencies. It is interesting to note that the code predicts high-frequency oscillations having a period 1/7 of the fundamental shock frequency (see Fig. 45b). Seegmiller et al. [24] also detected some high-frequency oscillations at  $M = 0.76$ ,  $R_{ec} = 11 \times 10^6$  from their Navier–Stokes computations although the frequencies appear to be lower than the experimental results.

It thus appears that the interactive boundary layer coupling method can produce results that are comparable with the more expensive Navier–Stokes codes. However, it will be interesting to use more advanced Navier–Stokes codes, such as the TLNS3D and CFL3D, to compute the buffet boundaries and pressure time histories of conventional and supercritical airfoils at moderate to heavy buffeting and compare the results with those obtained using the viscous–inviscid interaction schemes.

## 8. Control of shock oscillations

Experiments and numerical computations have shown conclusively that periodic shock motions on airfoils at transonic speeds are coupled to the flowfield in the wake region. To control the oscillations, we can either modify the flow in the shock–boundary layer interaction region or in the near wake by manipulating the trailing edge. In many cases, shock oscillations can be completely suppressed or delayed to a higher Mach number or incidence angle. The choice of control methodology must also take into consideration its effectiveness within the range of Mach number and incidence angle encountered. In some applications, the lift, drag and moment changes associated with the control strategy will need to be examined for overall performance evaluations.

### 8.1. Control of shock–boundary layer interaction

Transonic shock–boundary layer interaction and control have been the subject of investigation for many years in attempts to achieve drag reduction on airfoils. This topic is closely related to buffet alleviation since successful control of the boundary layer to reduce drag also decreases the amplitude of shock oscillations and in some instances suppresses the shock motions altogether. The subject of passive control of the interaction between a shock wave and a turbulent boundary layer is given in a review article by Raghunathan [100] where different schemes and their effectiveness on transonic airfoils are discussed.

The most commonly used procedure to control shock–boundary layer interaction is to modify the boundary layer in the interaction region by blowing or suction. One of the earliest proposals is to install a strip with a porous surface on the portion of the airfoil section where shock–boundary layer interaction occurs. A cavity or plenum is located underneath the porous surface. The static pressure rise across the shock wave will result in an outflow behind the shock into the plenum and the cavity permits injection of high pressure fluid into the region ahead of the shock wave. The thickening of the boundary layer produces a system of weaker shocks while the downstream suction reduces separation.

Thiede et al. [101] investigated three suction schemes using a supercritical airfoil (VFW VA-2) and the configurations are shown in Fig. 46. The basic airfoil model has interchangeable inserts, thus allowing tests to be conducted on a single slot, double slots and a perforated strip model. The slots and perforated strip were placed at a position coinciding with the shock location at an off-design Mach number  $M = 0.78$ . The Mach number range of the experiments was  $M = 0.6$  to  $0.86$ ,

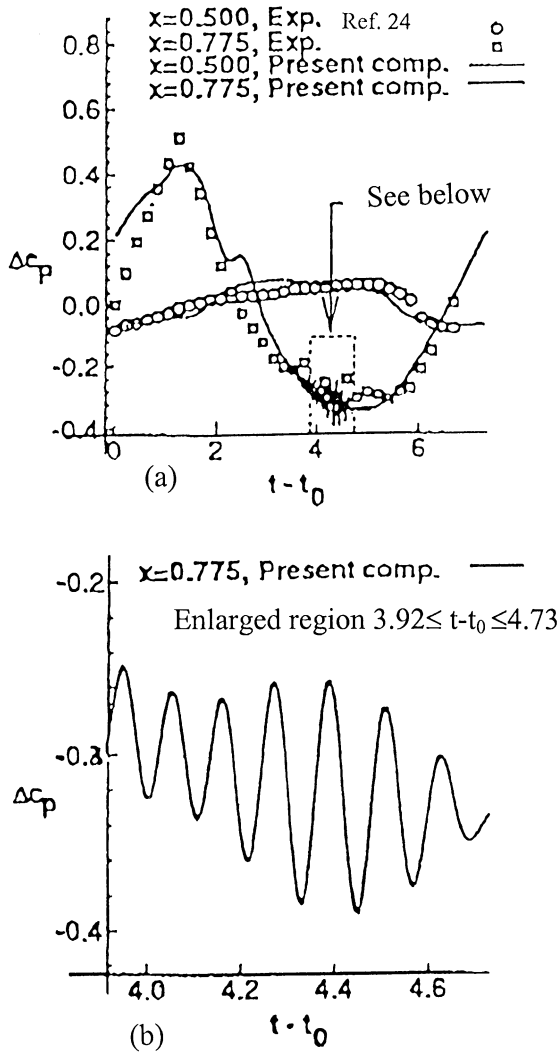


Fig. 45. Variation of  $\Delta C_p$  with time for one cycle,  $M = 0.773$  and  $Re_c = 10 \times 10^6$  (from Ref. [99]).

$Re_c = 2.5 \times 10^6$ , boundary layer trips were located at 30% chord on the upper surface and 25% on the lower surface, and suction coefficient was  $C_Q = 6 \times 10^{-4}$ . The effect of local boundary layer suction in the shock region is to delay the development of shock-induced separation and considerable improvements in the aerodynamic characteristics can be achieved. Thiede et al. [101] found that similar results can also be achieved for the double slots and perforated strip models without applying suction. This suggests that passive control using these two configurations without installation of mechanical suction devices is feasible even at the expense of a small decrease in performance. Fig. 47 shows the steady-state pressure distributions at  $M = 0.78$  for the clean surface and double slots configurations. At  $\alpha = 4^\circ$  which is close to

AIRFOIL VFW VA-2

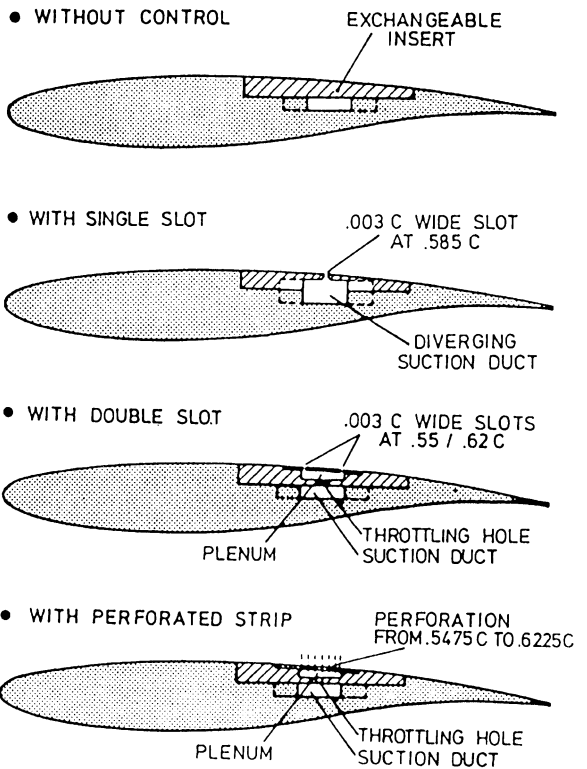


Fig. 46. Configurations for passive control of shock oscillations tested by Thiede et al. (from Ref. [101]).

the buffet onset boundary for the clean airfoil a thicker boundary layer is observed with the slots and the difference in pressure distributions between the two models is small. Inside the buffet boundary at  $\alpha = 5^\circ$ ,  $C_p$  distributions on the double slots configuration show the shock position to have moved only slightly forward. Without control, the shock moved quite far upstream and the pressure distributions have a shape typical of that for an unsteady flowfield after time averaging has been performed. The boundary layer near the shock region is thicker because of the blowing into the region ahead of the shock from fluid behind the shock that communicates to the front of the shock via the cavity. The pressure distributions with the perforated strip are quite similar to those with the double slots. For  $M \geq 0.78$ , the perforated strip gives better aerodynamic characteristics as well as a higher buffet boundary. But for  $M < 0.78$ , the double slots configuration improves the buffet characteristics of the airfoil quite significantly while the perforated strip seems to offer only a small improvement.

Passive methods to alleviate shock oscillations were also proposed by Raghunathan et al. [102] and the three

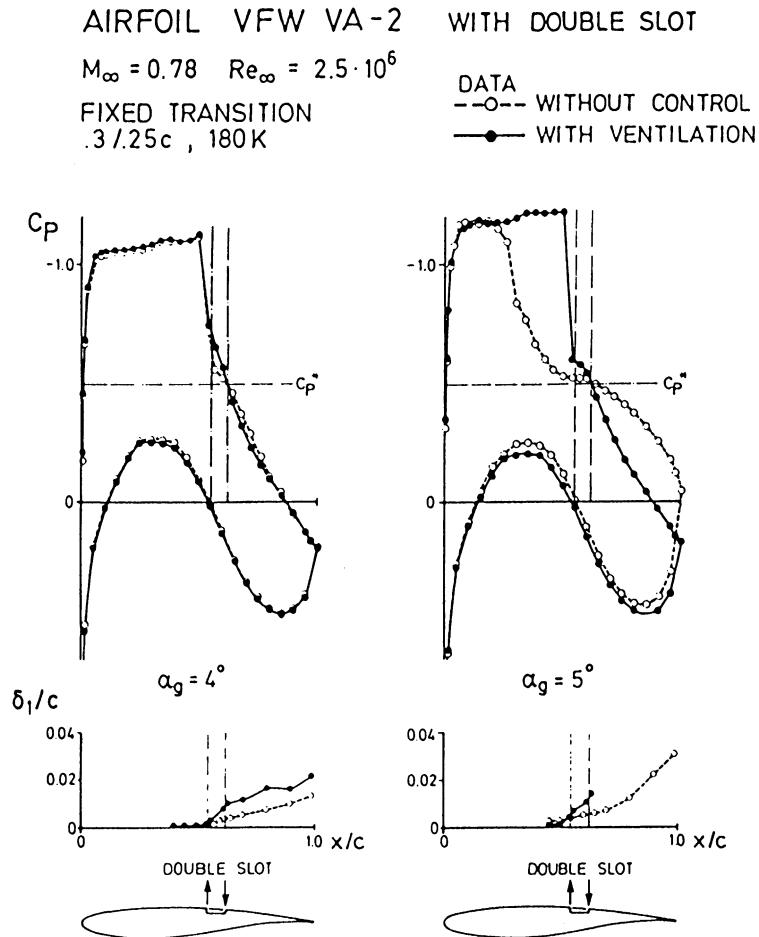


Fig. 47. Pressure distributions and boundary layer data with/without passive control (from Ref. [101]).

configurations tested on an 18% thick biconvex airfoil are shown in Fig. 48. The Reynolds number was fixed at  $Re_{cc} = 0.7 \times 10^6$  and the models had a transition trip near the leading edge on both surfaces. The buffer breather with interconnecting passage and the porous surface model are similar to the double slots and porous strip models tested by Thiede et al. [101]. The porous surface was located between 0.575 to 0.75 chord. Unsteady pressure measurements were conducted by a transducer located on the tunnel side wall at a distance 0.65 chord downstream of the leading edge and 0.175 chord normal to the airfoil plane of symmetry at zero incidence. The unsteady pressures measured in terms of rms fluctuations ( $\bar{p}$ ) normalised by the dynamic pressure  $q$  are shown in Fig. 49 for the 1.4% uniform and distributed porosity control strips. Vast improvements in attenuating the shock oscillations can be seen with an uniform porosity surface, but with even more impressive results are obtained with a distributed porosity model.

Configuration (b) in Fig. 48 has not been investigated in detail, but variations of configuration (a) having several rows of holes have been tested. With a porosity of 1.4% and greater, Raghunathan et al. [102] found that the shock oscillation has been greatly attenuated. This has been confirmed from spectra of the pressure fluctuations which show very small peaks at the shock oscillation frequency. The buffet breather concept was also studied by Gibb [54] on NACA 0012 and 14% biconvex airfoils. At incidence as high as  $\alpha = 3$  and  $5^\circ$ , the buffet breather is still effective in suppressing shock oscillations on the 14% biconvex airfoil.

Gibb [54] also proposed to install a wire just aft of the shock wave shown in Fig. 50c in order to fix the shock-induced separation position. The resulting flow is very stable without any periodic shock motion as determined from pressure measurements at  $x/c = 0.8$ . The wake is significantly larger and the drag is increased substantially, although this quantity was not measured.

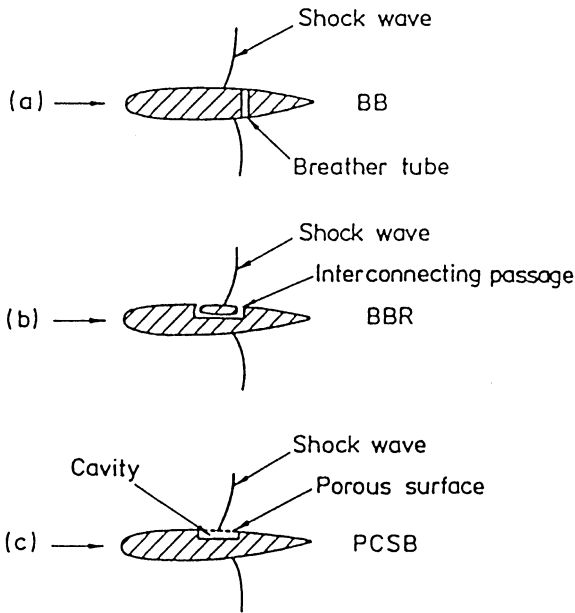


Fig. 48. Passive methods of alleviating shock oscillations (from Ref. [102]).

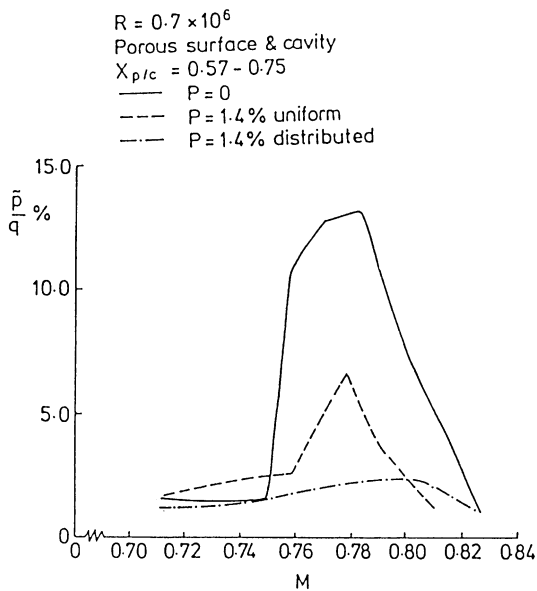


Fig. 49. Effect of passive control with distributed porosity on pressure fluctuation levels (from Ref. [102]).

8.2. Boundary layer control at the trailing edge

Alternatively, periodic shock motion can be controlled by manipulating the boundary layer at the trailing edge.

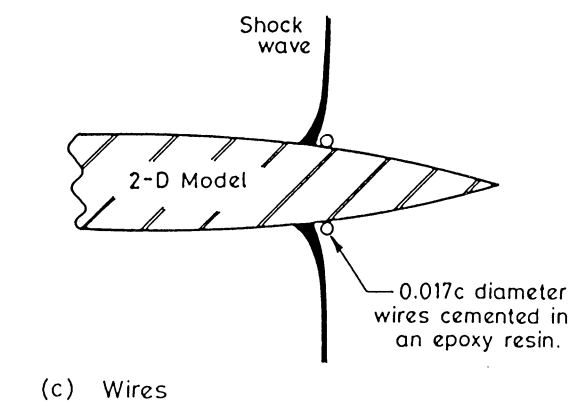
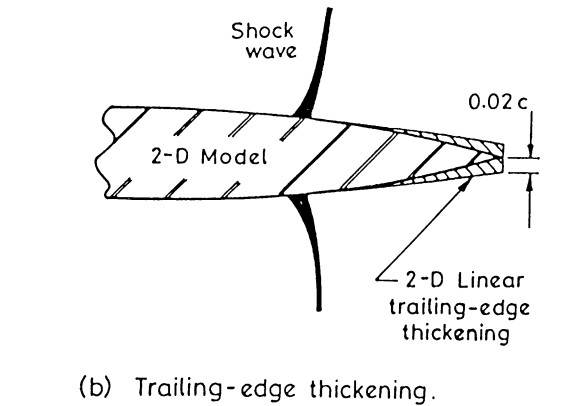
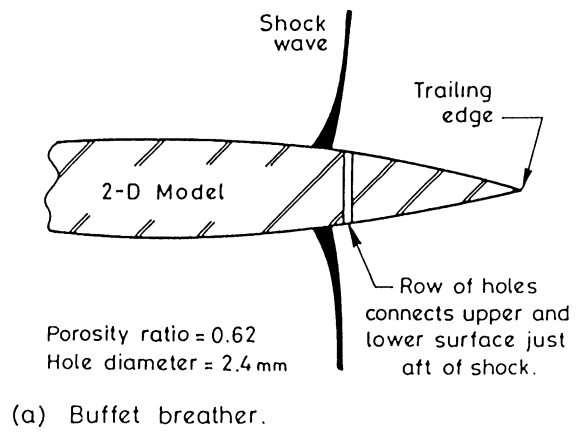


Fig. 50. Passive control of periodic flow (from Ref. [54]).

A simple technique is given by Gibb [54] where the trailing edge is thickened by modifying the airfoil profile (Fig. 50b). The technique was successfully tested at zero incidence on a 14% biconvex airfoil, and separation was effectively fixed at the start of the thickening of the modified airfoil trailing edge. The unsteady pressure fluctuations measured are slightly larger than those using

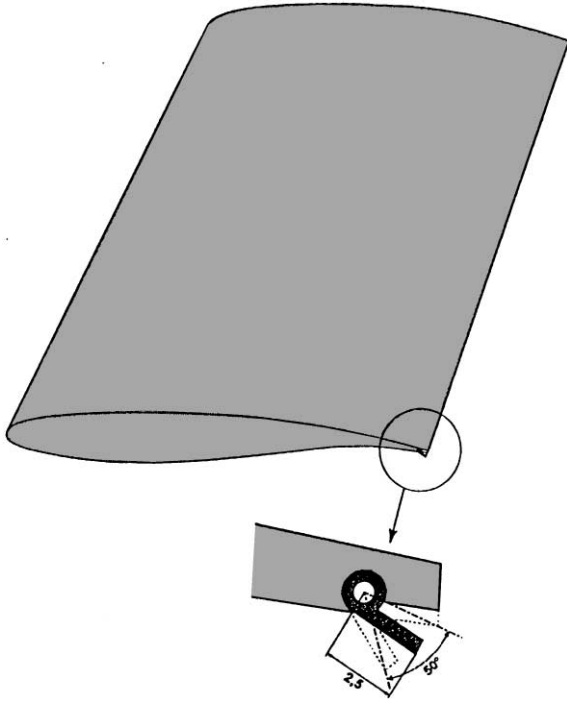


Fig. 51. Trailing edge deflector (from Ref. [103]).

a buffet breather located at  $x/c = 0.75$ . Again, no aerodynamic characteristics were measured, but an increase in drag is to be expected.

A trailing edge deflector [103] was designed at ONERA and installed on the OAT15A airfoil. Fig. 51 shows a schematic of the deflector which is located on the lower surface near the trailing edge. Its chordwise dimension is about 1–3% chord and can be moved to different static positions with an angular range between 0 and 60°. The 0° position coincides with the original thickness of the airfoil at the trailing edge. The device can also be driven both statically and dynamically by an electric motor. In the open loop mode, it was found that buffet onset can be delayed by choosing a suitable deflection angle. For example, at zero deflection angle buffet occurs at a lift coefficient  $C_L = 0.97$ . By setting the deflector at an angle  $\delta = 15^\circ$ , buffet occurs at  $C_L = 1.04$ . Open loop tests showed that when the deflector is driven at frequencies close to the buffet frequency, the influence on the shock frequency, amplitude and phase is significant. A closed-loop active control law to alleviate buffet was designed using pressure signal from the airfoil surface to activate the deflector. Writing the deflection angle  $\delta(t)$  as follows:

$$\delta(t) = \delta_m + A \times P(t - \tau), \quad (75)$$

where  $\delta_m$  is the mean angle,  $A$  is the gain and  $\tau$  is the time delay, Caruana et al. [103] obtained a significant

decrease in shock amplitude at  $M = 0.736$  by experimenting on the values of  $\delta_m$ ,  $A$  and  $\tau$ . The experimental observations were confirmed from numerical simulations using a viscous–inviscid interaction code.

The use of a trailing edge deflector is very similar in principle to buffet control by a trailing edge flap. Experiments on a 16% thick supercritical airfoil were reported by Lee [19] and Lee and Tang [29]. Flap angles can have a large influence on the shock positions and significant improvements in the buffet boundaries may be obtained. However, trailing edge flaps generally change the aerodynamic characteristics significantly and this factor needs to be taken into consideration when using flaps to alleviate buffeting.

## 9. Conclusions

Oscillatory shock waves are found on airfoils at transonic flow conditions and are associated with the phenomenon of buffeting. The motion is self-sustained and the mechanisms of periodic flow on the airfoil surfaces are discussed in this review. The importance of this subject was first recognized over fifty years ago, but a complete understanding of the mechanisms responsible for self-sustained oscillations of the shock waves under wide ranges of conditions, such as Mach number, incidence angle, Reynolds number, and airfoil geometry has not yet been achieved.

There are a number of models proposed to fit experimental observations to physical behavior of the flow in attempts to explain the onset and the self-sustaining nature of the periodic motion. Measurements of pressures on the airfoil surfaces and velocities in the wake indicate that the fluid motions in these two regions are strongly coupled. High-speed photography shows significant transverse oscillations of the wake near the trailing edge. Experimental investigations carried out on symmetrical airfoils at zero incidence show that there are narrow ranges of Mach numbers where shock oscillations can occur on the upper and lower surfaces of the airfoil. The two shocks move in anti-phase and the condition for periodic motion is such that the Mach number  $M_1$  in front of the shock wave lies in a range  $M_L \leq M_1 \leq M_U$ . The limits  $M_L$  and  $M_U$  vary for different airfoil geometry. The three types of shock motion proposed by Tijdeman have been observed on circular-arc airfoils of various thickness to chord ratios. A model which accounts for communications between the upper and lower airfoil surfaces has been suggested, and the shock motion is driven by the alternating regions of attached and separated flows on the airfoil surfaces.

For an airfoil at incidence where a shock wave is present only on the upper surface, the mechanisms of self-sustained oscillation are explained using a feedback loop which consists of downstream propagation of

disturbances in the separated flow and upstream propagation of waves in the inviscid fluid outside the separated flow region. The Mach number in front of the shock can be larger than  $M_U$  for a symmetrical airfoil at zero incidence. The oscillatory shock motion usually occurs for fully separated flows. It is interesting to note that the frequencies of oscillation for this case are nearly half of those for the symmetrical airfoils at zero incidence. Limited studies on supercritical airfoils at incidence show that only type A motion has so far been reported.

The disturbances generated by the shock propagate downstream into the wake. Inviscid compressible stability analysis shows that the frequency of the shock-induced disturbance generated on the airfoil surface is usually much lower than those for the most amplified waves in the shear layer. This suggests that at sufficiently far downstream distance from the trailing edge, the wake will be dominated by waves with frequencies other than that from the periodic shock motion.

Numerical simulation codes are powerful tools that can predict the shock oscillation frequencies as well as pressure fluctuations on the airfoil surfaces. The less time consuming interactive boundary layer coupling technique computes frequencies very close to the Navier–Stokes codes, but these two methods predict slightly different periodic motion domains for a symmetry airfoil at zero incidence. Turbulence modelling is important in the Navier–Stokes codes since different models give slightly different results for the buffet boundaries. Experimental measurements of turbulence properties can be used to improve turbulence modelling used in Navier–Stokes solvers.

Finally, much research is required to successfully control periodic shock motions. The devices used and the associated control laws to alleviate shock oscillations for a wide range of Mach number or incidence can be challenging. A successful mean to decrease the amplitude of shock oscillations or to delay the periodic motion to a higher Mach number or incidence angle will result in the achievement of an improved or expanded buffet boundary for the airfoil.

### Acknowledgements

The Institute for Aerospace Research provided time off from administrative duties to complete this task under project code 46\_DIO\_02. The support from the Natural Sciences and Engineering Research Council of Canada in the form of a research grant at the University of Ottawa is acknowledged.

### References

- [1] Hilton WF, Fowler RG. Photographs of shock wave movement. NPL R&M No. 2692, National Physical Laboratories, December 1947.
- [2] Pearcey HH, Osborne J, Haines AB. The interaction between local effects at the shock and rear separation — a source of significant scale effects in wind-tunnel tests on aerofoils and wings. AGARD CP-35, Transonic aerodynamics, Paris, France, 18–20 September 1968. p. 11.1–23.
- [3] Mundell ARG, Mabey DG. Pressure fluctuations caused by transonic shock/boundary-layer interaction. *Aeronaut J* Aug/Sept 1986;274–81.
- [4] Tjiedeman H. Investigation of the transonic flow around oscillating airfoils. NLR TR 77090 U, National Aerospace Laboratory, The Netherlands, 1977.
- [5] Humphreys MD. Pressure pulsations on rigid airfoils at transonic speeds. NACA RM L51112, National Advisory Committee for Aeronautics, December 1951.
- [6] McDevitt JB, Levy Jr LL, Deiwert GS. Transonic flow past a thick circular-arc airfoil. *AIAA J* 1976;14(5): 606–13.
- [7] Mabey DG, Welsh BL, Cripps BE. Periodic flows on a rigid 14% thick biconvex wing at transonic speeds. TR 81059, Royal Aircraft Establishment, May 1981.
- [8] Roos FW. Surface pressure and wake flow fluctuations in a supercritical airfoil flowfield. *AIAA 75-66*, *AIAA 13th Aerospace Sciences Meeting*, Pasadena, California, January 1975.
- [9] Hirose N, Miwa H. Computational and experimental research on buffet phenomena of transonic airfoils. NAL Report TR-996 T, National Aerospace Laboratory, Japan, September 1988.
- [10] Lee BHK. Investigation of flow separation on a supercritical airfoil. *J Aircraft* 1989;26(11):1032–7.
- [11] Lee BHK. An experimental investigation of transonic flow separation. In: Zhuang FG, editor. *Recent Advances In Experimental fluid mechanics*, Proceedings of First International Conference on Experimental Fluid Mechanics, Chengdu, China, June 17–21, 1991. Int. Academic Publishers, Beijing, China. p. 199–204.
- [12] Stanewsky E, Basler D. Experimental investigation of buffet onset and penetration on a supercritical airfoil at transonic speeds. AGARD CP-483, Aircraft dynamic loads due to flow separation, Sorrento, Italy, 1–6 April. 1990. p. 4.1–11.
- [13] Pearcey HH. Some effects of shock-induced separation of turbulent boundary layers in transonic flow past aerofoils. ARC R&M-3108, Aeronautical Research Council, June 1955.
- [14] Preston JH. The approximate calculation of the lift of symmetrical aerofoils taking into account of the boundary layer, with application to control problems. ARC R&M 1996, Aeronautical Research Council, 1943.
- [15] Spence DA. Prediction of the characteristics of two-dimensional aerofoils. *J Aeronaut Sci* 1954;21(9):577–87.
- [16] Pearcey HH. A method for the prediction of the onset of buffeting and other separation effects from wind tunnel tests on rigid models. AGARD Report 223, October 1958.
- [17] Pearcey HH, Holder DW. Simple methods for the prediction of wing buffeting resulting from bubble type separation. NPL AERO-REP-1024, National Physical Laboratory, June 1962.

- [18] Blackerby WT, Cahill JF. High Reynolds number tests of a C-141A aircraft semispan model to investigate shock-induced separation. NASA CR-2604, National Aeronautics and Space Administration, October 1975.
- [19] Lee BHK. Effect of trailing-edge flap on buffet characteristics of a supercritical airfoil. *J Aircraft* 1992;29(1):93–100.
- [20] McDevitt JB, Okuno AF. Static and dynamic pressure measurements on a NACA 0012 airfoil in the Ames High Reynolds Number Facility. NASA TP-2485. National Aeronautics and Space Administration, 1985.
- [21] Johnson DA. Transonic flow about a two-dimensional airfoil-inviscid and turbulent flow properties. AIAA 78-1117, AIAA 11th Fluid Dynamics and Plasma Conference, Seattle, Wash, July 1978.
- [22] Johnson DA, Bachalo WD, Owen FK. Transonic flow past a symmetric airfoil at high angle of attack. AIAA 79-1500, AIAA 12th Fluid and Plasma Dynamics Conference, Williamsburg, Virginia, July 1979.
- [23] Alber IE, Bacon JW, Masson BS, Collins DJ. An experimental investigation of turbulent transonic viscous-inviscid interactions. *AIAA J* 1973;11(5):620–7.
- [24] Seegmiller HL, Marvin JG, Levy Jr LL. Steady and unsteady transonic flow. *AIAA J* 1978;16(12):1262–70.
- [25] Roos FW, Riddle DW. Measurements of surface-pressure and wake-flow fluctuations in the flow field of a Whitcomb supercritical airfoil. NASA TN D-8443, National Aeronautics and Space Administration, August 1977.
- [26] Bütefisch KA, Stanewsky E. Experimental flow field study on a supercritical airfoil. *J Aircraft* 1987; 24(11):783–8.
- [27] Lee BHK. Transonic buffet on a supercritical airfoil. *Aeronaut J*, May 1990:143–52.
- [28] Eggleston B, Poole RJD. Thick supercritical airfoils with low drag and natural laminar flow. *J Aircraft* 1987; 24(6):405–11.
- [29] Lee BHK, Tang FC. Transonic buffet of a supercritical airfoil with trailing-edge flap. *J Aircraft* 1989;26(5):459–64.
- [30] Lee BHK, Tang FC. An experimental study of transonic buffet of a supercritical airfoil with trailing-edge flap. NAE-AN-54, National Research Council of Canada, September 1988.
- [31] Riddle DW. Wind-tunnel investigation of surface-pressure fluctuations associated with aircraft buffet. AIAA 75-67, AIAA 13th Aerospace Sciences Meeting, Pasadena, California, January 1975.
- [32] Roos FW. Some features of the unsteady pressure field in transonic airfoil buffeting. *J Aircraft* 1980;17(11):781–8.
- [33] Finke K. Unsteady shock wave-boundary layer interaction on profiles in transonic flow. AGARD CP-183, Flow separation, Gottingen, Germany, 27–30 May, 1975. p. 28.1–11.
- [34] Technical Report of the Accidents Investigation Subcommittee on the accident to the aeroplane G.AAZK at Meopham, Kent on 21st July, 1930. R&M No. 1360, British A.R.C., January 1931.
- [35] Coe CF, Mellenthin JA. Buffet forces on two-dimensional airfoils as affected by thickness and thickness distribution. NACA RM A53K24, National Advisory Committee for Aeronautics, February 1954.
- [36] Polentz PP, Page WA, Levy Jr LL. The unsteady normal-force characteristics of selected NACA profiles at high subsonic Mach numbers. NACA RM A55C02, National Advisory Committee for Aeronautics, May 1955.
- [37] Skopinski TH, Huston WB. A semi-empirical procedure for estimating wing buffet loads in the transonic region. NACA RM L56E01, National Advisory Committee for Aeronautics, September 1956.
- [38] Thomas F. Die ermittlung der schüttelgrenzen von tragflügeln im transsonischen geschwindigkeitsbereich. *Jahrb Wiss Gesellschaft Luft-Raumfahrt* 1966;126–44.
- [39] Mabey DG. Some remarks on buffeting. Tech. Memo. Structures 980, Royal Aircraft Establishment, February 1981.
- [40] DeAngelis VM, Monaghan RC. Buffet characteristics of the F-8 supercritical wing aircraft. NASA TM 56049, National Aeronautics and Space Administration, 1977.
- [41] Thomas F, Redeker G. A method for calculating the transonic buffet boundary including the influence of Reynolds number. AGARD CP-83, Facilities and techniques for aerodynamic testing at transonic speeds and high Reynolds, Gottingen, Germany, 26–28 April, 1971. p. 3.1–14.
- [42] Redeker G, Proksch HJ. The prediction of buffet onset and light buffet by means of computational methods. AGARD CP-204, Prediction of aerodynamic loading, NASA Ames Research Center, Moffat Field, CA, USA, 27–29 Sept. 1976. p. 22.1–10.
- [43] Bauer F, Garabedian P, Korn D. Supercritical wing sections. Lecture Notes in Economics and Mathematical Systems. Berlin: Springer, 1972.
- [44] Kacprzynski JJ. An experimental analysis and buffet investigation of the shockless lifting airfoil No. 1. LR-569, National Research Council of Canada, August 1973.
- [45] Lee BHK, Ellis FA, Bureau J. Investigation of the buffet characteristics of two supercritical airfoils. *J Aircraft* 1989;26(8):731–6.
- [46] Lee BHK, Ohman L. Unsteady pressure and force measurements associated with transonic buffeting of a two-dimensional supercritical airfoil. NAE-AN-14, National Research Council of Canada, June 1983.
- [47] Lee BHK, Ohman L. Unsteady pressures and forces during transonic buffeting of a supercritical airfoil. *J Aircraft* 1984;21(6):439–41.
- [48] Lee BHK. Flow separation on a supercritical airfoil. *CASI J* 1990;36(2):81–9.
- [49] Lee BHK. A study of transonic flutter of a two-dimensional airfoil using the U-g and p-k methods. LR-615, National Research Council of Canada, November 1984.
- [50] McDevitt JB. Supercritical flow about a thick circular-arc airfoil. NASA-TM-78549, National Aeronautics and Space Administration, January 1979.
- [51] Finke K. Stossschwingungen in schallnahen strömungen. VDI Forschungsheft 580. Dusseldorf: Verein Deutscher Ingenieure-Verlag, 1977.
- [52] Mabey DG. Oscillatory flows from shock-induced separations on biconvex airfoils of varying thickness in ventilated wind tunnels. AGARD CP-296, Boundary layer effects on unsteady airloads, Aix-en-Provence, France, 14–19 Sept. 1980. p. 11.1–14.

- [53] Mohan SR. Periodic flows on rigid aerofoils at transonic speeds. AIAA 91-0598, 29th Aerospace Sciences Meeting, Reno, Nevada, January 1991.
- [54] Gibb J. The cause and cure of periodic flows at transonic speeds. Proceedings 16th Congress of the International Council of the Aeronautical Sciences, Jerusalem, Israel, August–September 1988. p. 1522–30.
- [55] Erickson AL, Stephenson JD. A suggested method of analyzing transonic flutter of control surfaces based on available experimental evidence. NACA RM A7F30, National Advisory Committee for Aeronautics, December 1947.
- [56] Lee BHK. Oscillatory shock motion caused by transonic shock boundary layer interaction. AIAA J 1990; 28(5):942–4.
- [57] Spee BM. Wave propagation in transonic flow past two-dimensional aerofoils. NLR-TN-T.123, National Aerospace Laboratory, The Netherlands, July 1966.
- [58] Lee BHK, Murty H, Jiang H. The role of Kutta waves on oscillatory shock motion on an airfoil experiencing heavy buffeting. AIAA-93-1589, 34th AIAA/ASME/ASCE/AHS/ASC Structures, Structural Dynamics and Materials Conference, La Jolla, CA, April 1993.
- [59] Lee BHK, Murty H, Jiang H. Role of Kutta waves on oscillatory shock motion on an airfoil. AIAA J 1994;32(4):789–96.
- [60] Whitham GB. Linear and nonlinear waves. New York: Wiley, 1974.
- [61] Garabedian PR. Partial differential equations. New York: Wiley, 1964.
- [62] Sorenson RM, Wyss JA, Kyle JC. Preliminary investigation of the pressure fluctuations in the wakes of two-dimensional wings at low angles of attack. NACA RM A51G10, National Advisory Committee for Aeronautics, October 1951.
- [63] Lord Rayleigh. Scientific papers 1. London: Cambridge University Press, 1880.
- [64] Betchov R, Criminale Jr WO. Stability of parallel flows. New York: Academic Press, 1967.
- [65] Lessen M, Fox JA, Zien HM. On the inviscid stability of the laminar mixing of two parallel streams of a compressible fluid. J Fluid Mech 1965;23(2):335–67.
- [66] Chan Y, Leong R. Spatial instability of compressible wakes with three-dimensional disturbances. LTR-581, National Research Council of Canada, November 1984.
- [67] Liu JTC. Nonlinear development of an instability wave in a turbulent wake. Phys Fluids 1971;14(11):2251–7.
- [68] Reynolds WC. Large-scale instabilities of turbulent wakes. J Fluid Mech 1972;54(3):481–8.
- [69] Rumsey CL, Sanetrik MD, Biedron RT, Melson ND, Parlette EB. Efficiency and accuracy of time-accurate turbulent Navier–Stokes computations. AIAA-95-1835-CP, 13th AIAA Applied Aerodynamics Conference, San Diego, CA, June 1995.
- [70] Baldwin B, Lomax H. Thin layer approximation and algebraic model for separated turbulent flow. AIAA-78-257, AIAA 16th Aerospace Sciences Meeting, Huntsville, Alabama, January 1978.
- [71] Spalart P, Allmaras S. A one-equation turbulence model for aerodynamic flows. AIAA-92-0439, 30th Aerospace Sciences Meeting and Exhibit, Reno, Nevada, January 1992.
- [72] Levy Jr. LL. Experimental and computational steady unsteady transonic flows about a thick airfoil. AIAA J 1978;16(6):564–72.
- [73] Deiwert GS. Computation of separated transonic turbulent flows. AIAA-75-829, AIAA 8th Fluid and Plasma Dynamics Conference, Hartford, Connecticut, June 1975.
- [74] Deiwert GS. Numerical simulation of high Reynolds number transonic flows. AIAA J 1975;13(10):1354–9.
- [75] Marvin JG, Levy Jr LL, Seegmiller HL. Turbulence modeling for unsteady transonic flows. AIAA J 1980;18(5):489–96.
- [76] Steger JL. Implicit finite-difference simulation of flow about arbitrary two-dimensional geometries. AIAA J 1978;16(7):679–86.
- [77] Cebeci T. Calculation of compressible turbulent boundary layers with heat and mass transfer. AIAA J 1971;9(6):1091–7.
- [78] Edwards JW, Thomas JL. Computational methods for unsteady transonic flows. AIAA-87-0107, AIAA 25th Aerospace Sciences Meeting, Reno, Nevada, January 1987.
- [79] Rumsey CL, Thomas JL, Warren GP, Liu, GC. Upwind Navier–Stokes solutions for separated periodic flows. AIAA-86-0247, AIAA 24th Aerospace Sciences Meeting, Reno, Nevada, January 1986.
- [80] Gerteisen EA. Computations of unsteady flows around airfoil sections by explicit and implicit methods solving the Euler and Navier–Stokes equations. AGARD CP-507, Transonic unsteady aerodynamics and aeroelasticity, San Diego, CA, USA, 7–11 October 1991. p. 13.1–13.
- [81] Vatsa VN, Wedan BW. Development of a multigrid code for 3-D Navier–Stokes equations and its application to a grid-refinement study. Comput Fluids 1990; 18(4):391–403.
- [82] Thomas JL, Krist ST, Anderson WK. Navier–Stokes computations of vortical flows over low-aspect-ratio wings. AIAA J 1990;28(2):201–12.
- [83] Roe P. Approximate Riemann solvers, parameter vectors, and difference schemes. J Comput Phys 1981;43:357–72.
- [84] Raghunathan S, Gillan MA, Cooper RK, Mitchell RD, Cole JS. Shock oscillations on biconvex aerofoils. Aerosp Sci Technol 1999;3(1):1–9.
- [85] Raghunathan S, Mitchell RD, Gillan MA. Transonic shock oscillations on NACA 0012 aerofoil. Shock Waves 1998;8(4):191–202.
- [86] Kawai N, Hirose N. Development of the code NSFOIL for analyzing high Reynolds number transonic flow around an airfoil. NAL-TR-816, National Aerospace Laboratory, Japan, 1984.
- [87] Barakos G, Drikakis D. Numerical simulation of transonic buffet flows using various turbulence closures. Int J Heat Fluid Flow 2000;21(5):620–6.
- [88] Barakos G, Drikakis D. An implicit unfactored method for unsteady turbulent compressible flows with moving solid boundaries. Comput Fluids 1999;28(8):899–921.
- [89] Launder BE, Sharma BI. Application of the energy dissipation model of turbulence to the calculation of flow near a spinning disk. Lett Heat Mass Transfer 1974;1:131–8.
- [90] Nagano Y, Kim C. A two equation model for heat transport in wall turbulent shear flows. J Heat Transfer 1988;110:583–9.

- [91] Sofialidis D, Prinos P. Development of a non-linear strain sensitive  $k-\omega$  turbulence model. Proceedings of 11th Symposium on Turbulent Shear Flows, 1997. p. 289–94.
- [92] Batina JT. Unsteady transonic algorithm improvements for realistic aircraft configurations. *J Aircraft* 1989; 26(2):131–9.
- [93] Edwards JW. Transonic shock oscillations with a new boundary layer coupling method. AIAA 93-0777, 31st Aerospace Sciences Meeting and Exhibit, Reno, Nevada, January 1993.
- [94] Le Balleur JC. Computation of flows including viscous interactions with coupling methods. General Introduction Lecture 1, AGARD CP-291, Computation of viscous-inviscid interactions, United States Air Force Academy. Colorado Springs Colorado, USA, 29 Sept.–1 Oct., 1980.
- [95] Le Balleur JC, Girodroux-Lavigne P. A viscous-inviscid interaction method for computing unsteady transonic separation. In: Cebeci T, editor. Proceedings of third Symposium on Numerical and Physical Aspects of Aerodynamic Flows, California State University, 1985. Berlin: Springer, 1986. p. 252–71.
- [96] Girodroux-Lavigne P, Le Balleur JC. Unsteady viscous-inviscid interaction method and computation on buffeting over airfoils. Proceedings of Joint IMA/SMIAI Conference “Computational Methods in Aeronautical Fluid Dynamics”, University of Reading. Berlin: Springer, 1987.
- [97] Girodroux-Lavigne P, Le Balleur JC. Time-consistent computation of transonic buffet over airfoils. Proceedings of 16th Congress of the International Council of the Aeronautical Sciences, ICAS –88-5.52, 1988. p. 779–87.
- [98] Couston M, Angelini J. Numerical solutions of nonsteady two-dimensional transonic flows. *J Fluids Eng* 1979;101:341–7.
- [99] Bartels RE, Rothmayer AP. An IBL approach to multi-scaled shock induced oscillation. AIAA-95-2157, 26th AIAA Fluid Dynamics Conference, San Diego, CA, June 1995.
- [100] Raghunathan S. Passive control of shock-boundary layer interaction. *Prog Aerosp Sci* 1988;25:271–96.
- [101] Thiede P, Krogmann P, Stanewsky E. Active and passive shock/boundary layer interaction control on supercritical airfoils. AGARD CP-365. Improvement of aerospace performance through boundary layer control and high lift systems, Brussels, Belgium, 21–23 May 1984. p. 24.1–13.
- [102] Raghunathan S, Hall DE, Mabey DG. Alleviation of shock oscillations in transonic flow by passive controls. *Aeronaut J* 1990;94(937):245–50.
- [103] Caruana D, Corrège M, Reberga O, Desprè C, Mignosi A. Buffet and buffeting active control. AIAA-2000-2069, Fluids 2000, Denver, CO, June 2000.